THE TRANSACTIONS OF

The Royal Institution of Naval Architects

Vol 160 Part B1 2018

International Journal of Small Craft Technology

The Transactions of The Royal Institution of Naval Architects – Part B

International Journal of Small Craft Technology

ISSN 1740-0694 (Print)
ISSN 1740-2719 (CD-ROM)
ISSN 1740-0708 (Online)

The **International Journal of Small Craft Technology (IJSCT)** provides a forum for the reporting and discussion on technical and scientific issues associated with research and development of recreational and commercial small craft. The IJSCT is published as Part B of the Transactions of The Royal Institution of Naval Architects. Contributions in the form of scientific and technical papers and notes on the following aspects of small craft technology are invited:

- Design (including design methodologies, design practice, innovative concepts, design analysis tools, series data from experiments, design for safety, computer aided design).
- Construction (including one-off construction and series production issues, facility design, materials, joining technologies, reconstructions and rebuilds of historic craft).
- Operation (including racing, short handed sailing, equipment, results of seatrials, results of instrumentation, gear failure, human or vessel casualties, low technology operations).
- Regulation (including international, national, and regional regulatory frameworks, classification, codes of practice, rating rules).

PAPERS

Papers may introduce new theory or evaluate existing theory, or describe experimental or novel practical work, Papers presenting case histories will report on new or existing techniques, including design and production. Papers may also provide literary reviews which appraise and evaluate published work. All papers are refereed.

TECHNICAL NOTES

Technical notes will provide early announcement of new ideas, findings, procedures, applications, interim results, etc., which might later on form part of a full paper. Technical notes are refereed as for papers, but due allowance will be made for their immediate nature.

DISCUSSION

Comments on papers and technical notes will normally be published in the first available issue of the IJME following that in which the paper was published.Discussion may be continued in subsequent issues, at the discretion of the Editor. Authors will be invited to respond to published comment.

The Transactions of The Royal Institution of Naval Architects

Vol 160 Part B1 2018 **ISSN 1740 – 0694**

International Journal of Small Craft Technology

CONTENTS

PAPERS

TECHNICAL NOTES

There are no Technical Notes published in this issue of the IJSCT

DISCUSSION

COMPARATIVE STUDY IN DESIGN OF ANCHOR HANDLING TUG AND SUPPLY VESSELS OPERATING IN NORWAY AND INDONESIA

(DOI No: 10.3940/rina.ijsct.2018.b2.205)

Y H Chia and **A K Dev**, Marine Technology, Newcastle University in Singapore

SUMMARY

The present design of an Anchor Handling Tug Supply Vessel is greatly influenced by the operational requirements and the environmental conditions of the area of operation. This article looks at how the functional specifications and requirements of an Anchor Handling Tug Supply Vessel (AHTSV) affect its design, as well as the principal design drivers such as the area of operations, construction and operating costs, oil price and charter hire. An economic analysis based on pre-offshore crisis conditions is performed, and it is then re-evaluated taking into account the current offshore crisis. The article then compares the designs of the AHTSV based on two different areas of operations, namely Norway and Indonesia. Several possible design solution concepts are then derived for these two areas of operations.

1. INTRODUCTION

The global offshore oil and gas industry started a few years after the Second World War when the first mobile rig drilled an offshore oil well in about 4.5 metres (15 feet) water depth in the Gulf of Mexico off the US state of Louisiana (Offshore, 2007). Since then, the industry has come a long way, with offshore rigs currently drilling in the ultra-deep waters in the Brazilian pre-salt with depths up to 3,000 metres (Vidal *et al.*, 2015).

Offshore rigs such as fixed platforms, jack-ups, FPSOs and floaters are supported by specialised and customised vessels known as offshore support vessels (OSVs). OSVs provide support to the rigs in the form of towing, anchor handling, supplying of cargoes and stores, external fire-fighting, oil recovery, carrying and transferring personnel in limited number and other activities. There are various types of OSVs in the market, e.g. the anchor handling tug supply vessels (AHTSVs), platform supply vessels (PSVs), diving support vessels (DSVs), accommodation barges etc. In this article, only the AHTSVs are considered.

An AHTSV is mainly built to tow a rig to an offshore location; once at the site, help to lay the rig's anchors; and when the rig has finished drilling, the AHTSV will contribute to retrieve the anchors and tow it to another location. It is now common to find also AHTSVs performing the role of fire-fighting, rescue and even transporting supplies to and from the rigs. It is a multi-functional vessel and is a workhorse of the global offshore oil and gas industry.

The principal aim of this article is to compare the designs of the AHTSV based on two different areas of operations, namely Norway and Indonesia. The functional requirements that are relevant to the design of an AHTSV will be covered in the next section.

2. FUNCTIONAL REQUIREMENTS

The functional requirements for a modern AHTSV include towing, anchor handling and supply functions. These functions would be dependent on the vessel's bollard pull, its propulsion plant (main engines), anchor handling and towing winch, deck area including deck cargo loading capacity and storage pattern and stability.

2.1 BOLLARD PULL IN TONNES

Bollard pull is a conventional measure of the pulling or towing power of a tugboat and is one of a tugboat's primary design requirements. It is closely related to the Brake Horse Power (BHP) of the vessel. For example, the Bollard Pull (Tonnes) of a Tug with Twin screws in nozzles = f x (BHP/ 100) where f = 1.4 to 1.6 (Birmingham, 2015). It is common to find a new AHTSV fitted with twin controllable pitch propellers (CPP) in propeller nozzles as these improve the thrust of the propellers while the CPP provides variable propulsion power conditions regarding speed, bollard pull, and manoeuvrability.

2.2 TOTAL BRAKE HORSEPOWER (BHP) OF MAIN ENGINES

AHTSVs built in the '80s were mostly around 4,000 BHP and supported jack-up rigs drilling in shallow waters below 100 metres (approx. 330 feet). However as drilling moves to deeper water, and semi-submersible (semi-sub) rigs replace jack-up rigs and drill ships in harsh environments; the BHP of the AHTSV required to support the semi-subs has also increased to 8,000 BHP and more. It is because the semi-sub uses more massive anchor chains and anchors for its mooring system and hence requires an AHTSV with higher BHP/bollard pull for anchor handling and towing compared to the cable mooring system of a jack-up.

2.3 ANCHOR HANDLING AND TOWING (AHT) WINCH EQUIPMENT

Under the IMO Guidelines, the towing winch brakes should have an appropriate static holding capacity to that of the documented minimum breaking load (MBL) of the largest towline to be used. The minimum documented breaking load (MBL) of the main towline is 2.0 times the Bollard Pull (B.P.) for B.P. greater than 90 tonnes (IMO, 1998).

According to Bjørhovde & Aasen (2012), the winch packages for AHTSVs are large and heavy constructions with a weight that varies from 150 to 900 tonnes depending on types (single drum, double drums and triple drums) and may represent as much as 15% of the lightship weight of the vessel. It could influence the Vertical Centre of Gravity (VCG) and thereby the stability of the vessel. Miscalculation of the weight of the AHT winch equipment seems to be a very widespread error (Bjørhovde & Aasen, 2012).

2.4 DECK AREA AND DECK CARGO

For smaller AHTSVs, the deck area and deck cargo loading capacity are comparatively smaller (300 – 450 m^2 and 500 - 700 tonnes) as the vertical moment of deck cargo and deck cargo loading capacity are also related to stability under certain loading conditions. For bigger AHTSVs, the deck areas are much larger (700 - 900m^2 and 1200 - 1500 tonnes) which are capable of having higher vertical moments tagged to stability.

2.5 STABILITY

The stability of a new AHTSV is based on the Intact Stability Code 2008 (2008 IS Code) adopted by the IMO on 4 December 2008 (IMO, 2008). One of the requirements of 2008 IS Code stipulates that a minimum freeboard at the stern of at least 0.005L should be maintained in all operating conditions. It would work out to 0.35m for a 70m AHTSV. Another requirement is that the initial transverse metacentric height (GM) should not be less than 0.15m in 2008 IS Code.

An example of stability problem with AHTSVs was the Bourbon Dolphin which capsized on 12 April 2007 with most of its crew perished. One of the findings was that the vessel’s GM was reduced by 0.29m. It was because the KG (the vertical distance from the keel to the centre of gravity) was initially calculated to be 7.17m but during the inclining experiment was found to be 7.43m. The reason for the higher KG in the lightship condition was reportedly due to reduced weight control of parts during her construction. The vessel was initially designed to be 2,810 tonnes but was found to have a lightship displacement of 3,202 tonnes (Steamship, 2008).

There are other functional requirements for an AHTSV such as fire-fighting, carrying out rescue and recovery of oil but these can be considered as secondary functional requirements compared to its primary functions, which are anchor-handling, towing, and supply capabilities. As already discussed, these core functions would depend on the vessel’s bollard pull, the BHP of its main engines, AHT winch, deck area, cargo loading capacity and stability. The principal drivers relevant in the design of an AHTSV for two contrasting economic environments would be examined in the next section.

3. PRINCIPAL DESIGN DRIVERS

3.1 AREA OF OPERATIONS

One of the principal design drivers of an AHTSV would be the geographical area of operations. It will include the water depth where the rig will be operating as it will decide the type of rig (a jack-up or a semi-submersible) that the vessel will be supporting, the sea conditions, and the water depth of the supply base, from where the vessel will be operating. For example, in the Brazilian waters, the water depth in the offshore fields may vary from 200 to 3,000m, while the North Sea reaches almost 700m, but with much harsher sea conditions during the winter season (Vidal *et al.*, 2015).

Two countries (Norway and Indonesia) will be used to compare how geographical areas of operations can affect the design of an AHTSV.

3.1 (a) Norway

The history of the offshore oil and gas industry and its related offshore shipping companies in Norway is relatively short. When the first oil installations appeared on the Norwegian Continental Shelf in the 1970s, converted fishing vessels were used to provide supply services. However, in more than four decades, the Norwegian offshore shipping companies have grown to become world leaders with the world’s most modern and second most significant fleet. This development has also helped in the growth of Norwegian marine equipment suppliers, shipbuilders and ship designers such as Ulstein (N.S.A., 2012).

The water depths of Norwegian offshore fields vary from below 100 metres (example Embla Field) in the North Sea to more than 1,000 metres (example Ormen Lange) in the Norwegian Sea (NPD, 2013). Hence, bigger and more powerful AHTSVs are typically employed to support the semi-submersible floater rigs working there.

3.1 (b) Indonesia

Oil and gas exploration and production (E & P) in offshore Indonesia is mostly carried out in Western Indonesia in provinces such as Central Sumatra and East Kalimantan (PWC, 2012). The water depths in the offshore fields of the Natuna Sea in Central Sumatra are shallow (100 metres and below), and the water depth of offshore fields such as Peciko in East Kalimantan is around 60 metres (Total, 2012). In recent years, exploration in the deeper water (up 1,000 metres) in the Kutei Basin and the Makassar Strait has also discovered oil and gas deposits (Offshore-Mag, 2013).

While E & P may be moving towards deeper water in offshore Indonesia but most of such activities are still taking place in shallow water (100 metres and below) and relatively calmer sea conditions using jack-up rigs. The water depth of the cargo pier at the port of Balikpapan in Kalimantan, Indonesia is also between 6.4 - 7.6m which means that a bigger and more powerful AHTSV will be restricted from berthing alongside because of its operating draft. Hence, the majority of the AHTSV that are employed there to support the jack-up rigs are in the 5,000 BHP category.

Non-Indonesian flagged vessels are also prohibited from carrying passengers and/or goods between island or ports in Indonesian waters (Clyde, 2015). The Indonesian government applied this cabotage principle to offshore support vessels in 2014, and it has helped the local Indonesian ship owners to grow their fleet. A check on the website of PT Wintermar, a local owner with a fleet of more than 70 OSVs and listed on the Indonesian Stock Exchange, showed that it started its fleet expansion in 2007 and had in recent years also gone into joint ventures with offshore shipping companies. They have six new AHTSVs listed on their website of which, four are 8,000 BHP, and the remaining two vessels are 5,000 BHP (Wintermar, 2015).

3.2 COSTS OF CONSTRUCTING AND OPERATING AN AHTSV

There are two costs that an owner must consider before constructing an AHTSV. The first is the construction cost and second is the operating cost. Both types of cost can affect and be affected by the design of the vessel.

3.2 (a) Construction / Capital Costs

These would depend on various factors such as:

i) Place of construction – country of the shipyard building the vessel.
ii) Size/BHP of the vessel – Principal dimensions, deadweight, BHP of Main Engines, deck space, steel mass required, etc.
iii) Design Configuration – Type of engine (medium speed or high speed), type of propulsion (twin fixed pitch or controllable pitch propellers in nozzles or azimuthing thrusters), equipment on board (double or triple drum AHT winch, etc.).
iv) Number of sister vessels contracted – bulk discount given by shipyard

In their article, Kaiser & Snyder (2013) compared some of the construction costs of AHTSVs contracted between 2006 and 2008 (See Table 1). The same vessel design (VS 491 CD) can cost from US$85 million to US$95 million. The difference of US$10 million would most likely be because of the place of construction (Norway versus Indonesia) and also the equipment fitted on board (Kaiser & Snyder, 2013).

Although the construction cost of a 5,000 BHP AHTSV is not available in the above table, a generic five-year-old 5,000 BHP AHTSV would have been valued at about US$14 million in September 2013 before the offshore crisis started. The value of a similar 5-year-old vessel was valued at around US$3.5 million in November 2017, an impairment of almost 75% of the asset value (Griggs, 2017b).

Table 1. Some of the construction costs of AHTSVs contracted between 2006 and 2008 Source: Kaiser and Snyder (2013)

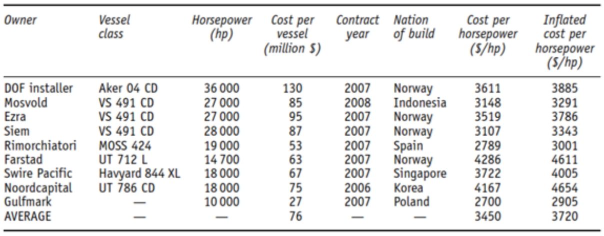

Owner	*Vessel class*	*Horsepower (hp)*	*Cost per vessel (million $)*	*Contract year*	*Nation of build*	*Cost per horsepower ($/hp)*	*Inflated cost per horsepower ($/hp)*
DOF installer	Aker 04 CD	36 000	130	2007	Norway	3611	3885
Mosvold	VS 491 CD	27 000	85	2008	Indonesia	3148	3291
Ezra	VS 491 CD	27 000	95	2007	Norway	3519	3786
Siem	VS 491 CD	28 000	87	2007	Norway	3107	3343
Rimorchiatori	MOSS 424	19 000	53	2007	Spain	2789	3001
Farstad	UT 712 L	14 700	63	2007	Norway	4286	4611
Swire Pacific	Havyard 844 XL	18 000	67	2007	Singapore	3722	4005
Noordcapital	UT 786 CD	18 000	75	2006	Korea	4167	4654
Gulfmark	—	10 000	27	2007	Poland	2700	2905
AVERAGE	—	—	76	—	—	3450	3720

3.2 (b) Operating Costs

These would depend mostly on the following:

i) Crewing Cost (Pre-Offshore Crisis)

The average daily crewing cost in Norway is around US$9,000 (Vikenes & Johannessen, 2014) while the average daily crewing cost in Indonesia is estimated to be US$1,600 (Deloitte, 2011) or even lower. As the crewing cost in Norway is high and could work out to be the same as the construction costs over the 25-year operating lifespan of the vessel, the owner would be looking at automation and technology to reduce manning to the minimum levels approved by the flag state. Such automation could include Unmanned Machinery Space (UMS) class notation.

ii) Fuel (Bunker) Consumption

Although bunkers are usually provided by the Charterers during the period charter of an AHTSV, however, the owner would still need to consider bunker consumption of the vessel carefully because during times of non-charter; in between charters; and mobilisation for a charter; the owners will be paying for the cost of bunkers. Furthermore, charterers are increasingly looking at the bunker consumption of the vessel besides the charter hire, when considering which vessel to charter. Hence, the owner has to consider during the design stage, the type of engine such as high speed or medium speed diesel as well as the number (two or four) to be fitted. Another alternative could also be the diesel-electric system, but the capital cost would be higher.

iii) Maintenance Costs

High-speed marine diesel engines, which are typically used as the primary drivers of an AHTSV are lower in cost for maintenance and spares. On the other hand, medium-speed marine diesel engines are more durable. Also, its specific fuel oil consumption (SFOC) can be up to 23% lower than high-speed marine diesel engines (Kristensen, 2012). Therefore, as mentioned above, the owner has also to consider these factors during the design stage, whether to go for lower maintenance costs but perhaps less durable and higher fuel consuming high-speed engines or higher maintenance costs but possibly more sustainable and lower fuel consuming medium speed engines.

3.3 OIL PRICE AND CHARTER HIRE

The price of crude oil has a substantial effect on the oil companies' E & P budgets. Oil companies will reduce their annual capital expenditure (Capex) and exploration budgets when the price of crude oil falls and is expected to remain at a relatively low cost. For example, Brent crude oil price fell from more than US$100 per barrel in August 2014 to below US$50 per barrel in January 2015. It dropped further to about US$30 per barrel in February 2016 before rebounding to close to US$70 per barrel in January 2018 (see Figure 1) (EIA, 2015).

Total presented a 2015 budget in February with a reduction of about US$3.2 billion in Capex and exploration (Total, 2015). It had affected deep water exploration and also production in existing fields and resulted in the reduction of a number of rigs and OSVs hired. OSVs on hire were also forced to take a charter hire reduction or had their charter terminated earlier. An oversupply of AHTSVs due to out of work vessels and reduced charter hire had also led to the cancellation of new constructions. Even though oil price has recovered from US$30 to US$70 per barrel and oil companies are likely to increase their exploration and production budgets, but the offshore shipping companies' fleet utilisation rates will remain low because of the oversupply of AHTSVs. This situation is made worse by an estimated 200 newbuild OSVs ready to be delivered from Chinese shipyards as of November 2017 (Griggs, 2017a). These new builds have been abandoned by offshore shipping companies that ordered them earlier or were built on speculation by the Chinese shipyards.

In contrast, offshore shipping companies such as Norway based Farstad Shipping did very well at the end of their 2007 financial year when oil price was moving from around US$50 per barrel in January 2007 to US$100 per barrel in December 2007. They were achieving 94% average utilisation rate and revenues of NOK 735 million (approx. US$131 million) for their North Sea fleet and had 13 vessels in the order book at the end of 2006 to be built and delivered (Farstad, 2008). One such vessel was the Far Sapphire (see Figure 2) (Creative Commons, 2015).

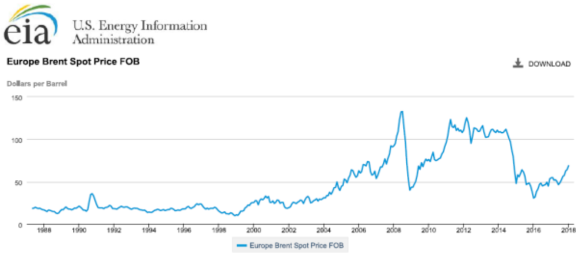

Figure 1: Brent Crude Oil Prices Source: EIA (2015)

Figure 2: Far Sapphire UT 732 CD AHTSV Source: Creative Commons (2015)

3.4 ECONOMIC ANALYSIS

The decision on whether to proceed to build a vessel will depend not only on the construction cost but also on the expected returns on the investment. The owner can use a simple capital budgeting tool such as payback period or a more sophisticated one such as Net Present Value, which takes into account the discounted cash inflows due to the cost of capital (the interest rate the bank charges for loan).

For a simple illustration, the payback period method and Farstad's UT 712 (14,700 BHP AHTSV) new construction in 2007 which cost US$63 million (see table above) will be used. The average utilisation and charter rates of the vessel, as well as the total operating expenses, are not known, but the following assumptions are made:

a) Crewing costs = US$9,000 per day which is around 65% of the total operating cost according to Vikenes and Johannessen (Vikenes & Johannessen, 2014)
b) Other (technical, insurance, etc.) operating costs = US$4,800 per day which is around 35% of the total operating cost
c) Overheads such as office staff salaries and other administrative expenses as well as dry-docking costs (once every 2.5 years) are not taken into account

d) Expected Payback Period = Assuming 20 years (Pre-offshore crisis) as the owner would probably want to achieve quicker breakeven although the usual economic lifespan of the vessel is 25 years

Given that Payback Period
= Cost of Vessel / Annual Net Cash Inflows, then

Annual Net Cash Inflows
= Cost of Vessel / Payback Period
= US$63 million / 20 years
= US$3.15 million

The total average operating cost per day is US$13,800 (US$9,000 + US$4,800), hence the annual total operating cost = US$5 million (approximately).

It means that annual charter hire must at least be US$3.15 million (net cash inflow) + US$5 million (total operating cost) = US$8.15 million (this is based on 100% utilisation rate) to break-even. It would work out to a daily charter rate of approximately US$22,000. Such a rate is very much attainable, especially in the North Sea during 2007 and it could even be considered low as North Sea rivals such as Viking Supply was getting an average daily charter rate of US$58,000 only just a few years ago (Viking, 2013). However, with the fall of oil price in 2014, charter rates in the North Sea for AHTSVs have dropped by almost 60% in January 2015 compared to a year ago (Seabrokers, 2015). Such rates had hardly recovered even after 3 years since the onset of the offshore crisis.

As can be seen from the above illustration, the economic analysis plays an important role when an owner is deciding on whether to proceed with new construction and at what cost that will allow the vessel to break-even in the shortest period. As mentioned earlier, construction cost will significantly affect the design of the vessel. When times are good, owners of AHTSVs are willing to spend on the top of the range design and equipment to stand out against competitors, but when times are bad like now, most owners of AHTSVs are fighting for survival and unlikely thinking of building new vessels.

3.5 DESIGN ENVIRONMENT AND PROCEDURES

Based on what has been discussed till now, Figure 3 shows the inter-relationship between the environmental factors (external and internal) and the design of an AHTSV.

As seen from Figure 3, many factors can affect the design of an AHTSV similar to the multi-criterion design optimisation decision-making of a bulk carrier proposed by Parsons and Scott (Parsons & Scott, 2004). There are also multiple conflicting criteria in the design of an AHTSV such as the minimisation of lightship weight versus maximisation of bollard pull, for example, and the ship designer has to come up with the best-optimised design based on such criteria.

Vidal *et al.* (2015) have developed a parametric model for operability of offshore support vessels via configuration-based design, and this could be useful for the designer. However, one of their derived designs from this model is a PSV operating in Brazil with a bollard pull of 105 tonnes, which is most unusual as PSVs do not have a towing winch (Vidal *et al.*, 2015).

In the opinion of the authors, the primary design driver would be vessel cost. The vessel cost would be related to the intended BHP and bollard pull of the AHTSV. The bollard pull of the AHTSV would be linked to the area of operations (e.g. Norway or Indonesia). Hence the bollard pull would be the most critical design requirement and would carry more weight if a multi-criterion design optimisation based on the model of Parsons and Scott were to be used. Several possible solution concepts that would be appropriate for each of these two economic environments/areas of operations (Norway and Indonesia) are derived in Section 4.

4. POSSIBLE SOLUTION CONCEPTS

All three of the designs (original, adaptive, and variant) can be found in the marine and offshore industry throughout history.

4.1 ORIGINAL DESIGN

The original design concept would be more appropriate for a developed economy such as Norway if the current offshore crisis is not considered. In the recent years, there have been quite some innovative ship designs coming out from countries in Western Europe, such as Norway and Netherlands. For example, the X-Bow ship design was developed by Norwegian company Ulstein, as an AHTSV (Bourbon Orca) for Bourbon Offshore Norway (See Figure 4) (Creative Commons, 2012). Ulstein has since adopted this design for PSV, Seismic, and Offshore Construction Vessel (OCV). Ulstein claimed that the backwards-sloping bow had been optimised to (or "intending to") high speeds, low resistance and reduced fuel consumption as well as the elimination of slamming and bow impact. Reasons, why the original design concept is appropriate for Norway, are because:

1) Increasing deeper waters and very rough weather for AHTSV operations in the North Sea and the Norwegian Sea will require more innovative designs for larger AHTSVs with better seakeeping capability and bigger bollard pull to handle semi-subs.

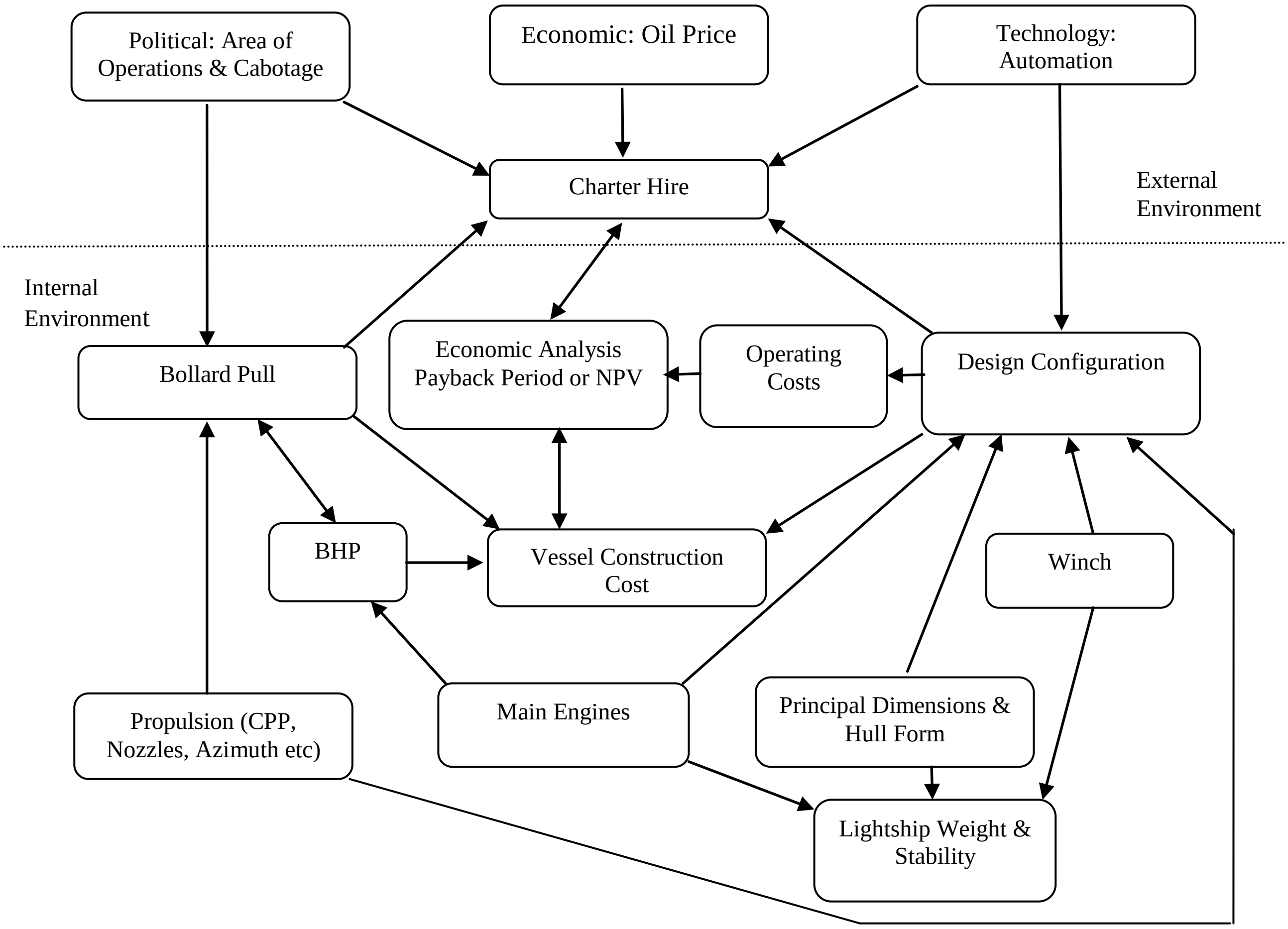

Figure 3: Inter-relationship between the environmental factors (external and internal) and the design of an AHTSV

Figure 4: Bourbon Orca AHTSV Source: Creative Commons (2012)

2) Lower pollutant emissions in Emission Control Areas such as the North Sea means the need to have more innovative and cleaner designs using the diesel-electric or hybrid system to meet the stringent requirements.

Future designs are likely to look at the hybrid diesel generator-fuel cell power plant for lower pollutant emissions (Diaz-de-Baldasano *et al.*, 2014).

4.2 ADAPTIVE OR VARIANT DESIGN

For a developing economy such as Indonesia which has a strict cabotage policy forbidding foreign offshore shipping companies to work there, the more appropriate design concept would be either an adaptive or variant design. Reasons, why the adaptive or variant design concept is suitable for Indonesia, are because:

1) AHTSV operations are still in relatively shallow waters, even though exploration has started to move to deeper waters. However, the weather patterns in Indonesia are still not as rough as the North Sea.
2) Original design AHTSV would cost more to build as there is a higher price to pay for innovation. Offshore shipping companies in Indonesia are still relatively small players, and even the bigger ones that are listed on the country's stock exchange are nowhere in the league of Norwegian offshore shipping companies.

3) Indonesian offshore shipping companies are likely to go for the "commodity design" AHTSV 5150 BHP that have been built in significant numbers in Chinese shipyards as shown in Figure 5. The design of such vessels has been adapted from an older AHTSV design with minor changes and cost around US$12 million before the offshore crisis. But with a significant oversupply in the Chinese shipyards due to the speculative building, these shipyards have halved the price as they are being forced by banks to pay back for the financing of construction of such vessels (Griggs, 2017a).

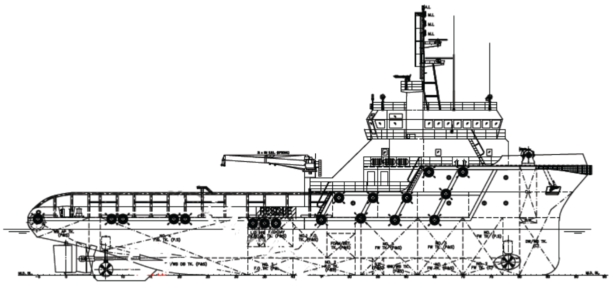

Figure 5: Typical 5150 BHP AHTS Vessel

5. CONCLUSIONS

This article has shown how the design of an AHTSV would differ in two distinct geographical and economic environments. For the developed economy, an original design is proposed to be more appropriate for the reasons given in section 4, while for the developing economy, the variant or adaptive design is the most suitable design concept proposed with reasons are also presented in Section 4.

Besides the economic environment, it has also looked at other external as well as internal environmental factors which would influence the design. As mentioned earlier, this article aims to compare the designs of the AHTSV based on two different areas of operations, namely Indonesia and Norway. It is the opinion of the authors that the aim has been met as can be seen from the industry examples and references given, as well as the diagram shown in Figure 3, which has been developed based on the authors' understanding of the complex design decision criteria.

6. ACKNOWLEDGMENTS

The authors express their profound acknowledgements to Creative Commons for the "free to share" photos of Bourbon Orca and Far Sapphire.

The authors also express sincere thanks to Professor Richard W. Birmingham for his excellent lecture notes on "Tugs – A Dynamic Design Environment – Divergent Design Solutions" in MSc in Marine Technology (International) module Advanced Marine Design.

7. REFERENCES

1. BIRMINGHAM, R.W. (2015) '*Unit 3 of Module MAR8227 – Advanced Marine Design: Tugs – A Dynamic Design Environment – Divergent Design Solutions*'. Newcastle University.
2. BJØRHOVDE, S. and AASEN, R. (2012) '*Parametric estimation of anchor handling / towing winches*'. 71st Annual Conference of Society of Allied Weight Engineers Bad Gögging and Manching – Bavaria, Germany.
3. CLYDE (2015) *Clyde & Co: Cabotage and its impact in Indonesia.* Available at: http://www.clydeco.com/insight/updates/view/cabotage-and-its-impact-in-indonesia.
4. CREATIVE COMMONS (2012) *Bourbon Orca in Bergen 01.jpg*. Available at: https://commons.wikimedia.org/wiki/File:Bourbon_Orca_in_Bergen_01.jpg
5. CREATIVE COMMONS (2015) *FAR SAPPHIRE (16917782647).jpg*. Available at: https://commons.wikimedia.org/wiki/File:FAR_SAPPHIRE_(16917782647).jpg
6. DELOITTE (2011) '*Challenge to the industry: Securing skilled crews in today's marketplace*'.
7. DIAZ-DE-BALDASANO, M.C. *et al.* (2014) '*Conceptual design of offshore platform supply vessel based on hybrid diesel generator- fuel cell power plant*'. Applied Energy, 116 91-100.
8. EIA (2015) *Europe Brent Spot Price.* Available at: http://www.eia.gov/dnav/pet/hist/LeafHandler.ashx?n=PET&s=RBRTE&f=M.
9. FARSTAD (2008) *Annual Report 2007.* Available at: https://www.farstad.com/prod_images/doc_274_10.pdf
10. GRIGGS, D. (2017a) '*Chinese yards halve prices on hundreds of unwanted OSVs*'. Tradewinds, November 23rd, 2017.
11. GRIGGS, D. (2017b) '*Forced sales finally trigger S&P rush for offshore ships*'. Tradewinds, November 2nd, 2017.
12. IMO (1998) '*MSC/Circ.884 Guidelines for safe ocean towing*'.
13. IMO (2008) '*Resolution MSC.267(85) Adoption of the international code on intact stability, 2008* (2008 IS code)'.
14. KAISER, M.J. and SNYDER, B.F. (2013) '*Economic impacts of the offshore supply vessel shipbuilding market in the Gulf of Mexico*'. Maritime Economics & Logistics, 15 (2), pp. 256-287.
15. KRISTENSEN, H.O. (2012) *Energy demand and exhaust gas emissions of marine engines* Available at: https://www.shipowners.dk/services/beregningsvaerktoejer/download/Basic_Model_Linkarea_Link/164/wp-2-report-5-energy-demand-and-emissions-of-marine-engines.pdf.

16. N.S.A. (2012) *Norwegian Shipowners' Association – Norwegian Offshore Shipping Companies*. Available at: https://www.rederi.no/DownloadFile/?file=1102
17. NPD (2013) *Norwegian Petroleum Directorate – Facts 2013 The Norwegian Petroleum Sector*. Available at: npd.no/global/engelsk/3-publications/facts/facts2013/facts_2013.pdf.
18. OFFSHORE (2007) *History of the offshore industry*. Available at: http://www.offshore-mag.com/index/about-us/history-of-offshore.html (Accessed: 12 Sept 2015).
19. OFFSHORE-MAG (2013) *Offshore Indonesia E&P activity revs up.* Available at: http://www.offshore-mag.com/articles/2013/03/offshore-indonesia-e-p-activity-revs-up.html.
20. PARSONS, M.G. and SCOTT, R. (2004) '*Formulation of multicriterion design optimization problems for solution with scalar numerical optimization methods*'. Journal Of Ship Research, 48 (1), pp. 61-76.
21. PWC (2012) *Oil and Gas Indonesia – Investment & Taxation Guide.* Available at: http://www.pwc.com/id/en/publications/assets/oil-and-gas-guide_2012.pdf.
22. SEABROKERS (2015) *Seabreeze: The Seabrokers Monthly Market Report.* Available at: http://www.seabrokers.no/wp-content/uploads/Seabreeze-January1.pdf.
23. STEAMSHIP (2008) '*Bourbon Dolphin – A Case History*'.
24. TOTAL (2012) *Indonesia: Total starts South Mahakam production ahead of schedule.* Available at: http://www.total.com/en/media/news/press-releases/indonesia-total-starts-south-mahakam-production-ahead-schedule.
25. TOTAL (2015) *2014 Results and Outlook.* Available at: http://www.total.com/sites/default/files/atoms/files/4t14-presentation-2014-and-outlook.pdf.
26. VIDAL, H.L., GASPAR, H.M., WEIHMANN, L. and MINIOLI, L.E.B. (2015) '*A parametric model for operability of offshore support vessels via configuration-based design*'. Marine Systems & Ocean Technology, 10(01) 47-59.
27. VIKENES, T. and JOHANNESSEN, C.K. (2014) *Comparing OSV operations in Brazil with Norway.* Available at: http://brage.bibsys.no/xmlui/bitstream/handle/11250/277961/Masterthesis.pdf?sequence=1.
28. VIKING (2013) *Viking Supply Ships Financial Report Q4 2013.* Available at: http://www.vikingsupply.com/userfiles/Financial%20reports%20VSS%20AS/Viking%20Supply%20Ships%20AS%202013%20Q4.pdf.
29. WINTERMAR (2015) *Wintermar Offshore Marine Group*. Available at: http://www.wintermar.com/index.html.

NUMERICAL TOOLS AND EXPERIMENTAL PROCEDURES FOR THE PREDICTION OF NOISE PROPAGATION ON BOARD SUPERYACHTS

(DOI No. 10.3940/rina.ijsct.2018.b1.207)

G Vergassola, **T Pais**, and **D Boote**, University of Genova - Italy

SUMMARY

The Italian Classification Society, RINA S.p.A., is developing a new set of Rules regarding comfort conditions on board large motor-yachts. Relative to present owner requirements and technical enhancement, the new limit values will be more restrictive especially for yachts of more than 65 metres in length. In this respect designers and shipyards should consider structure borne noise and vibration level as leading parameters from the earliest design stages. In this paper some numerical tools, which allow prediction of noise propagation on board before sea trials to be carried out, are presented.

NOMENCLATURE

ABN	Air-borne noise
DLF	Damping loss factor
f_c	Coincidence frequency [Hz]
FEA	Finite Element Analysis
FEM	Finite Element Method
NVH	Noise, Vibration, Harshness
L_{OA}	Length Overall [m]
SBN	Structure-borne noise
SEA	Statistical Energy Analysis
SPL	Sound Pressure Level [dB]
η_i	Damping loss factor in SEA matrix
η_{ij}	Coupling loss factor in SEA matrix
ω	Radiance frequency (rad)

1. INTRODUCTION

In recent years, the main parameter that designers have to consider during a megayacht project has shifted from speed to human comfort on board, in order to fulfil owners’ requirements.

Thus the assessment of level of noise and vibration has become a necessary task that has to be carried out even during the early design stages, when modifications in the structural layout and/or in the insulation plans can be accomplished with low working times and costs.

Moreover, Classification Societies are developing stricter rules in terms of NVH, by fixing new limit values for vibration velocities and sound pressure level (SPL) especially for super and megayacht ($L_{OA} > 65$ m) (Registro Italiano Navale, 2017).

As far as vibration assessment is concerned, numerical procedures based on FEA are well-established in the literature (Boote, et al, 2013) (Pais, et al, 2016). The numerical evaluation of air-borne noise (ABN) and structure-borne noise (SBN) has only emerged in the last few years by the development of software based on the Statistical Energy Analysis (SEA). By means of this procedure, the SPL distribution can be calculated even for those high frequency ranges, where deterministic solutions cannot be considered reliable. Despite this, the Statistical Energy Analysis needs the use of experimental results, especially for the damping loss factor (Vergassola, et al, 2018) and input power evaluation, in order to improve the accuracy of the calculation.

In this paper, after an overview of the SEA for marine applications, an experimental procedure regarding the input power calibration has been presented in order to improve the accuracy of the noise propagation simulations.

2. RINA ADDITIONAL COMFORT NOTATIONS

A mandatory regulation “The Code on noise levels on board ships” (hereinafter referred to as "the Code") has been developed by IMO (IMO, 2012) to provide international standards for protection against noise and to promote "hearing saving" environments on conventional passenger and cargo ships in order to avoid a noise-induced hearing loss.

The Code is intended to provide the basis for a design standard to prevent the occurrence of potentially hazardous noise levels and to provide an acceptable environment for seafarers with compliance based on the satisfactory conclusion of sea trials that result in issuance of a Noise Survey Report which show the noise to a level which is not potentially harmful.

In addition to the work undertaken by the IMO, Classification Societies have developed the so called “COMFORT” class notations with stricter requirements and recommendations not only to protect the people on board from excessive noise levels but also to provide living spaces with an acceptable degree of comfort in navigation. In this scenario, verifications of the acoustic insulation between spaces and of the structure borne noise on floor decks have to be carried out.

The Additional voluntary notation COMFORT class is assigned only when measurements during sea trials demonstrate that noise and vibration limit levels have been met.

RINA's additional class notations for comfort on board can in turn be assigned depending on the type of vessels as follows:

- COMF-NOISE to assess the noise level on all types of ships (compliance with Code of Noise Levels on Board Ships, IMO Resolution MSC.337(91));
- COMF-VIB to assess the vibration level on all types of ships;
- COMF Yacht to assess the noise and vibration levels on private or charter yachts;
- COMF (LY) to assess the noise and vibration levels on large yachts (Lpp>60m);
- DOLPHIN to set limit for the underwater radiated noise for both commercial vessels, pleasure yachts and yachts (above 24 meters).

The first three notations have been developed with prescriptive limits obtained by numerous tests on existing vessels in collaboration with shipyards and shipowners to provide reference values in compliance with the international standards.

Taking into account results of research projects in which several underwater radiated noise measurements have been carried out, DOLPHIN could be adopted in areas which are highly sensitive to environmental issues such as areas of marine mammal reproduction.

The notation COMF (LY) is the last one developed with the intention of obtaining the best compromise between the limit levels of a passenger ship with reduced vessel length and the performance required in luxury yachts taking into account also the well-being of the crew.

In the following Table I and Table II the limit levels for noise comfort on large yachts are shown:

Table I: Noise limits levels – passenger spaces – navigation

Type of space	**Navigation**	
	L_A	**L_B**
Passenger spaces		
Passenger cabins – superior	50	55
Passenger cabins – standard	53	60
Public spaces – lounges	55	60
Open main deck recreation areas, aft	75	79
Open deck recreation areas above, aft **(1)**	65	70
Wheelhouse	60	75
(1) +10 dB(A) if less than 1 m from the ventilation inlet/outlet		

The notation is differentiated by a letter A or B which represents the merit level achieved for the assignment of the notation, the merit A corresponding to the lowest level of noise and vibration.

Table II: Noise limits levels – passenger spaces – At berth

Type of space	**At berth**	
	L_A	**L_B**
Passenger spaces		
Passenger cabins – superior	45	50
Passenger cabins – standard	48	53
Public spaces – lounges	50	55
Wheelhouse	50	65

During the design stage, verification of compliance could be addressed by means of SEA-based calculations with the aim of obtaining conservative results in addition to applying a margin related to the uncertainties of the methodology.

3. THE STATISTICAL ENERGY ANALYSIS FOR MARINE APPLICATION

3.1 THEORETICAL BACKGROUND

The SEA is a framework of study (Lyon, 1975) for the prediction of sound and vibration for complex dynamic systems. The statistical aspect of this method emphasizes the differences between deterministic numerical approaches (such as FEM, FDM, FVM, etc.) that are not able to predict the correct behaviour for high frequency ranges in which the mode shape and resonance frequencies are highly sensitive to small details of geometry and construction.

This aspect could be solved in traditional FEA by using the so called Monte Carlo Approach (Zhang, et al, 2013) with a great increase in computational time and costs.

The Statistical Energy Analysis from a purely theoretical point of view is a set of power balance equations, derived from the principle of conservation of energy.

Considering that a complex dynamic system can be divided into at least two simpler subsystems (Figure. 1) the set of power balance equations can be written as:

$$\begin{cases} \sum_1^2 \pi_{in,i} = \sum_1^2 \pi_{out,j} \\ \pi_{out,i} = \pi_{ij} + \pi_{diss,i} \end{cases} \tag{1}$$

Where $\pi_{in,i}$ is the power input in the i-th subsystem, $\pi_{out,i}$ is the power output, π_{ij} is the amount of power that is transmitted between i-th and j-th subsystem and $\pi_{diss,i}$ is the power that is dissipated by the i-th subsystem.

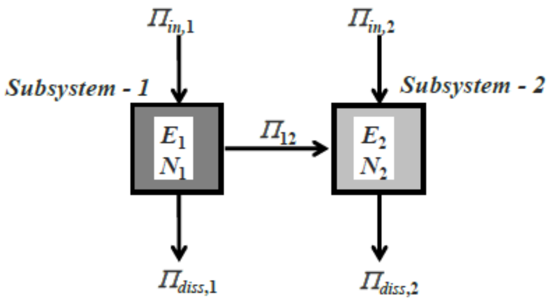

Figure 1: SEA system composed by 2 subsystems

In Figure. 1, the term E_i denotes the total energy of each subsystem and N_i is the modal density.

The dissipated power of each subsystem can be written as:

$$\pi_{diss,i}(\omega) = \omega \cdot \eta_i \cdot E_i \qquad (2)$$

where η_i describes the damping loss factor (DLF) of the subsystem.

The last unknown term is the transmitted power that is depending on the energy of each subsystem as it follows:

$$\pi_{ij}(\omega) = \omega \cdot \eta_{ij} \cdot n_i \cdot \left(\frac{E_i}{n_i} - \frac{E_j}{n_j}\right) \qquad (3)$$

By applying these sets of equations, a subsystem that could be decomposed in millions of nodal degrees of freedom in a deterministic numerical analysis, in SEA has only 1 energy degree of freedom, so the calculation is substantially less onerous.

The coupling loss factor η_{ij} depends on the type of subsystem (e.g. beam, shell, acoustic cavity) and on the transmission path (mass law, resonant, non-resonant or double wall) under consideration.

Under these assumptions, a SEA problem for a dynamic system composed of two subsystems could be written in matrix form as:

$$\begin{bmatrix} \pi_{in,1} \\ \pi_{in,2} \end{bmatrix} = \omega \cdot \begin{bmatrix} n_1(\eta_1 + \eta_{12}) & -n_1\eta_{12} \\ -n_2\eta_{21} & n_2(\eta_2 + \eta_{21}) \end{bmatrix} \begin{bmatrix} \frac{E_1}{n_1} \\ \frac{E_2}{n_2} \end{bmatrix} (4)$$

Generalizing Eq. 4 for an N-components dynamic system, the SEA matrix system is:

$$\begin{bmatrix} \pi_{in,1} \\ ::: \\ \pi_{in,N} \end{bmatrix} = \omega \cdot \begin{bmatrix} n_1(\eta_1 + \sum_{i\neq 1}\eta_{1i}) & -n_1\eta_{12} & \cdots & -n_1\eta_{1N} \\ -n_2\eta_{21} & n_2(\eta_2 + \sum_{i\neq 2}\eta_{2i}) & \cdots & \cdots \\ \cdots & \cdots & \cdots & \cdots \\ -n_N\eta_{Ni} & \cdots & \cdots & n_N(\eta_N + \sum_{i\neq N}\eta_{Ni}) \end{bmatrix} \cdot \begin{bmatrix} \frac{E_1}{n_1} \\ ::: \\ \frac{E_N}{n_N} \end{bmatrix} (5)$$

In the symmetric matrix system shown in Eq. 5, no information on mode shapes and on natural frequencies is requested for SEA computation; this implies that the analysis could be considered well-conditioned only for relative high value of n_i, typically higher than 2-3 modes per band.

For lower n_i values, an hybrid approach is required; the information on natural modes and shapes are acquired from a preliminary FEM or BEM analysis as a precursor to the SEA computation.

3.2 SUPERYACHT MODELLING

A predictive analysis of the noise propagation on board superyacht using SEA requires the creation of a global model of the vessel, as shown in Figure. 2.

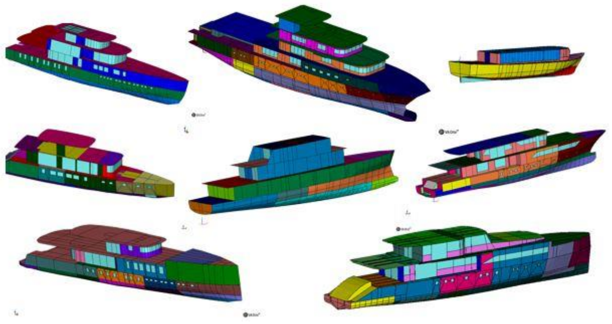

Figure 2: Examples of SEA global models for superyacht applications

The structural layout of the vessel (plates, longitudinal stiffeners and transversal frames) has to be created by using SEA plates or beams. This typology of elements, that could be actually more subdivided into different kinds of plates (plane, curved ribbed), uses different transmission paths for noise and vibration and implies also different coupling loss factors in the transmitted power Eq. 3.

While the creation of the structural layout could be considered as easier with respect to a complete FEM model (due to the absence of small elements and nodes to be linked) the SEA procedure requires also the creation of internal subsystem, say "acoustic cavity", that are necessary for having the SPL as output.

Moreover, as shown in Figure. 3, internal subdivisions, as well as external plating, have to be carefully modelled following the vessel's insulation plans, in order to apply the correct noise control treatment (NCT) in each area.

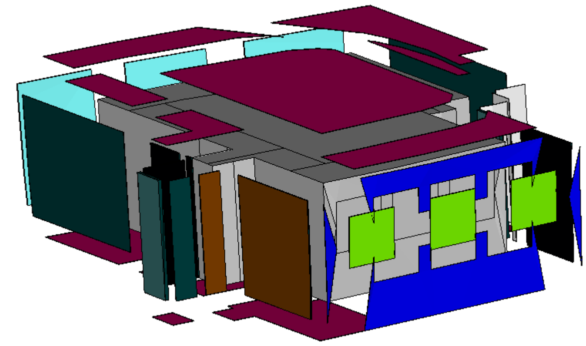

Figure 3: Internal panel subdivision of an owner's cabin

The three windows have been clearly highlighted in green, because, as discussed later, they cause the main power input contribution to the SPL of the cabin itself.

This means an increase in the pre-processing times and also implies a deep knowledge in the mechanical and dynamical (in terms of DLF and radiation efficiency) characterization of materials (Gragnani, et al, 2015) (Boote, et al, 2017).

3.3 TYPICAL RESULTS SCHEMES AND MAIN INPUT VARIABLES

As already stated, the main advantage of SEA for naval architecture is its ability to predict the SPL in each zone of the vessel and the main energy path for SBN.

The overall SPL has to be compared with limit values imposed by IMO (Registro Italiano Navale, 2017) for charter yacht, and with Classification Societies rules for private yachts or if owner requires additional class notations.

In Figure. 4, a typical SPL diagram for an entire vessel is reported.

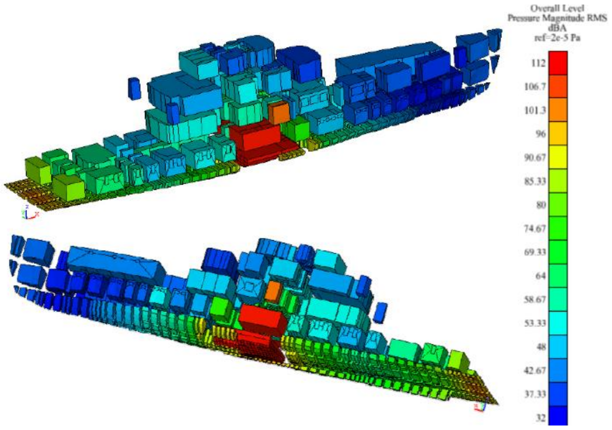

Figure 4: SPL distribution on a superyacht

Moreover, SEA analysis is able to plot (as shown in Figure. 5) the contribution to the total energy in each subsystem given by panels or adjacent cavities. In Figure. 5 the power input plot of the owner's cabin shown in Figure. 3 is reported.

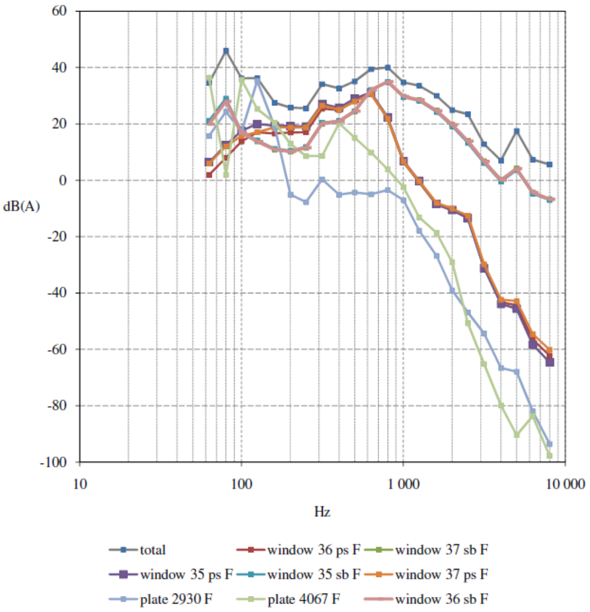

Figure 5: Power input diagram of the owner cabin shown in Figure. 3

This tool is very helpful because, in cases where rooms fail to comply with limits, it can clarify which panels radiate more noise and so where the transmission loss has to be improved.

In the aforementioned study, the main contribution to the pressure level in the owner's cabin is due to glazing windows in the mid frequency range; this behaviour is caused by the coincidence frequency (f_c) of the windows, which is at 800 Hz, causes the classical drop in transmission loss, as shown in Figure. 6.

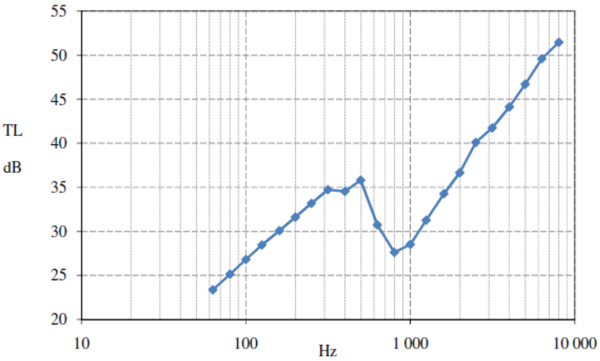

Figure 6: Transmission loss (TL) of owner's cabin windows

Looking in detail to Eq. 5, it appears clear that the main input variables in the SEA procedure are the damping loss factor of each subsystem (Vergassola, et al, 2018) and the calculation of the power input. In addition, it is not sufficient to have these data merely in terms of magnitude, but they must be quantified for the whole frequency range under consideration.

For these reasons, in the next sections of this work, numerical tools and experimental activities are presented in order to perform a reliable power input calibration (based on an hybrid approach) with easy and quick experimental activities.

4. POWER INPUT CALIBRATION BY HYBRID SEA-FEM APPROACH

The SEA procedure requires a precise definition of the input power spectrum; for marine application, the principal sources are the propulsion engines, that are directly connected to the hull's structure thorough the engine foundation, as shown in Figure. 7.

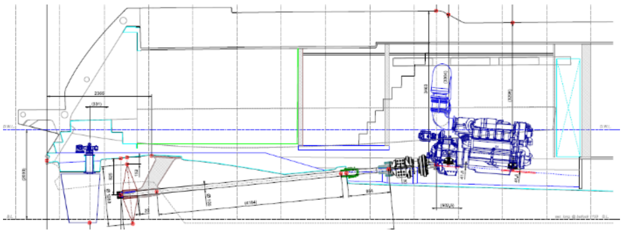

Figure 7: A typical propulsion engine installation with traditional shaft line

The foundation, and in particular viscoelastic materials used for this application, are able to significantly modify the amount of energy transmitted to the hull's bottom and consequently the SBN propagation.

Therefore, the aim of this study is to test a methodology to obtain the power source to input in the foundations, starting from standard vibration data for the main engine (usually given as a vibration velocity spectrum).

The procedure herein presented can be summarized by 4 main steps:

1. Creation of an hybrid model composed of an FE model of structural foundation and SEA elements of the surrounding structures
2. Calibration of input forces (narrow band) to obtain the measured velocity spectra;
3. Calculation of the power input (1/3 octave band) representing the main engine action to input to the full SEA global model;
4. Evaluation of the results in terms of sound pressure levels inside the vessel by means of SEA calculation with the computed power input.

For this purpose, two input data are required:

- Velocity spectrum measured on the main engine foundation below and above the resilient mounting (Figure. 8);
- FE model of the structural foundation and SEA model of the whole vessel from which the hybrid model described at point 1 can be created.

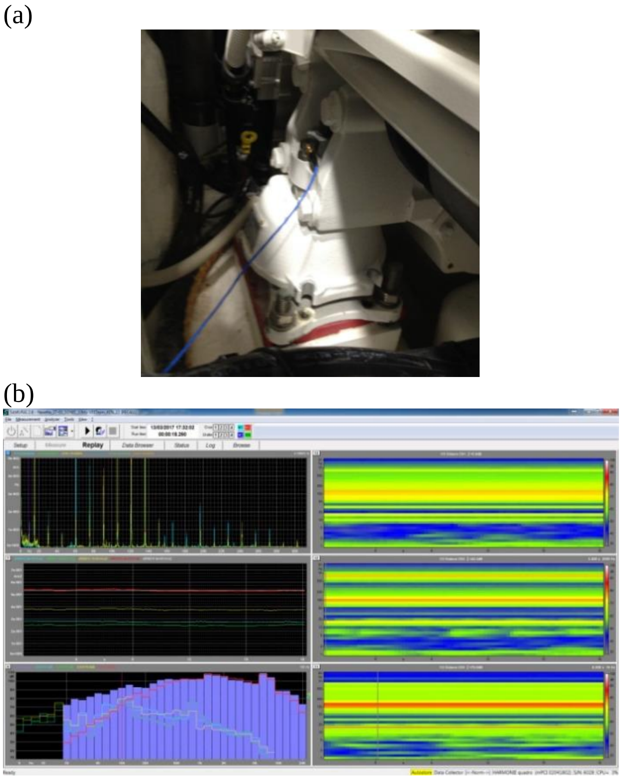

Figure 8: Velocity spectrum measurement, (a) accelerometers positioning and (b) response spectrum

The velocity spectrum has been measured by the instrumentation shown in Figure. 9; it consists in an impact hammer and piezoelectric accelerometers for the calculation of the frequency response function and a microphone for the calculation of the SPL.

Figure 9: Instrumentation for N&V measurements on board

The hybrid model of the engine foundation (Figure. 10) facilitates a reliable calculation even for the low frequency range, where a full SEA approach could lead to higher uncertainties. Moreover, the same testing condition could be created in the coupled SEA-FE model, by using forces and velocity sensor in the same place of the experimental activity.

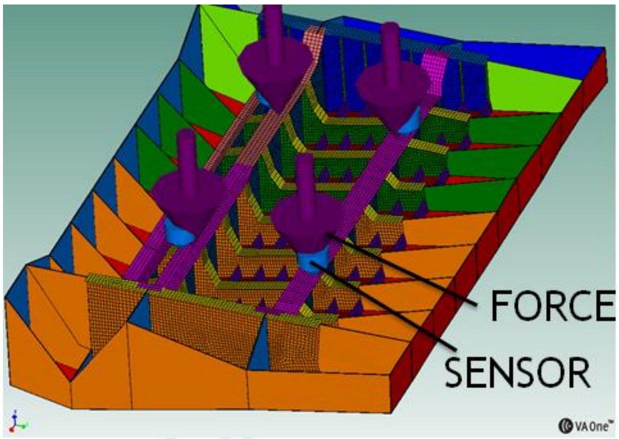

Figure 10: Hybrid model of the engine's foundation

A local analysis of the hybrid model shown in Figure. 10 is carried out by applying a unit input force (F_{1N}). The velocity spectrum obtained by the numerical procedure (V_{1N}) has to be compared with the one obtained through the experimental measurements ($V_{measured}$).

Since the FE analysis is a linear static one (MSC Software Corporation, 2016), the superposition principle can be applied; so the correct input force (F_{INPUT}) can be calculated as:

$$F_{INPUT}(\omega) = F_{1N}(\omega) \cdot \frac{V_{measured}(\omega)}{V_{1N}(\omega)} \qquad (6)$$

Once having found the total input force generated by the propulsion engines and the foundation's mobility (Biot, et al, 2014) (Y_z) (computed by the software), the power input spectrum can be easily calculated:

$$P_{INPUT}(\omega) = < F^2{}_{INPUT}(\omega) > \cdot\, Re(Y_z(\omega)) \qquad (7)$$

The power input spectrum calculated by Eq. 5 can be applied to a global SEA model as shown in Figure. 11.

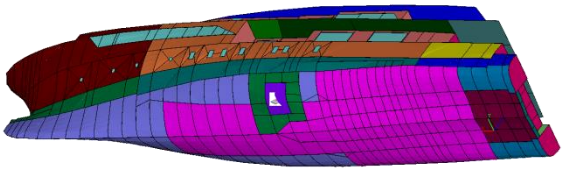

Figure 11: A global SEA model

A comparison between the measured velocity spectrum and the velocity spectrum obtained from different numerical models, applying Eq. 6, is shown in Figure. 12.

As it can be easily seen, the FE model alone (i.e. not integrated in a hybrid model with SEA plates) is not reliable for the mid and high frequency range, as stated by Pais et al. (2018) where the oscillations are caused by local resonances of the mesh grid that are not corresponding to the real phenomenon.

Using the abovementioned hybrid model the reliability of the results increases if compared to the measured velocity spectrum.

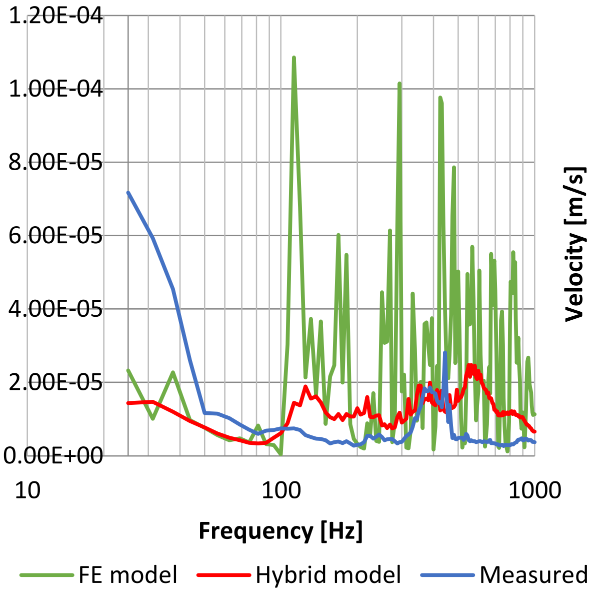

Figure 12: Velocity spectrum comparison

Figure 13 shows a comparison between the SPL in the engine control room (adjacent to the engine room) measured onboard and the results of the SEA with the power input calculated using the described procedure.

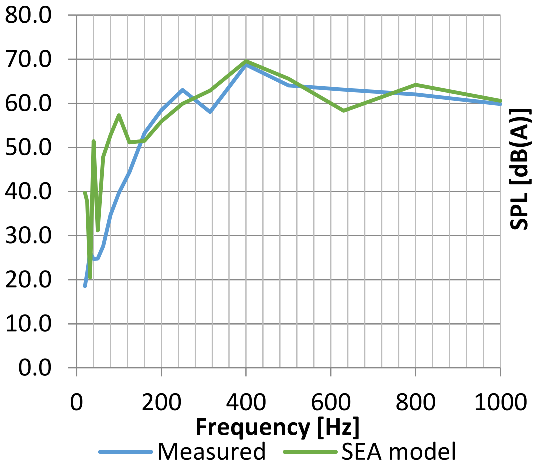

Figure 13: Comparison of the SPL in the engine control room

The general trend is similar; there is a discrepancy at low frequency but a good correspondence above 200 Hz.

5. CONCLUSIONS

The increased number of stricter rules and regulations in terms of vibration and noise level on board super and megayachts has shifted the focal point of naval architects to the prediction of noise and vibration levels, and consequently the insulation of vessels.

From this perspective, new numerical tools such as Statistical Energy Analysis have been developed in order to consider these tasks at the early stages of a project, where changes can be made with less time and cost and extend the reliable frequency range.

The level of uncertainties in a SEA calculation are higher than for a deterministic approach like FEA and they have to be carefully taken into consideration while performing global analyses on vessels. For these reasons, experiments have to be carried out to improve the confidence of analysis to an error level up to ±3 dB.

For this purpose, in this paper, a procedure for the calibration of the input power due to propulsion engines has been studied in depth using a hybrid SEA+FEA model.

This research is being extended to establish the parameters affecting the underwater radiated noise from superyachts and the calibration of the noise radiated by the propeller on the stern structures.

6. ACKNOWLEDGEMENTS

The authors wish to thank Mr. Angelo Tonelli and Mr. Daniele Torre for their precious and continuous support to this research which is still ongoing.

7. REFERENCES

1. REGISTRO ITALIANO NAVALE, *Rules for the Classification of Yachts Designed for Commercial Use*, RINA S.p.A., Genova, Italy, 2017.
2. BOOTE, D, PAIS, T, DELLE PIANE, S., “*Vibration of superyacht structures*”, Proceedings of the 4th International Conference on Marine Structures, MARSTRUCT, 2013.
3. PAIS, T, BOOTE, D, KAEDING, P. “*Experimental and numerical analysis of absorber materials for steel decks*”. Proceedings of 26th International Offshore and Polar Engineering Conference, ISOPE, Rodi, 2016.
4. VERGASSOLA G., BOOTE D., TONELLI A., “*On the damping loss factor of viscoelastic materials for naval applications*”, Ship and Offshore Structures, 2018.
5. IMO Resolution MSC.337(91) “*Adoption of the Code on Noise Levels on Board Ships*” Annex 1 MSC 91/22/Add.1, November 2012.
6. LYON R.H., “*Statistical energy Analysis of dynamic systems. Theory and Applications*”, The MIT Press, 1975.
7. ZHANG J., WANG C., SATO T., “*Advanced Markov Chain Monte Carlo Approach for Finite Element Calibration under Uncertainty*”, Computer aided civil and infrastructure engineering, 2013.
8. GRAGNANI L., TONELLI A., BOOTE D., PAIS T., “*Experimental investigation on the damping coefficient of laminated glass for large yachts*”, NAV 18th International Conference on Ships and Shipping Research, NAV, Lecco (I), 2015.
9. BOOTE, D, PAIS, T., VERGASSOLA G., TONELLI A., GRAGNANI L., “*On the damping coefficient of laminated glass for yacht industries*”, International Shipbuilding Progress, 2017.
10. MSC Software Corporation, “*Nastran User Guide*”, Newport Beach, CA, USA, 2016.
11. BIOT, M., BOOTE, D., BROCCO, E., MORO, L., MENDOZA, VASSALLO, P.N., PAIS, T. “*Validation of a Design Method for the Simulation of the Mechanical Mobility of Marine Diesel Engine Seatings*”, Proceedings of Transport Means 2014 Conference, pp. 1-8, Kaunas University of Technology, Lithuania, 23rd – 24st October 2014.
12. PAIS, T., BOOTE, D., VERGASSOLA, G., “*Vibration analysis for the comfort assessment of a superyacht under hydrodynamic loads due to mechanical propulsion*”, Ocean Engineering, Volume 155, Pages 310-323, February 2018.

ENGINE FOUNDATION RE-DESIGN DUE TO MODIFICATION OF THE SHAFT LINE ARRANGEMENT

(DOI No: 10.3940/rina.2018.ijsct.b1.208)

T Pais, D Boote, G Vergassola, University of Genova, Italy, and **M E Di Iorio**, Naval Architect, Chile

SUMMARY

The on board acoustic comfort is a fundamental condition to be pursued in super-yacht design process in order to meet the requirements of the owner and to allow the crew to work safely. The excitation forces originated by the shaft line can greatly affect the dynamic response of the whole ship structure. Within this context, the implementation of a thrust-bearing block in the shaft line of an existent 46 m long yacht is investigated. The main objective of this work is not to prove the already known advantages of the insertion of a thrust block in the propulsion system, but, rather, to study the adjustment of the original configuration to the variations proposed in the shaft line arrangement. Different possible modifications of the structure are tested on a partial model of the vessel, in order to study the response of the engine block's supporting structure when subjected to selected loads.

1. INTRODUCTION

In a yacht the acoustic energy generated by onboard sources, is transmitted to the surrounding environment by two main transmission paths: air and structures (Biot et al. 2015). This fact gives the name to two different noise categories: air-borne and structure-borne sound. The structure-borne sound influences the acoustic comfort at long distance from the sound source due to the low material damping (Pais et al. 2016, Vergassola et al., 2018). As well known, space availability in motor yacht engine rooms is always very limited. This is particularly true when dealing with small size motor yachts. Thus the implementation of a compact, integrated system thrust bearing coupling to reduce the structure-borne noise becomes a very interesting subject to be investigated

The principal difference resulting from the incorporation of a thrust bearing in the shaft line is that the engine and gearbox are isolated from the forces applied to the shaft. Therefore, the only force transmitted by the engine block to the shaft, is the torque. This difference gives several benefits, such as smaller and lighter components in the engine block, the possibility to use only torsion couplings between the engine and gearboxes, etc. However, the main advantage of the incorporation of a thrust bearing lies in the configuration of the mounting system which connects the components in the engine block to the structure. Without the addition of the thrust block, the mounting system of the engine (or gearbox) needs to be stiff enough to resist to the axial load coming from the shaft. This increased stiffness reduces the capacity of the mounting system to absorb loads generated by the engine and allows its transmission into the structure.

In this research, the thrust block has been implemented into an existent three-decks superyacht built in 2016 by an Italian shipyard. The vessel has a length of 46 meters, a breadth of 9.5 meters, a steel hull with aluminum superstructures, a displacement of 400 tons and the maximum speed of 17 Kn. The hull has a longitudinal structure with web frames every 1400 mm in the middle body and 1200 mm at fore and aft extremities. The ship has been designed and built according to American Bureau of Ships (2014), Bureau Veritas (2012) and Lloyd’s Register (2014) rules.

The addition of the thrust bearing cannot bring by itself significant benefits to the performance of the ship, it needs to be completed not only by an appropriate thrust block, including the coupling connection to the gearbox flange and support configuration but, also, by an appropriate engine block support system. This because the most important advantage of an additional thrust block is that the engine support system is not responsible of resisting the axial load transmitted by the shaft. Therefore, it is designed with the only objective of reducing the noise and vibration generated by the engine (Pais et al. 2018) and to improve the comfort on board the yacht (Boote et al. 2013, Biot et al. 2014).

Then, the original structure was modified into different configurations, each one adapted to one of the different thrust blocks provided by the industry. A part of this work is dedicated to determine the loads that should be taken into account and how to reproduce the way these are transmitted to the structure by the mounting system. The behavior of each modified structure is analyzed and compared with the original version on the base of their stress and strain distribution. These tests are carried out by a numerical computational analysis carried out on finite element models.

2. IMPLEMENTATION OF THE THRUST BEARING IN THE SHAFT LINE

The thrust, acting on the propulsion shaft as a result of the pushing action of the propeller, is transmitted to the ship's structure by the main thrust bearing (Venkatesh 2015). The use of a thrust bearing in the propulsion system allows the rotation of the shaft while it transmits the axial load generated by the propeller (Childs 1993). The sketch of Figure 1 shows the location and relative sizes of the main element of the propulsion system, shaft line and engine block obtained from the construction plans of the yacht.

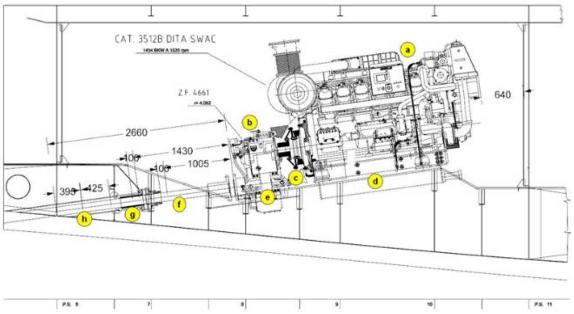

Figure 1 - Side view of the engine room including main elements of the shaft line and engine block

The axial force is transmitted by the propeller and any variation on the propeller's dimensions directly affects the load transmitted to the structure by the shaft. On the other side, the main shaft transmits both the torque generated by the engine to the propeller and the reaction to the thrust generated by the propeller back to the structure. The strut bearing, spring bearings and stern tube keep the shaft and propeller in a fixed position with respect to the ship structures. In order to include the thrust bearing in the shaft line, there are pre-established constraints that must be fulfilled:

- the bulkhead position which limits the engine room;
- the shaft angle of inclination (7.7°);
- the location where the shaft exits from the hull bottom (hull tube).

These constraints comes from the engine room lay out and any variation would implicate heavy interventions on the ship structures inside and outside the engine room. For these reasons, the addition of an element in the shaft line is only possible if there is enough available space. The situation in the engine room of the study case yacht is shown in Figure 1:

- the available space between the engine and the forward machinery space bulkhead is 640 mm. This reduces the possibility of displacing the engine forward unless the bulkhead is displaced as well;
- the distance from the gearbox flange to the aft E.R. aft machinery space bulkhead is about 2600 mm;
- if there are no structural modifications the available space is limited by the position of the deep-sea seal. As a 100 mm minimum working distance needs to be left after the forward end of the seal, the total potential space to locate the thrust block is reduced to 1005 mm;
- if we consider that the maximum backward displacement of the deep-sea seal is 425 mm, the available space is increased to 1430 mm till the forward minimum working distance.

Despite all previous considerations the engine room allows a limited but sufficient space to make the incorporation of a thrust block in the shaft line possible. Taking into account the restrictions recommended by the shipyard technical office, structural modification become necessary to increase the available space.

3. THE ENGINE ROOM

The analysis performed in this study are addressed to provide a comparison between the performance of the foundation of the original structure and the proposed modifications. The structural response of the actual and modified foundations is studied from the reaction to the forces generated by the:

- *component weight*: generated by the main components supported by foundations (engine, gear box, couplings, etc.);
- *torque*: generated by the engine and the gearbox;
- *thrust*: transmitted through the shaft to the respective resisting element (gearbox or thrust bearings).

The engine used in this study case corresponds to a 3512B DITA SWAC from Caterpillar. At the nominal the pre-established nominal speed of 16 knots, the engine should provide 1454 kW at a rotational speed 1830 RPM. The gearbox corresponds to a ZF-4661, with a engine-gear box ratio of 4.062.

3.1 WEIGHT

The Engine's total weight (W_{eng}) is 88.24 kN. This value takes into account the "dry" weight of the engine with an additional 35% related to the operating fluids and fuel. The weight of the engine-gearbox coupling ($W_{couple\ E\text{-}GB}$) is shared between the engine and gear box supports. The weight acting on each support system can be approximated as half of the total coupling's weight. The total weight of the couple used in this study case (Vulkardan E) is 3.2 kN. For each of the four mounting elements, the total vertical weight load ($W_{T\ eng}$) will be:

$$W_{T\ eng} = \frac{W_{eng} + {}^{W_{couple\ E-GB}}/_{2}}{4} = 22.5\ kN \qquad (1)$$

The torque generated by the engine T_{eng} at nominal speed, can be estimated by using the following relation between the engine's power at nominal rotation speed P_{eng} and the nominal rotation speed of the engine ω_{eng}.

$$T_{eng} = \frac{P_{eng}[KW] \cdot 9.55}{\omega_{eng}[rpm]} = 7.57\ [kN \times m] \qquad (2)$$

The force transmitted to the resilient mounts $F_{T\ eng}$ by the engine's torque is estimated by using the distance between opposite mounts d_{eng} as the lever. In Figure 2 the transition of the torque to one of the resilient mounts (left) and the force (F) applied on the opposite mount due to the distance between them is shown.

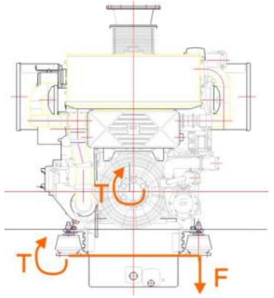

Figure 2 - Estimated force on the supports generated by the engine's torque

Then, the force applied on the resilient mounts depends on the transversal distance d_{eng} between supports at each side of the engine, divided by the number of elements in the support. In the following Figure 3, it is possible to see the lever distance considered for the engine and the gearbox.

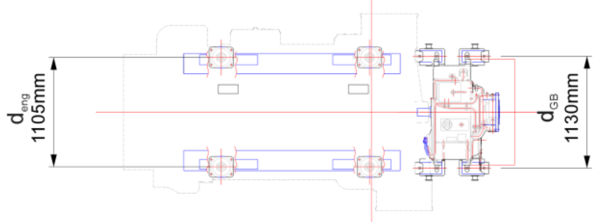

Figure 3 - Distance of the engine supports d_{eng} and of the gearbox supports d_{GB}

In the case of the engine, the force generated by the torque $F_{T\ eng}$ is obtained using the following relationship:

$$F_{T\ eng} = \frac{Torque}{d_{eng}\cdot n^{\circ} elements} = \pm 3.42\ kN \qquad (3)$$

The force acting on each support is divided between the resilient mounts (in this case, two elements on each side of the engine). Depending on the direction of the shaft rotation relative to the position of the resilient mount, this force will present the same or opposite direction of the weight. The force on each resilient mount results from the contribution of the weight and the torque force:

$$R_{eng} = W_{T\ eng} \pm F_{T\ eng}\ k\ N \qquad (4)$$
$$R_{eng+}=25.89\ \text{kN} \qquad (5)$$
$$R_{eng-}=19.049\ \text{kN} \qquad (6)$$

R_{eng+} refers to the resultant force of the resilient mounts when the added torque force $F_{T\ eng}$ has the same direction as the weight $W_{T\ eng}$. In the case of R_{eng-}, the direction of the $F_{T\ eng}$ is opposite to the $W_{T\ eng}$, and therefore should be subtracted.

The forces acting on the gearbox's support are calculated taking into account the same considerations valid for the engine. Gearbox's total weight W_{GB} is obtained from the gearbox dry weight, 22.95 kN. The gearbox total weight should then be increased by half engine-gearbox coupling $\left({W_{couple}}/{2} = 1.6\ kN\right)$.

In this case the weight of the shaft between the hull tube and the gearbox flange is added as well; the shaft total weight is 2.03 kN. Therefore, the total weight applied to the gearbox's support system is:

$$W_{T\ GB}=W_{GB}+W_{couple}+W_{shaft}=24.55\ \text{kN} \qquad (7)$$

Then, the weight applied on each side of each support is $W_{T\ GB}/2 = 12.27$ kN

3.2 TORQUE

The force generated by the torque on each support is obtained by the following Eq.8. It is possible to see that the torque is "r" times the torque in the engine:

$$T_{GB} = \frac{P_{eng}[KW]\cdot 9.55}{\omega_{eng}[rpm]}\cdot\frac{1}{1/r} = T_{eng}\cdot r = 30.73\ [kN\times m] \qquad (8)$$

The same equation 3 can be used to obtain the forces transmitted by the gearbox torque T_{GB} to each support $F_{T\ GB}$:

$$F_{T\ GB} = \frac{T_{GB}}{d_{GB}\cdot n^{\circ} elements} = \pm 27.20\ kN \qquad (9)$$

By using equation 4, it is possible to estimate the resultant force R_{GB} applied on each side of the gearbox:

$$R_{GB} = W_{GB} \pm F_{T\ GB}\ kN \qquad (10)$$
$$R_{GB+}=39.47\ \text{kN} \qquad (11)$$
$$R_{GB-}= -14.92\ \text{kN} \qquad (12)$$

Unlike the engine supporting elements, the supports on one side of the gearbox will be subjected to a compression load R_{GB+} and the other under tension R_{GB-}. This because:

- the gear box is almost 4 times lighter than the engine, being $\frac{W_{ENG}}{W_{GB}} = 3.84$;
- the torque transmitted by the gear box is more than 4 times the torque transmitted by the engine, being$r = 4.062$.

As a result, the torque-generated force $F_{T\ GB}$ applied on the supports is higher than the contribution of the gearbox weight W_{GB} and the direction of the resulting force changes. In such case, it is necessary to use resilient mounts that are able to resist to both types of loads.

3.3 THRUST

In the working condition of 16 knots, the total thrust T_h at each shaft is 100 kN. The applied thrust on each support of the gearbox is then $T_h/2=50$ kN. Taking into account that the shaft inclination angle is 7.7°, it is possible to decompose the force into:

- a component parallel to the resilient mount axis: T_{hv}= -T_h sine (7.7°)= 6.69 kN;
- a component perpendicular to the resilient mount axis: T_{hh}= -T_h cosine (7.7°)= 49.55 kN.

The thrust force is usually neglected when performing a pre-selection of the resilient mounts of the support system, because the predominant component of the force is generally perpendicular to the direction of the element. However, the vertical component of the thrust load T_{hv} is in this case almost half of the contribution of the gearbox's weight on each support $W_{GB}/2$=12.27 kN.

3.4 RESILIENT MOUNT SELECTION

The resultant force applied on the resilient mount will generate a deflection. Once loads acting on the supports are known, it is possible to pre-select the resilient mounts to be used on the base of its desired maximum deflection. Considering only the static load, the mount displacement y_0 depends on its static stiffness k.

$$y_0 = \frac{Resultant\ Force}{k} \tag{13}$$

It is important to distinguish between the static stiffness from the rubber hardness. The first item corresponds to a property of the resilient mount element as a whole, while the second corresponds to a specific property of the element elastic material. The dynamic behavior is influenced by the elastic and damping characteristics of the system and will determine the transmissibility of the system.

3.4 (a) Transmissibility of the resilient mounts

When a harmonic force $F_{applied}$ is applied to the system with a frequency f_F, it will be transmitted to the foundation $F_{foundation}$ through the supporting elements (Harris 2002). The ratio of the applied force versus the transmitted one is called transmissibility $TR_{f\text{-}a}$ and it will depend on the relation between the frequency of the applied force f_F and the natural frequency of the system f_0. This last one is called frequency relation (β):

$$TR_{f-a} = \frac{F_{foundation}}{F_{applied}} \tag{14}$$

$$\beta = \frac{f_F}{f_0} \tag{15}$$

If the foundation is considered perfectly rigid, the applied force can be analyzed in terms of the deflection of the mounting element. In other word, the force transmitted to the foundation will be considered equal to the force applied on the supports which depends of the deflection. The varying force will generate a variation of the displacement from its static position, and the transmissibility can be defined as:

$$TR_{f-a} = \frac{Amplitude\ of\ the\ dynamic\ displacement}{Amplitude\ of\ the\ static\ displacement} \tag{16}$$

The main objective in the design of the support system is to minimize the force transmitted to the foundation from the applied force by reducing as much as possible the dynamic motion of the supported masses. In Figure 4, a typical transmissibility graph $TR_{s\text{-}a}$ (β) is shown. This graph can be interpreted as the response of a system with a particular natural frequency f_0, to different frequencies of the applied force β(f_F) Each curve corresponds to systems with different characteristics. In this case, the difference resides in the damping coefficients ξ.

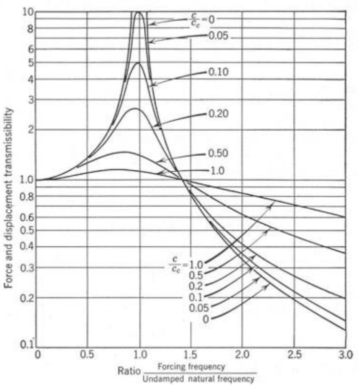

Figure 4 - Transmissibility $TR_{s\text{-}a}$ (β) (De Silva 2007)

Independently on the damping coefficient, the force transmitted to the foundation is equal to the applied force $TR_{s\text{-}a}$=1 at $\beta = \sqrt{2}$. This fact limits the two possible behavior of the system depending on the value of β:

- if $\beta < \sqrt{2}$, there is an amplification of the applied force. The force transmitted to the foundation is maximum when the frequency of the excitation force is equal to the system's natural frequency (β=1) and the system achieves resonance. When using higher damping coefficients (ξ) it is possible to reduce the maximum transmissibility values at the resonance frequency;
- if $\beta > \sqrt{2}$ there is an attenuation of the transmitted force, with respect to the applied force. In this case, when increasing the damping coefficient, it reduces the attenuation capacity and the transmitted force is increased.

In order to validate the selection of a particular resilient mount, it is necessary to analyze the transmissibility of the system composed by an element (engine, gearbox, etc.) elastically supported on a perfectly rigid foundation. This analysis is usually performed by the supporting system providers using special computational tools and specific knowledge and information and is beyond the aim of this work. Moreover, it is difficult to anticipate the influence of the system's dynamic response on the structure before performing any modifications.

The resilient mounts and supporting structure configurations designed and proposed by the same companies that provides the thrust bearing scheme.

4. THE MOUNTING SYSTEM CONFIGURATION

4.1 THE ORIGINAL CONFIGURATION

The following Figure 5 shows the configuration of the engine block after the shaft. Highlighted in red it is possible to see the main connections between the engine and gearbox (engine-gearbox coupling) and to the rigid foundations (resilient mounts).

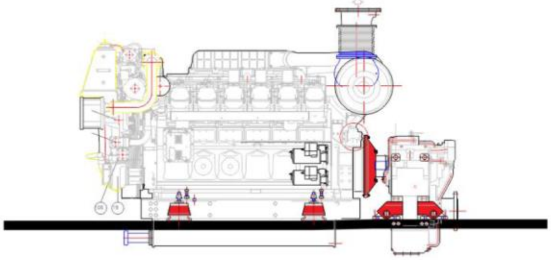

Figure 5 - Original configuration of the engine block of the study case

In the case of the original configuration, the engine and gearbox are connected rigidly by the coupling's cover.

4.1 (a) Engine support system:

The engine is mounted on a rail at each side (Figure 6, left). The rails are connected to the structure through highly elastic mounts corresponding to the conical T-Series. This type of mount is used to prioritize insulation and noise reduction. Rubber is used as resilient material and is glued between conical rings (Figure 6, right).

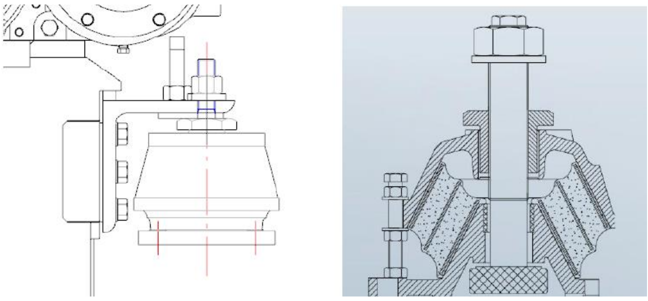

Figure 6 - Sketch of the configuration of the engine support (left), provided by technical office. Conical T-Series resilient mount (right)

4.1 (b) Engine-Gear box coupling:

This component is responsible of transmitting the power generated by the engine into the gearbox. The used couple is a Vulkardan type E. It is a highly-flexible rubber coupling for free standing installations. It is optimized to compensate radial misalignments and it is able to give the best performance especially in flexible mounted engine installations. Four rubber qualities are available in order to tune the coupling to the various system requirements.

4.1 (c) Gearbox support system:

The gearbox is mounted on four semi-elastic mounts fixed to the foundation. These elements are responsible of transmitting the axial load held by the gearbox to the structure. In Figure 7 the mounting elements, corresponding to the AVR Series mounts, are shown. The resilient material presents higher static stiffness in order to resist the applied axial thrust load.

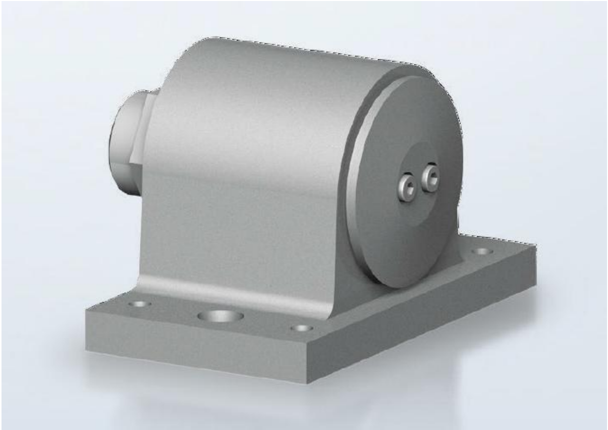

Figure 7 - The gearbox support

4.2 THE NEW CONFIGURATION WITH THRUST BEARING

The only alteration of the engine block support after the addition of the thrust bearing in the shaft line is the mounting type. In Figure 8, the new configuration of the engine block is shown.

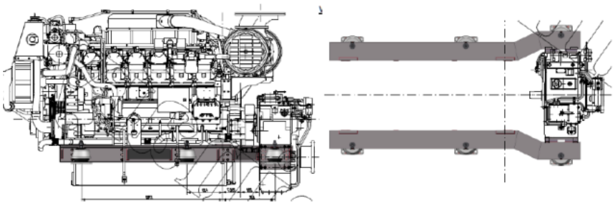

Figure 8 - New configuration of the engine block

Unlike the original configuration, the stiffness of all the resilient mounting elements is the same. This type of supporting system configuration totally distributes the force and torque between all elements. The force generated from the gearbox increased torque may generate a tension resultant force on some or all the mounting elements. The potential tensional loads need to be taken into account when choosing the type of resilient mount.

At the same time, the resultant weight of the whole engine block increases the compression found in the resilient mounts below the gearbox. If the stiffness of each resilient mount element is not appropriately calculated, the force may not be equally distributed between the elements. This could generate overloading that can eventually destroy the support and damage the structure.

5. THRUST BLOCK

Two different thrust block configurations have been proposed in order to connect the selected thrust block to the structure. One uses extensions at sides of the thrust bearing to bolt it to a keelson's flange (Solution A) and the other using a cover around the deep-sea seal to bolt the flange to a transversal member (Solution B). In Figure 9, the two proposed solutions are positioned in the engine foundation structure of the actual ship.

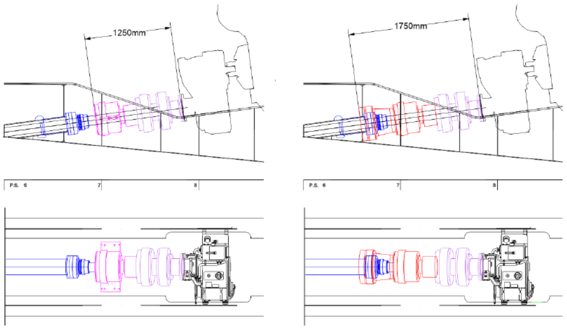

Solution A Solution B

Figure 9 - Solution A (left) and Solution B (Right) are positioned on the original structure (side view and top view)

The main geometric characteristic that differentiates this two thrust blocks is the overall length including the marine coupling (1250 mm), making it necessary to move the engine forward or the deep-sea seal backwards. In our study, only the position of the deep-sea seal was moved backwards in order to reduce modifications to a minimum.

Another type of proposed thrust bearing is the V Solution, and it is shown in Figure 10. One of the most distinctive features of this thrust block resides in the configuration of the coupling between the thrust bearing and the gearbox flange. This coupling presents a set of resilient mounting elements arranged radially around the coupling and are responsible of transmitting the torque, maintaining the shaft alignment and absorbing the axial vibrations transmitted by the shaft.

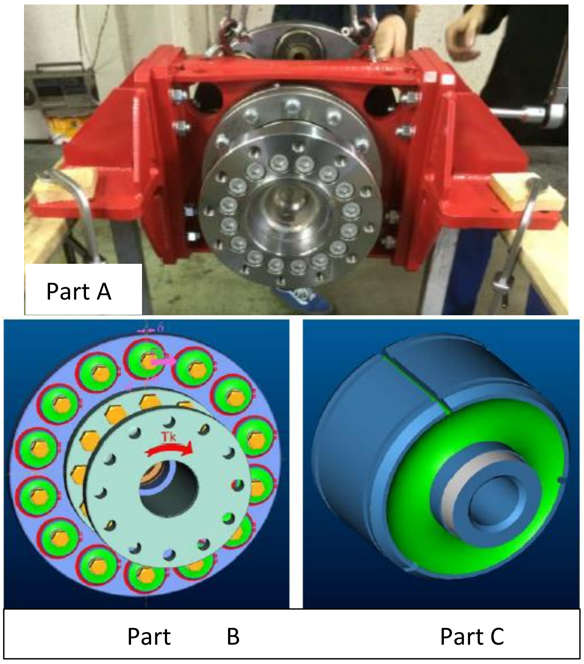

Figure 10. Coupling arrangement (Part A), plate arrangement (Part B) and resilient mount element (Part C) used in the Solution V

Given that the chosen thrust bearing is able to resist the pre-defined axial load coming from the shaft, the characteristics of the thrust block depends more on the performing conditions of the coupling rather than on the actual bearing. The characteristics of the thrust block will depend on:

- number of rows: different number of plates (where the resilient mounts are arranged) can be position next to the other. By increasing the number of rows, the rigidity of the connection to the gearbox is reduced. This benefits the vibration absorption but can jeopardize the torque transmission to the shaft. In our case, two sets were used;
- number of "bushes": refers to the number of resilient mounts per coupling plate. The amount of used elements affect the stiffness of the coupling as a whole element;
- resilient mount characteristics: this is defined by the type of resilient element (in this case rubber) used for the mounts. It includes the torsional static and dynamic stiffness [kN×m/rad], the angular static stiffness [kN×m/rad], the axial static stiffness [kN/mm] and radial stiffness [kN/mm].

The supporting elements of this particular thrust block are independent from the main bearing. This allows to vary the configuration and shape of the thrust block in order to adapt the connection to the supporting base. The following Figure 11 shows an exploded 3D view of the main elements that compose the thrust block highlighting in red the supporting elements, that can be replaced according to existing structural configuration.

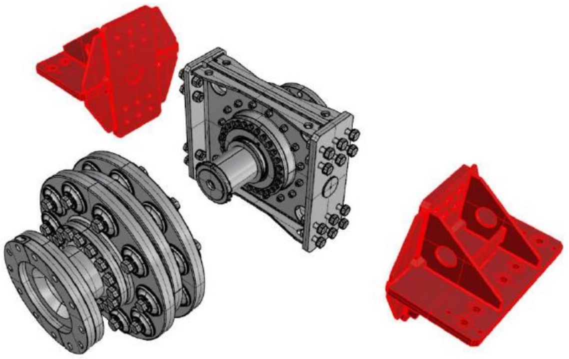

Figure 11 - Thrust block Solution V exploded in a 3D view. Thrust bearing (middle grey), gearbox couplings (forward grey) and supporting elements (sides red)

5.1 THRUST BLOCKS COMPARISON

The three chosen thrust bearings differ each other mainly in the longitudinal position where the force is transmitted to the structure. This gives a wide range of structural modifications when considering the addition of the bearing on other projected ships. In Figure 12 the mid position of the thrust load transmission to the structure from the shaft line is reported:

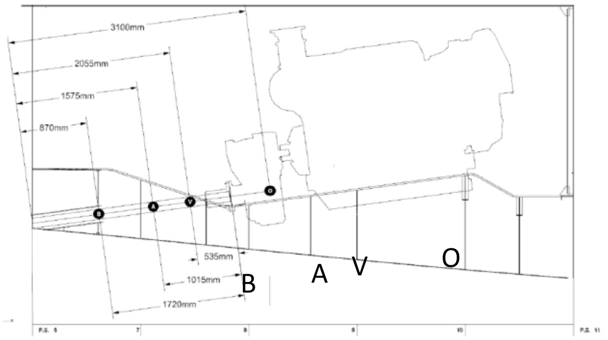

O: the original configuration;
A: the first proposed solution;
B: the second proposed solution;
V: the third proposed solution.

Figure 12 - Position where the thrust load is transferred to the structure (middle point between the supports)

It is possible to see how the different solutions move the thrust load of application closer to the aft bulkhead (2210 mm of maximum difference in Solution B). This changes the length of the section that is under compression, modifying the response to the combination of the axial load and perpendicular forces. Another aspect that can be noted is the available vertical space between the shaft and the hull that is reduced by the displacement of the point of application of the load.

6. PROPOSED STRUCTURAL MODIFICATIONS

There are always different possible variations of the structure to be performed because of the addition of a new component. The solutions studied in this work were the ones that minimized the differences with the original version.

6.1 MODIFIED SOLUTION A

The main obstacle to overcome when considering the use of this type of bearing block is related to the vertical position of flanges. If it is intended to be bolted on the main keelson of the foundation before the engine block, the distance d_{tb} (see Figure 13) between the flanges and the hull is reduced. This is not beneficial for the longitudinal stiffness as the web's height needs to be reduced to adapt to the position of the flange. Moreover, as four of the five main stiffeners are reduced in dimensions, the inertia of the overall section is reduced as well. This jeopardizes the hull girder longitudinal resistance to global loads. The minimum web height recommended by common practice for this particular case is 500 mm. The most critical situation corresponds to the outer main keelson (2150 mm from middle ship). In the original structure, the minimum web height is 405 mm before the position of the gearbox mounts (d_{min} in Figure 13).

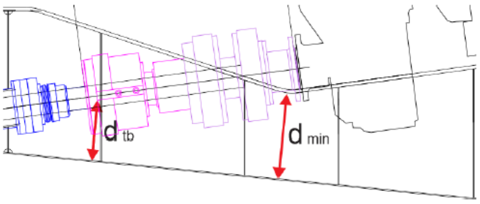

Figure 13 - Shortest distance (d) between the thrust block flange and the hull

For this particular case, the d_{tb} is less than 250 mm before the TB's flange, less than one half of the recommended minimum height. This caused to apply other type of solutions such as the addition of internal longitudinal supports.

In our case, it has been proposed the use of internal secondary keelsons between the main stiffeners of the foundation, where only the thrust block would be supported. This simple solution present other construction obstacles. The transversal distance between the original and the added keelsons was not enough to allow the welder to reach the the hull and web junction. The optimum welding angle recommended by shipyard technical office is 45°. When adding the "inner" stiffeners to the original structure, the available welding angle is much less, making it necessary to move the main stiffeners away from the shaft. In Figure 14, it is possible to see how the available welding angle is increased when the engine foundation keelsons are moved 150 mm away from their original position.

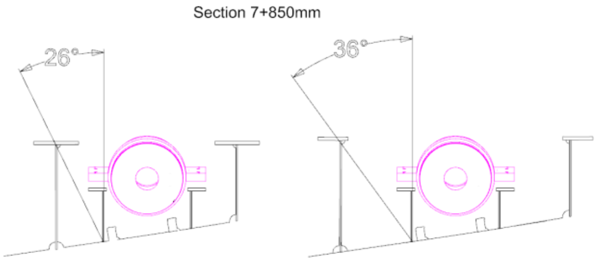

Figure 14 - Maximum welding angle between keelsons on section 7+850 mm. Original structure (left) and proposed modification (right)

The inner structure used to support the bearing extends from the engine room's aft bulkhead (at section 6) to the transversal section 7+850 mm. It was necessary to modify the main keelsons to assure sufficient space for welding between these sections. In Figure 15, the flange of main foundation keelsons has been reduced from 290 mm to 200 mm between the frames where the thrust bearing support is located (Frame 6 to Frame 7+850 mm). This provides additional space to allow correct welding.

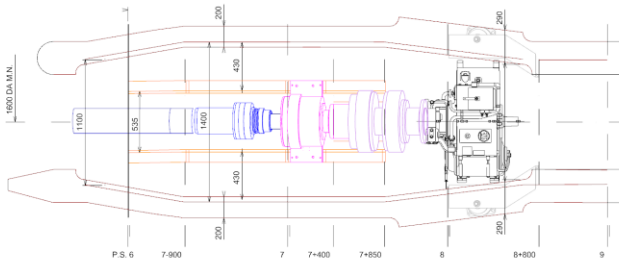

Figure 15 - Top view of the modified engine's foundation for Solution A

The addition of the thrust block between the main keelson required a reduction of the existing transversal frame's height in order to adapt to the thrust bearing's shape and leave sufficient space between the frame's flange and the rotating elements. This reduces the frame's stiffness and the strength of the overall hull section. In order to compensate the resistance loss of the structure, a transversal frame between sections 7 and 7+850 mm has been added; Figure 15 shows the location of the added frame is reported. In addition, the frame 7-550 mm was moved 350 mm backwards, following the re-positioning of the deep-sea seal in order to fit the thrust block in the shaft line. The shape of this frame was modified to be adapted to its new location and to the geometry of the bearing in addition to the main and inner keelson modifications. These modifications are shown in Figure 16. The general shape and plate thicknesses are the same but the frame is wider due to the position of the main keelsons. In Figure 16 it is also possible to see how the general shape of the main keelson located at 1600 mm from the mid ship (above the position of the shaft) is modified in order to adapt to the frame shift and to the intersection with the hull tube. It also shows how the web height of Frame 7 is reduced to one half of its original size in order to present sufficient space between the bearing.

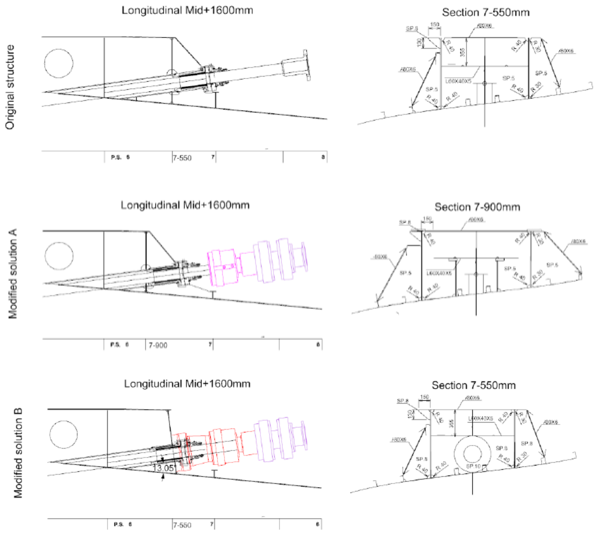

Figure 16 - Side view of original main keelson located at 1600 mm from mid ship (top-left) and section 7-550 mm of the original structure (top-right); proposed Solution A (middle) and proposed Solution B (bottom)

6.2 MODIFIED SOLUTION B

In this solution, the thrust block is bolted at the back end using a rigid cover as a cantilevered beam. In Figure 16 (bottom left), it is possible to see that the general shape and longitudinal position of the frame is the same as the original structure, with the following modifications:

- the frame where the block is connected has been tilted 7.7° in order to be perpendicular to the direction of the shaft and thrust load;
- the main keelson located at 1600 mm from mid ship does not reach the following frame 7;
- the plate thickness is increased to 8 mm in all frame's platings;
- a cylindrical flange of 10 mm thickness is located in the frame where the block's cover should be bolted.

This solution presents different construction obstacles with respect to the previous one. The available space below the block's bolted flange at frame 7-550 mm (see Figure 16) is minimum. This is not advisable from a constructive point of view as there is no sufficient space to bolt the cover to the flange. Moreover, stress can concentrate close to the hull's plate. In order to increase the vertical space above the hull the thrust block and engine block should be moved forward from the proposed position. With a relative inclination angle between the shaft and hull of 13°, the blocks should be displaced 1meter to achieve a 225 mm gap between the bolted flange and the hull, which is the minimum gap recommended by the provider. This makes it necessary to move the forward machinery space bulkhead of the engine room located at section 11 to fit the engine inside.

However, the deep-sea seal needs to be connected to forced external lubrication and refrigeration. The use of an external cover around the seal was not welcomed by shipyard, as it limits the access for maintenance and control. The mentioned obstacles make this solution unfeasible for this particular ship. Despite this, it was tested by numerical analysis presenting interesting advantages related to the stress distribution on the main keelson of the structure.

6.3 MODIFIED SOLUTION V

The main difference between the third thrust block with respect to the first two blocks is that it reduces the amount of structural modifications necessary to perform the foundation adaptation. The thrust block's combined length (thrust bearing and coupling) of 800 mm is 2/3 of the shortest version A and B (Solution A - 1250 mm and Solution B - 1820 mm). In Figure 12, it is possible to see how this allows moving the thrust block supports towards the gearbox connection flange. As the thrust bearing is positioned 0.5 meters forward with respect to Solution A, it allows to consider mounting the thrust block on the same foundation as the gearbox and engine. This is possible because the web height reduction is not as significant as in the proposed Solution A. In the following Figure 17, the relative distance between the middle point of the thrust load application and the hull is 100 mm larger. Nevertheless, the web height for this solution would be also below 500 mm.

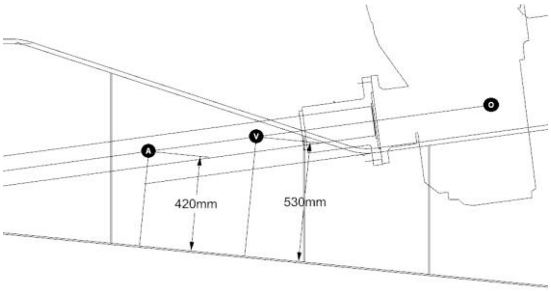

Figure 17 - Distance between the middle point of the thrust load application and the hull, for Solution A and Solution V cases

These two aspects allows performing a less invasive and more flexible structural modification when considering the incorporation of the thrust block in an existing design. In Figure 18 the Solution V is shown.

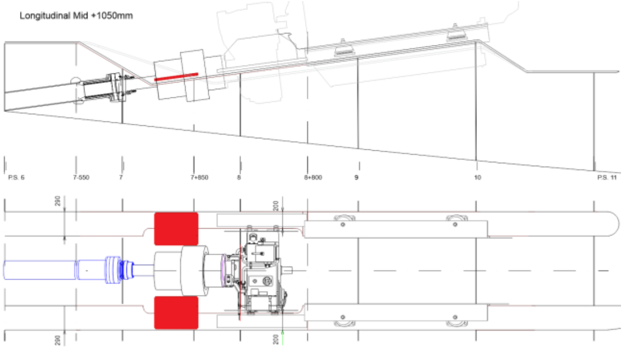

Figure 18 - Side view (top) and top view (bottom) of the modified engine's foundation for trust bearing Solution V

The presented modifications are simple, as only the height of main keelsons of the foundation are redesigned so that the engine, gearbox and thrust block are supported on the same "ski". In Figure 18 (top) side view of the original flange shape is represented in light grey. The new flange is moved 85 mm up so that it adapts to the thrust block and gear box supporting element position. A 30 mm gap is left between supports and the flange for the insertion of chock fast and plates. In addition, the flange is extended more than 700 mm backwards as far as the end of the thrust block's support. These modifications are simple but they present some disadvantages with respect to the original configuration. The two flange's curvature angle between frames 7-550 mm and 8 are increased of more than 10°. There is not sufficient space before the location of the thrust block support and the transition curvature is not smooth enough. These jeopardizing conditions were chosen to test the structure under a "worst case scenario" but keeping the main keelson's web within a reasonable height. However, for the case of the main keelson located at 2150 mm from the mid ship, the minimum web height is reduced to 350 mm, while in the original structure this distance is 405 mm.

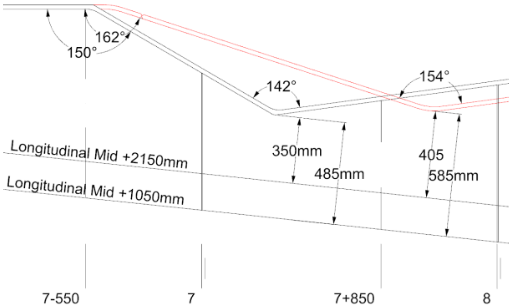

Figure 19 - Superposed side view of the foundation's main keelsons between frames 7-550 mm and 8. The red line is the original flange shape and the grey line is the Solution V

Different solutions are considered to adapt the existing structure to the incorporation of the proposed thrust bearing in the shaft line. From the selected candidates, the thrust block Solution V results more beneficial for this particular study case as it requires a less invasive structural modification.

7. FINITE ELEMENT MODEL

In order to perform accurate and reliable FEM calculations a detailed numerical model of the engine room of the yacht structures has been realized by Patran & Nastran, MSC Software (MSC 2014); the result is shown in Figure 20. The hull geometry and structure lay out has been imported from a 3D model previously created by a rendering software. The mesh was created using shell elements for plating and main reinforcements such as keelsons, floors and girders. For secondary stiffeners simple beam elements have been preferred to keep the model dimension within reasonable dimensions.

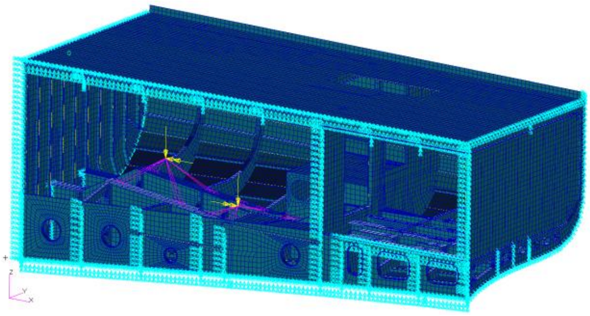

Figure 20 - The engine room model

The loads are transmitted from the application points to the structure in the different modified configurations by the rigid link elements. In the FE software, they are called as "MPC" and use RBE2 rod elements (Nastran library) to connect the only "independent" node where the load is applied to all the "dependent" nodes that transmit the load to the structure (MSC 2013). In the previous Figure 20, they are represented by light blue symbols.

7.1 LOAD

Due to the shape of modelled structure and the nature of the forces acting on it, the approach of the analysis has been "inspired" based on the ultimate strength of stiffened panels, proposed by O. F. Hughes (1988). In his work, Hughes analyses the possible mechanisms of collapse of longitudinally stiffened panels by applying compressive axial load in combination with the perpendicular load. Under this type of compressive load, the panel is essentially a group of symmetric columns, each consisting of a stiffener and a plate flange of effective width.

There are certain important differences between the way loads are applied in Hughes simplified approach and our study case:

- the lateral loads applied on the stiffener's flange corresponds to point loads (coming from the weight of the engine, gearbox, bearings, shaft, etc) instead of distributed ones;
- the axial load is applied as a point load at a certain longitudinal position of the stiffeners. This generates compression only on one section of the keelson (between the point of application of the thrust and the forward machinery space bulkhead) and the other in tension (between the point of application of the thrust and the backward bulkhead);
- the axial load is not applied on the whole section, but to a vertical position different from the location of the stiffener's neutral axis height, generating a flexural moment on the stiffener section.

In Hughes' study there are different collapse modes depending on the combination of applied loads:

- mode I: compression failure of the stiffener. Combination of load 1 and 3;
- mode II: compression failure of the plating. Combination of load 2 and 3;
- mode III: compression failure of stiffener and plating. Combination of load 2 and 3.

The hydrostatic pressure generated on the stiffener's plates is not considered in this study, then modes II and III are discarded as possible collapse behaviors. However, the load combination of the study case can be compared with the loads applied on the collapse mode I.

From the performed analysis, the longitudinal stress distribution on the main keelson of the engine foundation is compared with different structures. In the same way as the material yield stress is compared with the von Mises combined stress, an acceptance criteria for buckling needs to be defined. This way it is possible to determine if the buckling capability of plates and stiffened panels are within acceptable limits. This limit was determined by the critical buckling load of stiffener's section (Patnaik 2004).

8. ANALYSIS OF RESULTS

The prediction proposed by the combined approach let us define that most critical points at each section of the foundation main keelsons is located on the web between the neutral axes and flanges. It has been decided to compare the strength of the different solutions on the base of the stress and deformation values reported on an imaginary line that crosses the foundation keelsons. This line is located on the web 150 mm below the flange. In Figure 21, the location of this imaginary line drawn in a red dashed line on the main keelson at 2150 mm from the middle of the ship (F.M.S) of the original structure, is shown.

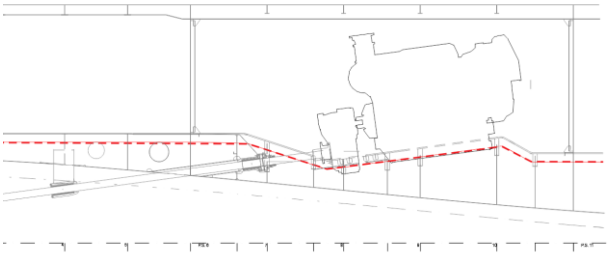

Figure 21 - Stress and deformation measurement location (red dashed line) referred as "vulnerability line"

The following Figure 22 compares the stress (X-component) distribution along the same keelson (located at 2150 mm from the midship) of the original structure, but under different loading conditions. In the first plot (top) only the axial thrust load is applied, while on the second plot (bottom) the engine's block's weight and torque is added to the thrust load.

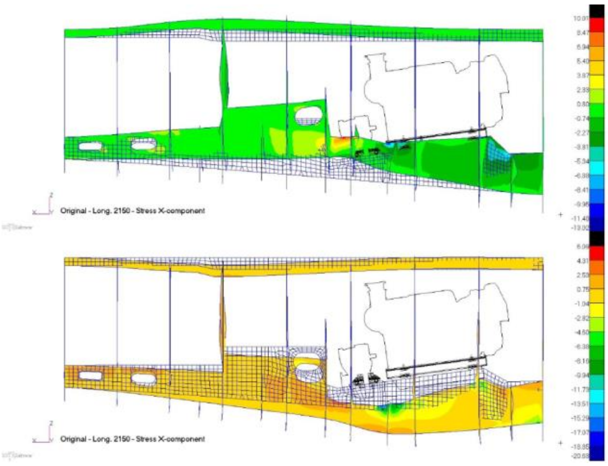

Figure 22 - Longitudinal stress distribution (MPa) on Keelson at 2150 mm from mid ship. Under thrust load (top) and under thrust, weight and torque loads (bottom)

These figures shows that without the addition of the forces transmitted by the engine block, according to the distinction made by the combined approach, the deformation of the keelson is not negative (towards the hull plates). In fact, the upward vertical component of the thrust load tends to "bend" the foundation keelson "positively", allowing the failure to be generated by Modes I and II.

In the graph of Figure 23, the stress (X component) reported at the "vulnerability line" on the main keelson located at 2150 mm from mid ship, for the two load cases, has been plotted. In the first case, only the thrust is taken into account, while, in the second one , the thrust, weight and torque are applied as well.

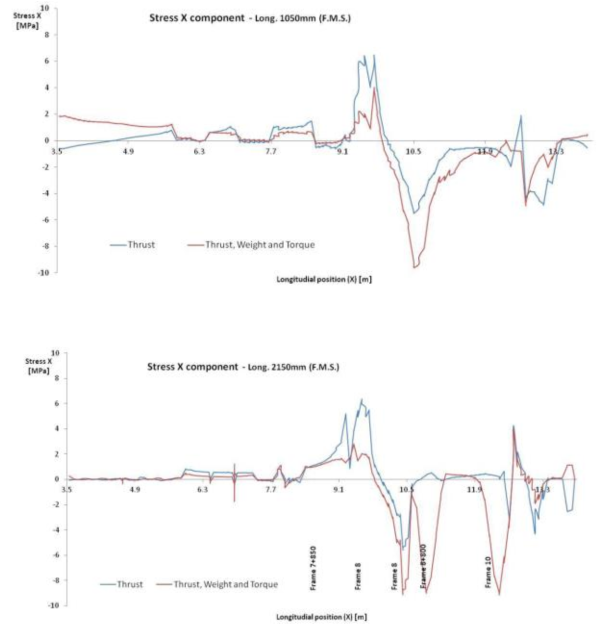

Figure 23 - Longitudinal stress distribution along vulnerability line of the main keelson located at 1050 mm F.M.S (top) and 2150 mm F.M.S (bottom)

It is possible to see that the position of the maximum values of the two loading conditions differ each other depending on the longitudinal position where the forces are applied. However, the maximum resulting values present the same order of magnitude in both cases. In the case of simple thrust, load is between -6 MPa (compression) and +6 MPa (tension) which gives an amplitude Δ equal to 12 MPa. Appling the thrust, weight and torque loads the magnitude is between -10 MPa (compression) and +2 MPa (tension). This gives a Δ=12 MPa.

In Figure 23 the approximate position of frames of the original structure has been included. It is possible to see that the longitudinal position of the reported peaks are coincident with the frame position. This is due to the fact that the frames provides a barrier where stress (compression and tension) concentrate.

After that the longitudinal stress distribution along the "vulnerability lines" of the main keelson located at 2150 mm from mid ship of the modified solutions has been calculated. Figure 24 shows the longitudinal stress (X) distribution reported on the main keelson elements located at 2150 mm for Solutions A, B and V F.M.S.

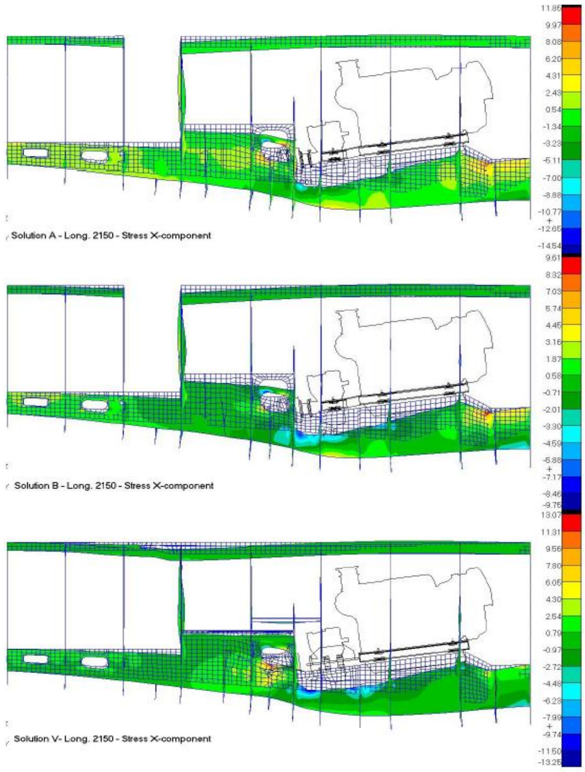

Figure 24 - Side view of the stress (MPa) distribution on keelson at 2150 mm FMS of the modified proposed solutions: Solution A (top), Solution B middle and Solution V (Bottom)

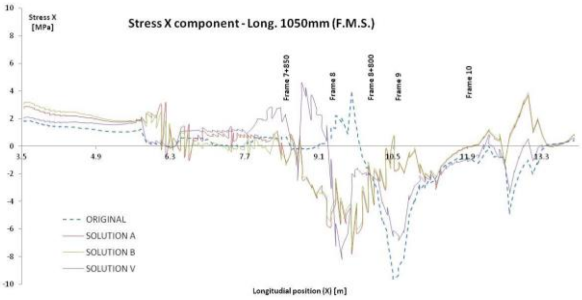

Figure 25 - Longitudinal stress distribution along the vulnerability line of the main keelson located at 1050 mm (F.M.S) of the original and modified structures (Solutions A, B and V)

From these last images, it is possible to find significant similitudes in the stress distribution between the different shaped keelsons. The maximum and minimum stresses present the same order of magnitude. The lowest stress (compression) reported is -17 MPa (Solution A) and the highest stress (tension) reported is (14 MPa).

There is a stress concentration point between the frame 7+850 mm and frame 8. The stress peak is located where the stiffener web presents a minimum height of 405 mm and a web height variation. This peak is close to the stiffeners flange, as predicted by Hughes approach.

The stress distributions shown in Figure 24 confirms that maximum and minimum longitudinal stress values are found closer to the main keelson flange. Using the same methodology adopted for Figure 23, the longitudinal stress is reported for the original and for the three modified foundations at the "vulnerability line" on the main keelsons located at 1050 mm F.M.S. (Figure 25) and at 2150 mm F.M.S. (Figure 26).

In Figure 25 and 26 it is possible to see that the position of the minimum (compression) and maximum (tension) values are shifted from their original longitudinal position as well. This is mainly due to the fact that the longitudinal position of the points of thrust load application have been moved as well displaced.

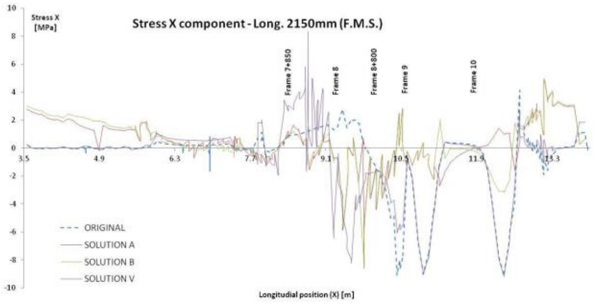

Figure 26 - Longitudinal stress distribution along vulnerability line of the main keelson located at 2150 mm (F.M.S) of the original and modified structures (Solutions A, B and V)

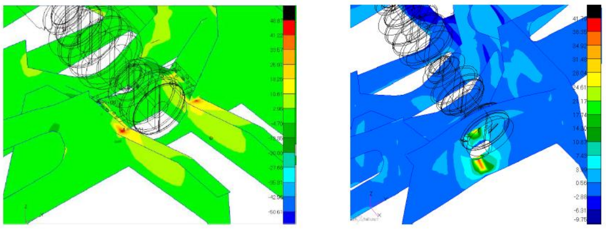

Figure 27 - Longitudinal stress distribution (MPa) and position of the thrust block. Solution A (left) and Solution B (right)

Particularly in Figure 26 (Keelson 2150 mm F.M.S) the first observable maximum is reported from the longitudinal stress distribution of Solution V. This peak is again present between the Frame 7+850 and Frame 8 where the supports of the thrust bearing is located. Moreover, the bearing supports are bolted on the same main keelson where the stress values where highlighted. The longitudinal stress distributions along the "vulnerability line" of the main keelsons of the modified Solutions A and B do not report any maximum or minimum values at the same location where the thrust are positioned (Solution A, between frames 7 and frame 7+850 mm and Solution B at Frame 7-550 mm). This because the bearing is not directly supported by the main keelsons. In these proposed modifications, the load is transmitted by the secondary structural elements, such as the inner keelsons for Solution A (Figure 27 left) or the transversal relocated at 7-550 mm (Figure 27 right).

In Figure 27, the longitudinal stress distribution on the secondary elements proposed for the modification of the foundation is shown. The maximum and minimum longitudinal stress reported are 10 times greater than the maximum values reported on the intersection profiles. This correspond to concentration points generated in correspondence of the application points of the thrust load. In Solution A, the concentration point is found to be before Frame 7 where the inner longitudinal web varies its height (Figure 27 left). In Solution B, the stress peak is found on Frame 7-550 mm (where the bearing is bolted) between the application point and the hull plate (Figure 27 right).

By an additional analysis it is intended to compare the response of the structural members that complete main keelsons of the foundation, such as adjacent keelsons, intersecting transversal frames and other stiffened plating interested by the considered loads. The comparison is performed among the original structure and the proposed solutions analyzing the von Mises combined stress distribution (MPa) and the deformation patterns

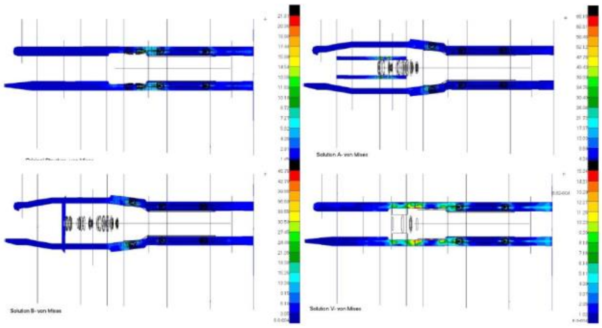

Figure 28 - Von Mises stress distribution (MPa) of the foundation's keelson flanges of the original structure (top left), Solution A (top right), Solution B (bottom left) and Solution V (bottom right)

Figure 28 confirms that only for the engine foundation flanges of the original structure and proposed Solution V, the longitudinal position of the maximum combined stresses are located on the flanges where the forces are applied. In the case of Solution A and Solution B, the maximum stresses are not found on the main keelsons flanges, but on the secondary structures used to support and resist the axial load coming from the thrust bearing.

9. VERIFICATION OF BOLTING-OPTION V

In this case study, after a deep structural analysis of the different proposed thrust bearings, the most suitable thrust bearing is the Solution V. The last structural verification concerns the connection between the supporting elements of the thrust block and the foundation. They are bolted with bolts class 8.8. In Figure 29, the FE mesh of the supporting elements of the thrust bearing is shown.

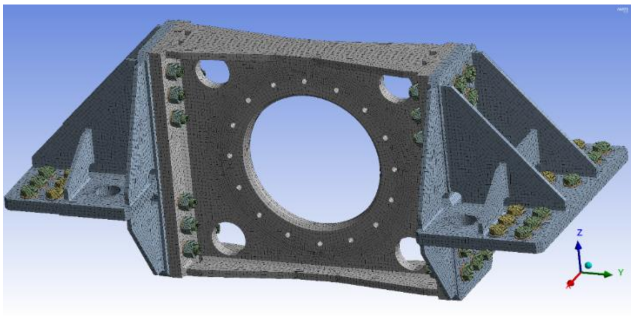

Figure 29 - The mesh of the supporting elements of the thrust bearing

In Figure 30 red arrow symbols show the bolt pretentioning, the thrust force and the boundary conditions applied to the numerical model.

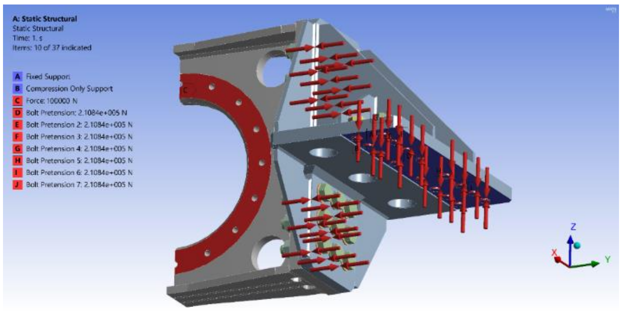

Figure 30 - The bolt pretentioning, the thrust force and the boundary condition

After static structural analysis has been run in Figure 31 and 32 respectively the longitudinal deformation and the Von Mises stress are reported. The longitudinal deformation is maximum in correspondence of the flange of the support but it is equal to only 0.015 mm.

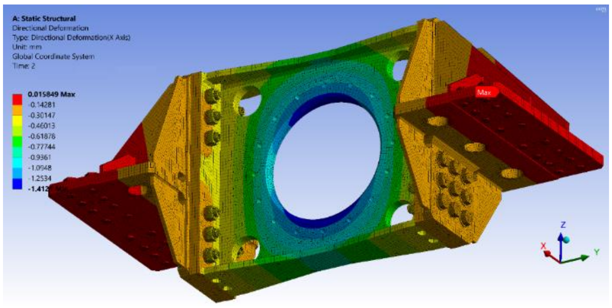

Figure 31 - Longitudinal deformation (X axes)

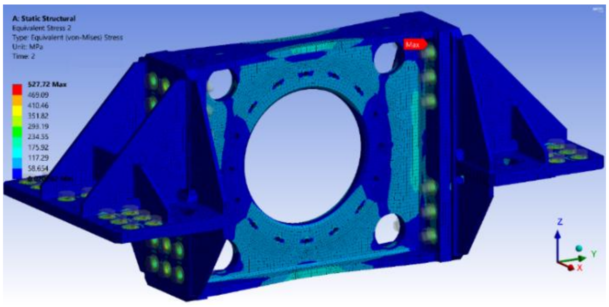

Figure 32 - Von Mises Stress

10. CONCLUSIONS

By the present investigation it came out that the strength of the engine foundations corresponding to the modified structures is reduced with respect to the strength of the original configuration. The less invasive modified Solution V, proposed to adapt the structure to the thrust block, presented the highest stresses on the foundation. This is due to the fact that it is the only block directly bolted to the main keelson flanges, whereas the other are connected to secondary elements. Nevertheless, the longitudinal stress values are small compared to the predefined critical stress limit σ_{cr}.

By a combined stress and strain analysis on the proposed Solution A and B, it was possible to find stress concentration points in the added or modified structures in order to support the thrust blocks.

These high stress values should not be neglected when designing the final shape of the secondary elements. However, this stress concentration is not transmitted to the main reinforcements of the bottom and the problem can be addressed as a localized issue keeping the general modified configuration .

The future development of this study, at the moment under course, will be to investigate the changes of the dynamic behavior of the structure after the insertion of the thrust bearings in the shaft line.

11. REFERENCES

1. AMERICAN BUREAU OF SHIPS (ABS), 2014. *Guide for Building and Classing of Motor Pleasure Yachts*, New York, USA.
2. BIOT, M, BOOTE, D, BROCCO, E, MORO, L, PAIS, T, DELLE PIANE, S., 2015. *Numerical and experimental analysis of the dynamic behavior of main engine foundations*, Proc 25th Int Offshore and Polar Eng Conf, Hawaii, ISOPE.
3. BOOTE, D, PAIS, T, DELLE PIANE, S. 2013. *Vibrations of superyacht structures: Comfort rules and predictive calculations*, Proc 4th International Conference on Marine Structures, Finland, MARSTRUCT.
4. BIOT, M., BOOTE, D., BROCCO, E., MORO, L., MENDOZA, VASSALLO, P.N., PAIS, T. *Validation of a Design Method for the Simulation of the Mechanical Mobility of Marine Diesel Engine Seatings*, Proceedings of Transport Means 2014 Conference, pp. 1-8, Kaunas University of Technology, Lithuania, 23rd – 24st October 2014.Bureau Veritas, 2012. *Rules for the Classification and Certification of Yachts*, Paris, France.
5. CHILDS, D, *Turbomachinery dynamics*, John Wiley, 1993.
6. DE SILVA, C. W., *Vibration: Fundamentals and Practice*, Taylor &Francis Group, Second Edition, 2007.
7. HARRIS, C.M., PIERSOL, A.G.,2002, *Harris' Shock and Vibration Handbook*, McGRAW-HILL, Fifth Edition.
8. MSC, Dynamic analysis User's Guide, MSC Software, 2013.
9. MSC Software Corporation, "Nastran UserGuide", Newport Beach, CA, USA, 2014.
10. LLOYD'S REGISTER OF SHIPPING, 2014. *Rules and Regulations for the Classification of Special Service Craft*, London, UK.
11. HUGHES O., 1988, Ship Structural Design, SNAME.
12. RIGO, P., and RIZZUTO, E. 2003. *Analysis and Design of Ship Structure*. In Ship Design and Construction, SNAME. Volumes 1 and 2. United States of America. Sheridan Books. Chapter 18, Pages (18-5 to 18-6).
13. PAIS, T, BOOTE, D, KAEDING, P. 2016. *Experimental and numerical analysis of absorber materials for steel decks*. Proc 26th Int Offshore and Polar Eng Conf., Rodi, ISOPE.
14. PAIS T., BOOTE D., VERGASSOLA G., 2018, *Vibration analysis for the comfort assessment of a superyacht under hydrodynamic loads due to mechanical propulsion*, Ocean Engineering, Vol. 155, pp 310-323.
15. PATNAIK SURYA N. and HOPKINS DALE A., *Strength of materials: A unified theory for the 21st Century*. Published by Elsevier January 2004 USA.
16. VULKAN COUPLING, *VULKARDAN E data sheet*. Published 09-2014, Herne, Germany. Available from www.vulkan.com
17. VENKATESH, B, SURA SANYASI, R., KAKARLA, S, JAYAVARAPU, M, 2015, *Design of marine propulsion shafting system for 53000 dwt bulk carrier*, International. Journal Mechanical. Engine. & Robotics Research, Vol. 4, No. 2.
18. VERGASSOLA G., BOOTE D., TONELLI A., 2018, *On the damping loss factor of viscoelastic materials for naval applications*, Ship and Offshore Structures, Vol. 13(5), pp 466-475.

RESISTANCE AND TRIM MODELING OF THE NAPLES HARD CHINE SYSTEMATIC SERIES

(DOI No: 10.3940/rina.ijsct.b1.2018.211)

D Radojčić and **M Kalajdžić**, University of Belgrade, Faculty of Mechanical Engineering, Department of Naval Architecture, Serbia

SUMMARY

An Artificial Neural Network (ANN) method with multiple-outputs is used to develop the mathematical models for the Naples Systematic Series (NSS) of resistance, dynamic trim, wetted surface area and length of wetted surface area, as functions of length beam ratio, slenderness ratio, longitudinal centre of gravity and volumetric Froude number. Multiple ANN output enables simultaneous use of all the available resistance and trim data, producing both an output for resistance and for trim. Similar results are obtained for the wetted surface area and length of wetted surface area datasets. Note that the multiple-output models share a common ANN structure, with only slight differences in equations for resistance and trim, and for wetted surface area and length of wetted surface area. *This paper is upgraded and corrected version of a paper published under the same title at the *11th High Speed Marine Vehicles Conference (HSMV 2017)* in Naples, 25th-26th October 2017.

NOMENCLATURE

B_{PX}	max. projected chine beam [m]
C_A	correlation allowance
C_F	frictional resistance coefficient
C_R	residuary resistance coefficient
C_T	total resistance coefficient
Fn_L	length Froude number
Fn_∇	volumetric Froude number $= \frac{v}{\sqrt{g\nabla^{1/3}}}$
g	acceleration due to gravity [m/s^2]
L	static waterline length [m]
L_{WL}	dynamic waterline length [m]
L_P	projected chine length [m]
L_P/B_{PX}	length-beam ratio of planing bottom area
$L_P/\nabla^{1/3}$	slenderness ratio
LCG	longitudinal center of gravity forward of the transom [m]
LCG/L_P	longitudinal center of gravity relative to transom
R	total bare hull resistance (towing tank cond.) = R_T [N]
R/Δ	resistance to weight ratio = $(R_T/\Delta)_{100000}$
S	wetted surface area [m^2]
$\frac{S}{\nabla^{2/3}}$	wetted surface area coefficient
v	velocity of craft [m/s]
Δ	displacement, mass [kg]
∇	volumetric displacement [m^3]
β	deadrise angle [deg.]
ν	kinematic viscosity of water [m^2/s]
ρ	mass density of water [kg/m^3]
τ	trim angle relative to its value at zero speed [deg.]
τ_S	trim at rest [deg.]
ANN	Artificial Neural Network
MM	Mathematical Model
NSS	Naples Systematic Series

Statistics

RMS	Root Mean Square $= \sqrt{\frac{1}{N}\sum_{i=1}^{N}\left(\frac{y_i-\hat{y}}{y_i}\right)^2}$
N	Number of cases
y_i	Measured value
$\hat{y}$	Evaluated value (with MM)
$\bar{y}$	Mean value of all measurements

Note: L_{WL}, L and B_{PX} correspond to L_{WLD}, L_{WL} and B_C, respectively in De Luca and Pensa (2017)

1. INTRODUCTION

Model test results in calm water for the Naples Systematic Series (NSS) have been presented in a recent paper by De Luca and Pensa (2017) for dynamic trim (τ), total and residuary resistance coefficients (C_T and C_R), wetted surface area (S) and waterline length (L_{WL}). NSS consists of five hard-chine, stepless models, all with the same deadrise distribution, wide-stern, warped bottom and rising keel. Tested speed range corresponds to length Froude numbers F_{nL} =0.5 - 1.6 or volumetric Froude numbers Fn_∇=1.1 - 4.2. NSS is envisaged to be used with interceptors, but the interceptor effect is yet to be published. Series primary parameters are length beam ratio (L_P/B_{PX}=3.45, 3.89, 4.45, 5.19 and 6.25), slenderness ratio ($L_P/\nabla^{1/3}$=5.0 - 7.8) and longitudinal centre of gravity (LCG/L_P=0.33 and 0.38)[1].

In the referenced work for each of the five NSS models and LCG/L_P=0.38 (correspond to static trim τ_S=0 deg.), regression analyses was used to derive a 20-term polynomial equation for evaluation of resistance (actually C_R), running wetted surface area and waterline length as a function of $L/\nabla^{1/3}$ and F_{nL}. That is, these are speed dependent, but L_P/B_{PX}, β and LCG independent mathematical models. Equations actually evaluate (interpolate) C_R, S and L_{WL} within the tested $L/\nabla^{1/3}$ range, but not between the two LCG positions and for the

---

[1] Note: notation used here is not same as in De Luca and Pensa (2017), see Nomenclature. Moreover, the main loading parameter (slenderness ratio) there and here is not same.

various L_P/B_{PX} values. This is similar to the simple two-parameter mathematical model (MM) of Radojčić et al. (2014a), except that each of five polynomial equations is valid for a particular NSS model, instead for the whole series. Dynamic trim, influence of interceptors and wave profile were not modeled, although they were tested.

Other mathematical models for hard chine hull forms for prediction of resistance and, where available, for dynamic trim are:

- Radojčić (1985) - Series 62 with β=12.5 and 25 deg. and Series 65-B
- Lahtiharju et al. (1991) - VTT hard chine models
- Keuning et al. (1993) - Series 62 with β=12.5, 25 and 30 deg.
- Radojčić et al. (2014a) - Series USCG and TUNS
- Radojčić et al. (2014b) - Series 50
- Radojčić et al. (2017) - Series 62 with β=12.5 to 30 deg.

The relationship of the NSS MM to the abovementioned MMs is depicted in Figure 1 and is presented in terms of the principal parameters $L_P/\nabla^{1/3}$ and $F_{n\nabla}$. For higher planing speeds, when the hydrodynamic forces are dominant, Savitsky's method (Savitsky, 1964) is the most frequently used resistance prediction model.

ANN is a nonlinear statistical data modeling technique that can be used to determine the complex relationships between dependent and independent variables. Probably the first application of ANN for modeling resistance of high speed vessels was in Bertram and Mesbahi (2004) and Mason et al. (2005). In the first case ANN was used for MM development, while in the second case ANN was implemented directly in the treatment of the test data for obtaining resistance, hence not for the MM development. By far the most frequent application of ANN is as in the second case, which considerable differs from that what is done here where ANN is actually used as an extraction tool for obtaining MM for resistance evaluation. Once MM is available it then can be used by the other users who do not have any knowledge about ANN whatsoever.

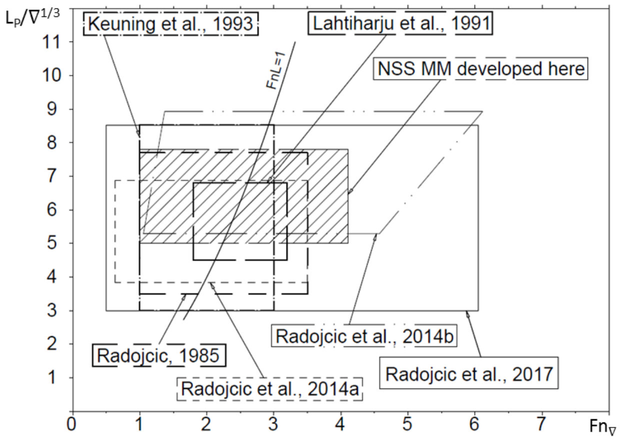

Figure 1: Relation of the MM developed here to other available planing hull MMs presented in terms of the principal parameters $L_P/\nabla^{1/3}$ and $F_{n\nabla}$

This paper fills in the gaps in the simplified two-parameter NSS MM explained above, and presents MMs of resistance (actually $(R_T/\Delta)_{100000}$), dynamic trim (τ), wetted surface area $(S/\nabla^{2/3})$ and length of wetted surface area (L_{WL}/L_P), as functions of L_P/B_{PX}, $L_P/\nabla^{1/3}$, LCG/L_P and $F_{n\nabla}$. An Artificial Neural Network (ANN) method with multiple-outputs is used to develop the enhanced mathematical models (see Radojčić et al. 2017, for example). Multiple ANN output enables simultaneous use of all the available $(R_T/\Delta)_{100000}$ and τ data, producing an output for R/Δ and another one for τ. A similar approach was used and, hence, similar results were obtained, for the $S/\nabla^{2/3}$ and L_{WL}/L_P datasets.

2. DEPENDENT AND INDEPENDENT VARIABLES

The raw model-scale data for each NSS model and various loadings were given in tabular form for Δ, L, $L/\nabla^{1/3}$, τ_S, v, τ, L_{WL}, S, C_R and C_T (see De Luca and Pensa, 2017). From the lines plans of each NSS model (created by 3D hydrostatic software according to the table of offsets for parent Model C1 and reduction factors for depth and beam which were given too), the exact value of LCG for each model and various loadings (Δ, L and τ_S) were obtained. These data were sufficient for configuration of parameters chosen here for the development of the mathematical models. These are:

- The single hull form parameter is L_P/B_{PX}. Note that the deadrise angle β, which in previous cases was amongst the hull-form parameters, is now identical for all models, hence may be regarded as a secondary hull form parameter.
- The hull loading parameters are LCG/L_P and $L_P/\nabla^{1/3}$.
- The performance parameters are volumetric Froude number ($Fn_\nabla = v/(g\cdot\nabla^{1/3})^{1/2}$), dynamic trim (τ) and total resistance-to-weight ratio for a 100,000 lb (45.36 t) boat – $(R_T/\Delta)_{100000}$ (from now just R/Δ). The running wetted length L_{WL}/L_P and wetted surface area coefficient $S/\nabla^{2/3}$ are necessary for Froude expansion in order to evaluate R/Δ for displacements other than 100,000 lb. Namely, $(R/\Delta)_{\text{New Displacement}} = (R_T/\Delta)_{100000} + f\,(S/\nabla^{2/3}, L_{WL}/L_P)$.

$(R_T/\Delta)_{100000}$ is obtained for standard operating conditions in sea water, i.e. 15°C, ρ=1026 kg/m^3 and ν=1.1907·10^{-6} m^2/s. Extrapolation is done with ITTC-1957 friction coefficients with zero roughness allowance (C_A=0)[2].

Thus, to summarize, the independent variables are Fn_∇, L_P/B_{PX}, $L_P/\nabla^{1/3}$ and LCG/L_P, while R/Δ, τ, L_{WL}/L_P and $S/\nabla^{2/3}$ are the dependent variables. Chosen variables are

---

[2] When R/Δ is calculated for displacement other than 100,000 lb, C_A may be applied if desired, as:

$$R/\Delta)_{\text{New Displacement}} = (R_T/\Delta)_{100000} +$$
$$+ [(C_F + C_A)_{\text{New Displacement}} - C_{F100000}]\cdot 1/2\cdot S/\nabla^{2/3}\cdot Fn_\nabla^2.$$

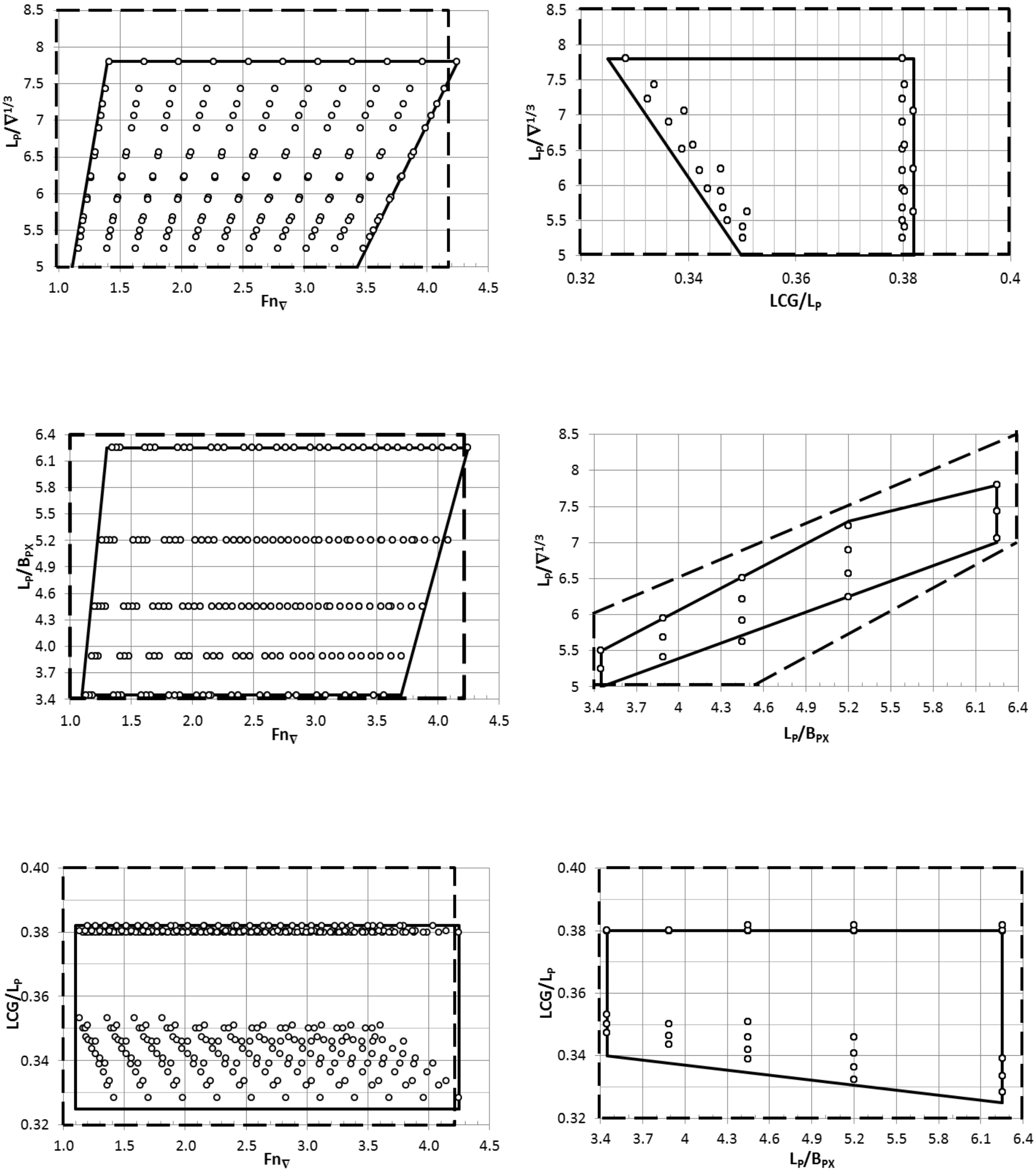

Figure 2: Boundaries of applicability (full lines). Dashed lines show extended boundaries which should be treated with caution

same as in other related papers, which facilitates easier hull comparison and hull form optimization.

The constraints of the original test variables (De Luca and Pensa, 2017) define the boundaries of applicability of the mathematical model, see Figure 2. The primary limits of the series are listed below:

$$3.45 \leq L_P/B_{PX} \leq 6.25$$
$$5 \leq L_P/\nabla^{1/3} \leq 7.8$$
$$0.33 \leq LCG/L_P \leq 0.38$$
$$1.1 \leq Fn_\nabla \leq 4.0$$

3. MATHEMATICAL MODELS FOR R/Δ, τ, S/∇$^{2/3}$ and L$_{WL}$/L$_P$

The ANN technique with multiple-outputs is used throughout in the same way as in Radojčić et al. (2017), i.e.:

- Program aNETka V2.0 (Zurek, 2007) was used
- A sigmoid function ($\text{sig} = (1 + e^{-x})^{-1}$, i.e. S-shaped curve) was adopted as an activation function
- The entire dataset was used for training of the algorithm.

Activation or transfer function convert an input signal of a node to an output signal, which then becomes input signal for another node in the next layer. Nonlinear activation function enables nonlinear transformation between input and output.

The use of the entire dataset produces repeatable results, but thorough checking of reliability and stability of the derived mathematical models is required. So, for each derived model, several 2D and 3D diagrams were plotted to demonstrate the model fit to data, and to ensure smooth behavior with no weaving between the data points. Note that repeatability also depends, but to a lesser extent, on the number of iterations used in the derivation (which was usually up to 100,000).

Selection of the number of layers and number of neurons within each layer is very important, because “over-fitting” can easily lead to instability. The number of layers and neurons is determined here in advance through a trial-and-error technique. That is, the development of an appropriate ANN structure is an iterative hands-on process. Consequently, several ANN models with different numbers of neurons per layer were developed. The development flow, together with the ANN structure of the finally adopted mathematical models, are given in Figure 3.

Multiple-output ANN structure allows τ data to influence modeling of R/Δ, and vice versa. Namely, R/Δ and τ often mirror each other, and a τ-hump generates an R/Δ-hump for the same Fn$_\nabla$ values. Note that 361 data points were available for each R/Δ and τ so that, in total, 722 points were used to simultaneously obtain the mathematical models for R/Δ and τ. Consequently, multiple-output models share a common ANN structure with only slight differences in the equations for R/Δ and τ.

Similar considerations apply for S/∇$^{2/3}$ and L$_{WL}$/L$_P$ datasets. Moreover, ANN structures for both datasets, R/Δ & τ, and L$_{WL}$/L$_P$ & S/∇$^{2/3}$, are identical, thereby further simplifying the programming. The models that were finally selected are stable and accurate, although statistically they are not the best fits amongst all of the considered models, see RMS values in the tables of Figure 3.

Multiple R/Δ and τ

No. Hidden layers	No. of terms	No. of considered MM	Correlation	RMS
1	48-78	3	0.983-0.990	4-7.3
2	109-131	18	0.994-0.997	3.7-4.8
3	84-113	2	0.996-0.997	4.1-4.6
4	124	1	0.997	3.7
2	**131**	**Final MM**	**0.997**	**3.9**

Multiple L$_{WL}$/L$_P$ and S/∇$^{2/3}$

No. Hidden layers	No. of terms	No. of considered MM	Correlation	RMS
1	48-78	1	0.983	7.3
2	109-131	7	0.992-0.993	5-6.3
3	84-113	2	0.988-0.992	6.4-10
2	**131**	**Final MM**	**0.993**	**5.04**

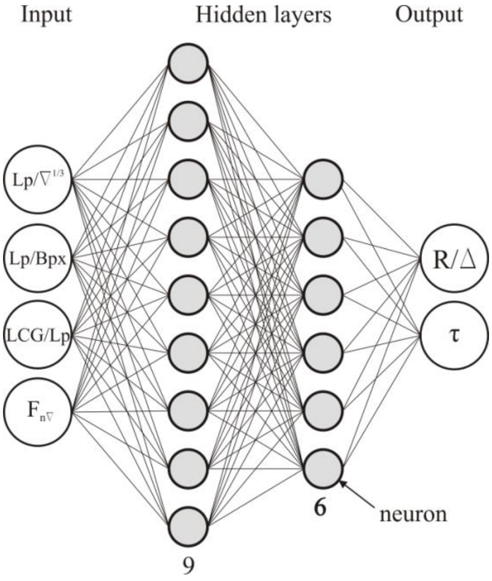

Figure 3: Developing process (tables) and multiple-output ANN structure for R/Δ & τ. ANN structure for L$_{WL}$/L$_P$ & S/∇$^{2/3}$ is identical to R/Δ & τ ANN structure

Table 1: Final form of multiple-output mathematical models for both, R/Δ & τ and L_{WL}/L_P & $S/\nabla^{2/3}$

R/Δ & τ and **L_{WL}/L_P & $S/\nabla^{2/3}$**	$Y_{1,2}=\dfrac{sig\left(c_w+\sum_{i=1}^{6}\left(C_{iw}\times sig\left(b_i+\sum_{j=1}^{9}\left(B_{ji}\times sig\left(a_j+\sum_{k=1}^{4}\left(A_{kj}\times\left(P_kX_k+R_k\right)\right)\right)\right)\right)\right)\right)-G_{1,2}}{L_{1,2}}$ Where $Y_1=R/\Delta$, $Y_2=\tau$ or $Y_1=L_{WL}/L_P$, $Y_2=S/\nabla^{2/3}$ $X_k=\left\{L_P/\nabla^{1/3}, L_P/B_{PX}, LCG/L_P, F_{n\nabla}\right\}$, $sig(x)=\dfrac{1}{1+e^{-x}}$ ***Coefficients for R/Δ & τ and L_{WL}/L_P & $S/\nabla^{2/3}$ are given in the Appendices 1and 2***

As shown in Figure 3, Table 1 and Appendices 1 and 2, the multiple-output configuration in both cases is 4-9-6-2 with 131 terms that define both R/Δ & τ, as well as L_{WL}/L_P & $S/\nabla^{2/3}$, with only 9 terms differing between R/Δ & τ, and L_{WL}/L_P & $S/\nabla^{2/3}$. That is, even though R/Δ & τ on one side, and L_{WL}/L_P & $S/\nabla^{2/3}$ on the other, are physically different quantities, 113 terms of the mathematical model describing the multidimensional surfaces are identical.

4. VERIFICATION OF DERIVED R/Δ, τ, $S/\nabla^{2/3}$ AND L_{WL}/L_P EQUATIONS

In general, model verification usually consists of presenting:

a) statistics of model accuracy,
b) documentation of the discrepancies between the modeled and measured values, and
c) exploration of the model behaviour between the fitted data points.

In this specific case the statistics are not presented, since this would be meaningful mostly for comparison of different mathematical models based on a common dataset (as in Radojčić et al. 2014b, for example), which is not the case here. On the other hand, in order to ensure the expected and logical behaviour, the linear R/Δ, τ, L_{WL}/L_P and $S/\nabla^{2/3}$ trend between LCG/Lp=0.34 and 0.38 was assumed and needs to be verified. Consequently, the verification procedure used here consists of demonstrating b) and c) above. The newly-derived mathematical models were also compared with experimental data for arbitrary hull forms similar to the NSS. Figures 4 to 11 show only the verification results for R/Δ and τ, although identical 2D and 3D graphs were produced also for L_{WL}/L_P & $S/\nabla^{2/3}$.

4.1 COMPARISON OF EVALUATED AND MEASURED VALUES

The goal is to develop mathematical models that accurately fit experimental data, but not “over-fit” to an extent where experimental scatter becomes part of the model. Figure 4 shows maximal discrepancies, but from the obvious outliers, i.e. MM for τ faired experimental data. Most discrepancies between the evaluated and experimental τ data are, by far, within 0.1 deg., with a few points within 0.2 deg., and an occasional point lying beyond 0.2 deg., corresponding to the outliers as indicated in Figure 4. It should be noted that it is considerably easier to find an adequate MM for R/Δ than for τ (as also concluded in Radojčić et al., 2017) and that R/Δ discrepancies compered to experimental data are almost negligible.

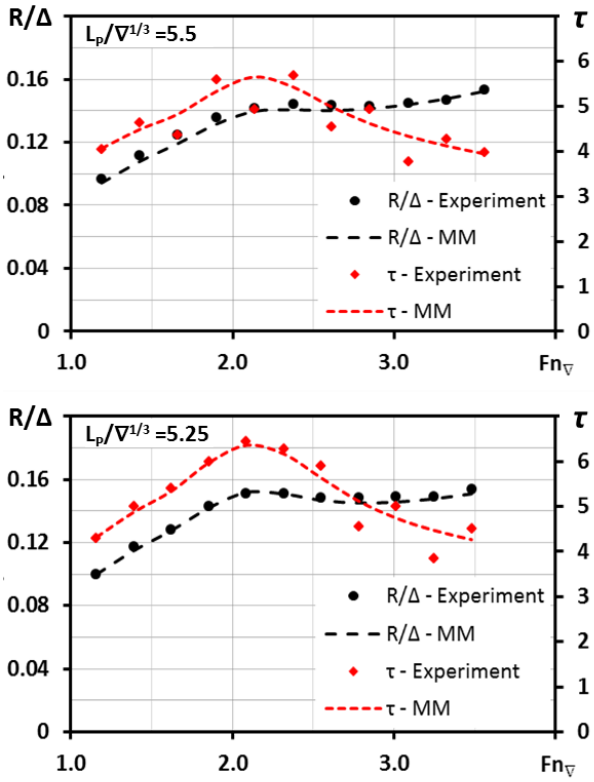

Figure 4: 2D R/Δ and τ graphs ($L_P/\nabla^{1/3}$=5.5 and 5.25, LCG/L_P=0.35, L_P/B_{PX}=3.45)

Typical discrepancies of R/Δ and τ between the modeled and measured points are illustrated in Figures

5 to 7. These discrepancies are within the measurement errors; see the uncertainty for experimental results given in De Luca and Pensa (2017). Note also that the accuracy of the dynamic trim measurements is generally around ± 0.20 – 0.25 deg. (see Blount, 2014).

Figures 5 to 7 also show the 3D surfaces generated by the mathematical model, with the curves representing the original test data superimposed on the surfaces to show the discrepancies between measured and calculated values. 2D diagrams (for the same loadings), better illustrate the difference between the measurements and MM. Altogether, very good agreement between the measurements and mathematical models is shown for all cases discussed above, as well as for the many others that were examined.

4.2 FIT OF MODELS BETWEEN DATA POINTS

Excessively elastic multidimensional mathematical models can easily fit the measured data, but may also be too elastic between the data points. Therefore, several 3D graphs were examined to ensure that there is no waving of the R/Δ, τ, $S/\nabla^{2/3}$ and L_{WL}/L_P surfaces between the measured points. Figures 8 to10 show example plots demonstrating the stability of the mathematical models over the whole range of independent variables. Note that the multidimensional surfaces seem to be stable even beyond the tested boundaries. Extended (extrapolated) zones, also indicated in Figure 2, should, however, be taken with caution.

4.3 VERIFICATION OF DERIVED R/Δ AND τ EQUATIONS

The derived MMs are compared with the experimental data of the USCG Motor Lifeboat Series (Kowalyshyn and Metcalf, 2006) as those are also wide-transom warped-bottom hulls. The closest USCG model to the NSS is Model No 5629 (β_M=23°, L_P/B_{PX}=4.09, $L_P/\nabla^{1/3}$ =5.6, LCG/L_P=0.37). Figure 11 shows the differences between the modeled and tested R/Δ and τ data for the USCG Model No. 5629. For other cases examined the agreement between the measured and modeled data is equally good.

5. CONCLUSIONS

The principal results of this work are mathematical models for resistance and dynamic trim of the NSS hard-chine planing hulls, covering the speed range Fn_∇=1 to 4.2. MMs for evaluation of $S/\nabla^{2/3}$ and L_{WL}/L_P are also developed as they are needed for Froude expansion. All derived MMs can be easily adapted for computer modeling used in everyday engineering work. As a side effect, modeling also enabled fairing of raw experimental data.

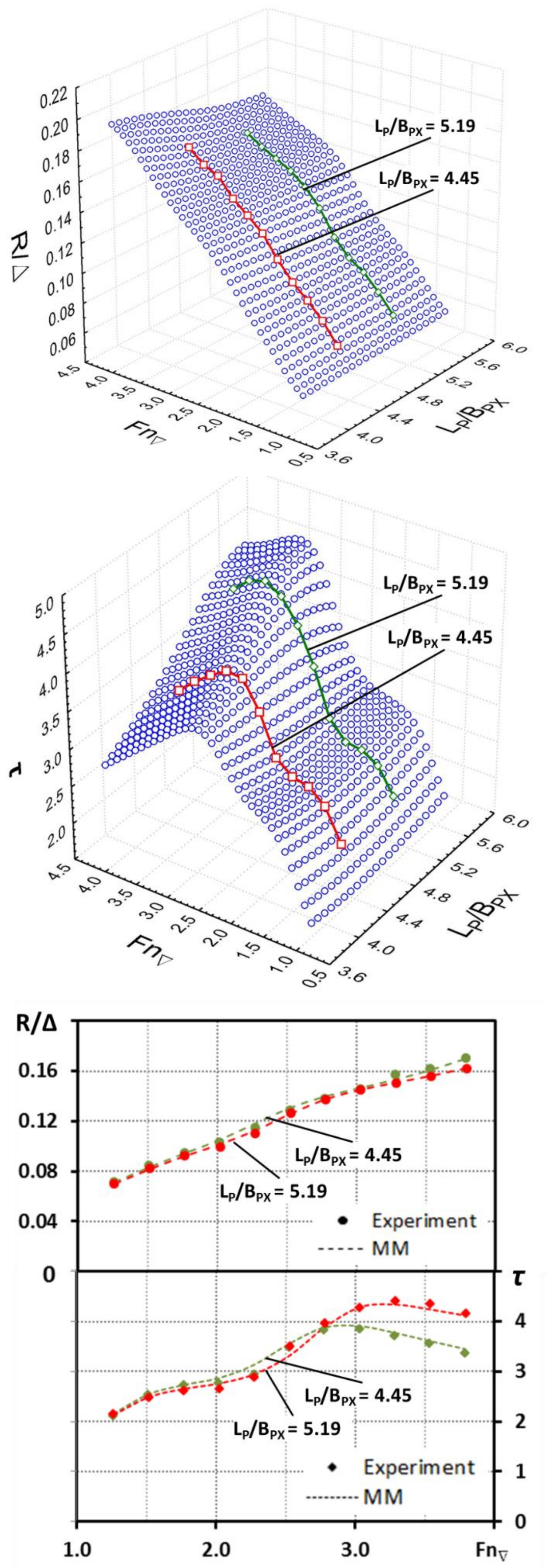

Figure 5: 3D and 2D R/Δ and τ graphs for L_P/B_{PX}=4.45 and 5.19 for $L_P/\nabla^{1/3}$=6.22 and LCG/Lp=0.38

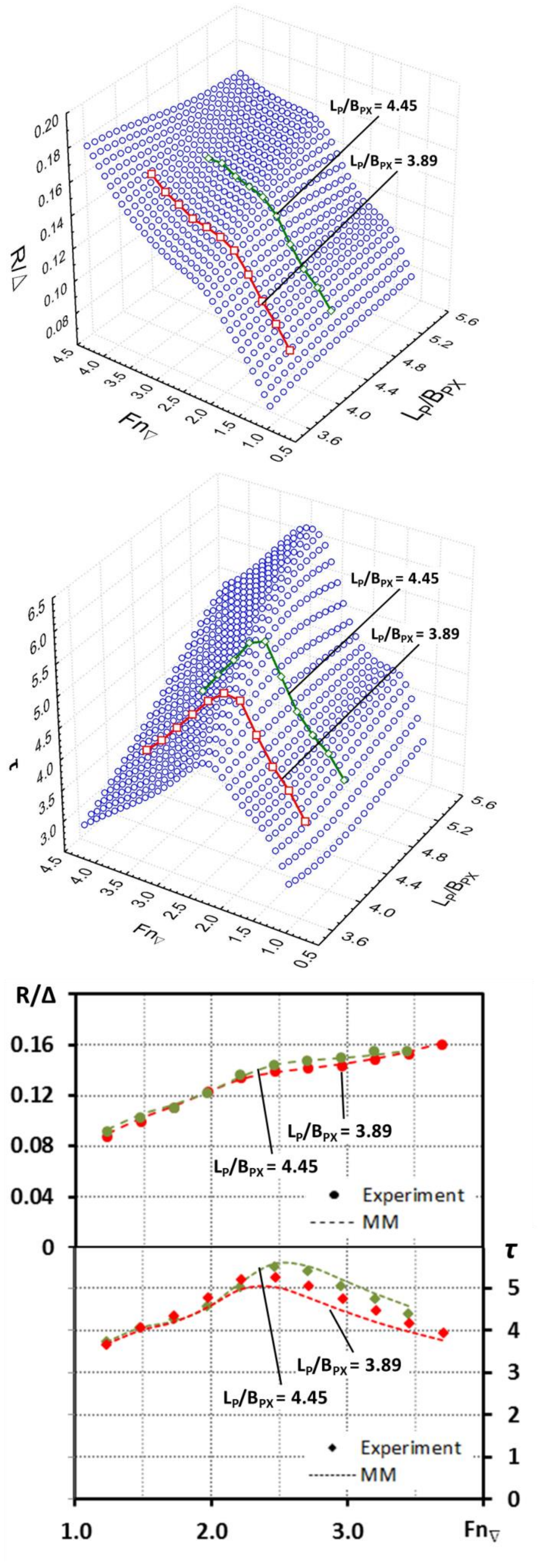

Figure 6: 3D and 2D R/Δ and τ graphs for L_P/B_{PX}=3.89 and 4.45 for $L_P/\nabla^{1/3}$=5.92 and LCG/L_P=0.35

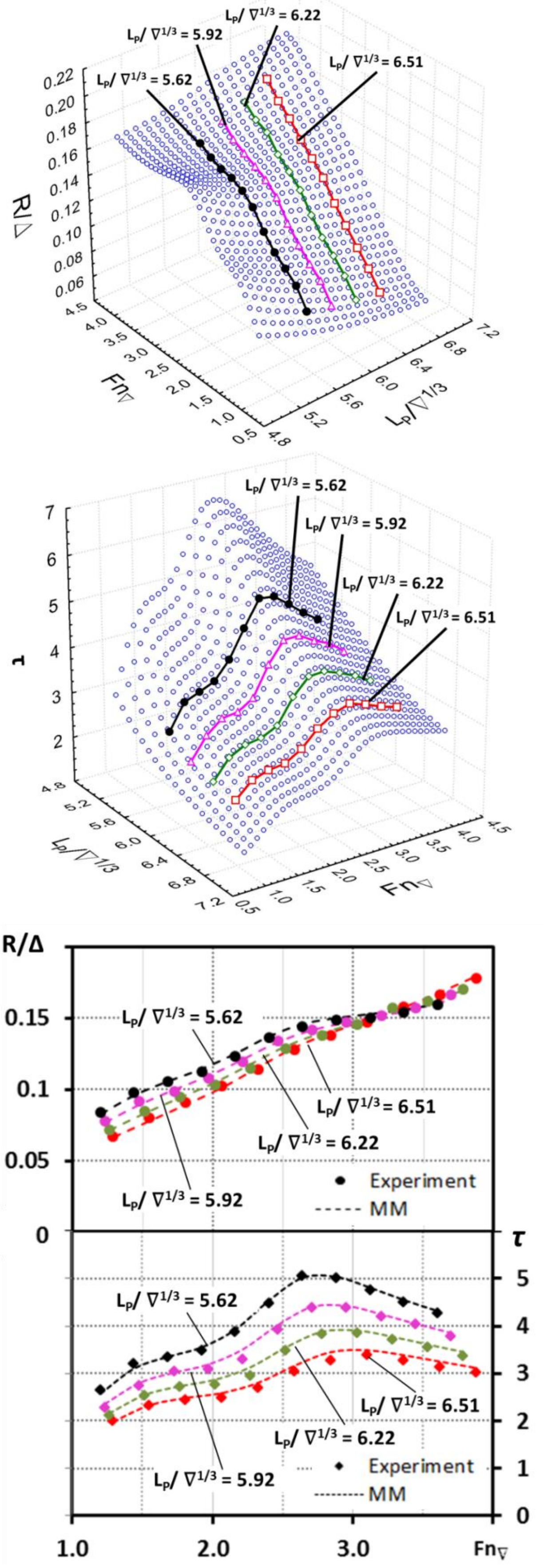

Figure 7: 3D and 2D R/Δ and τ graphs for $L_P/\nabla^{1/3}$=5.62, 5.92, 6.22 and 6.51 for L_P/B_{PX}=4.45 and LCG/L_P=0.38

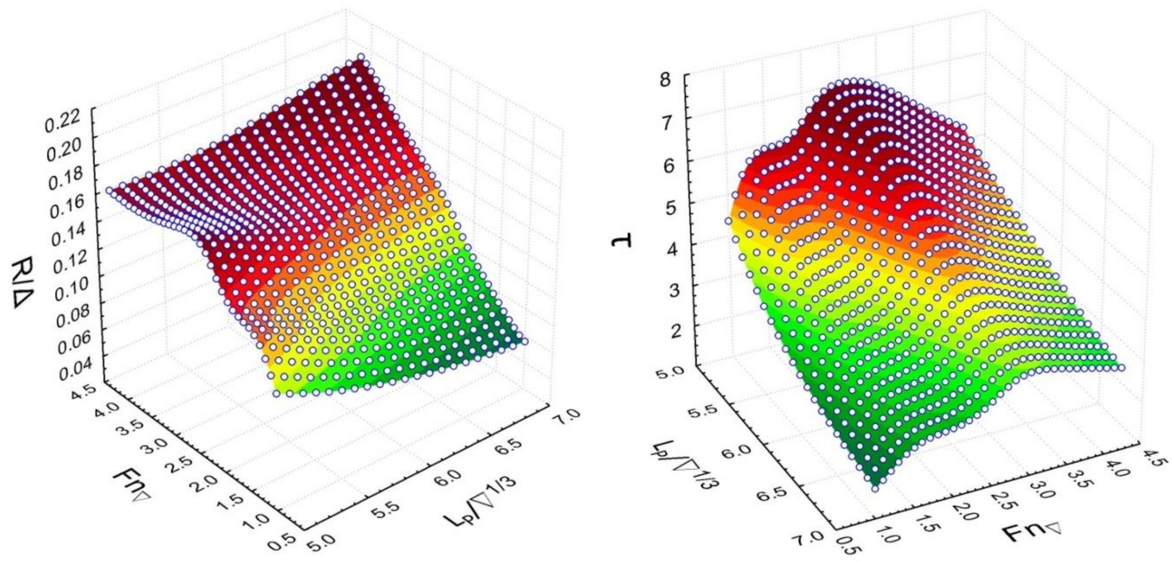

Figure 8: The influence of $L_P/\nabla^{1/3}$ on R/Δ and τ (L_P/B_{PX}=4.71, LCG/L_P=0.36)

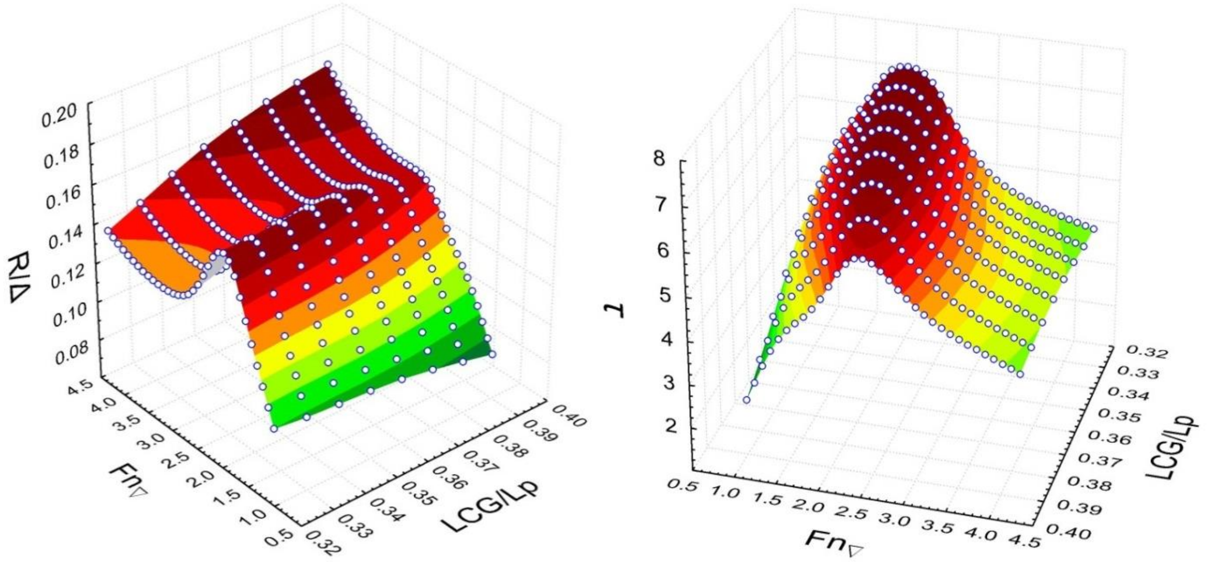

Figure 9: The influence of LCG/L_P on R/Δ and τ (L_P/B_{PX}=3.44, $L_P/\nabla^{1/3}$=5)

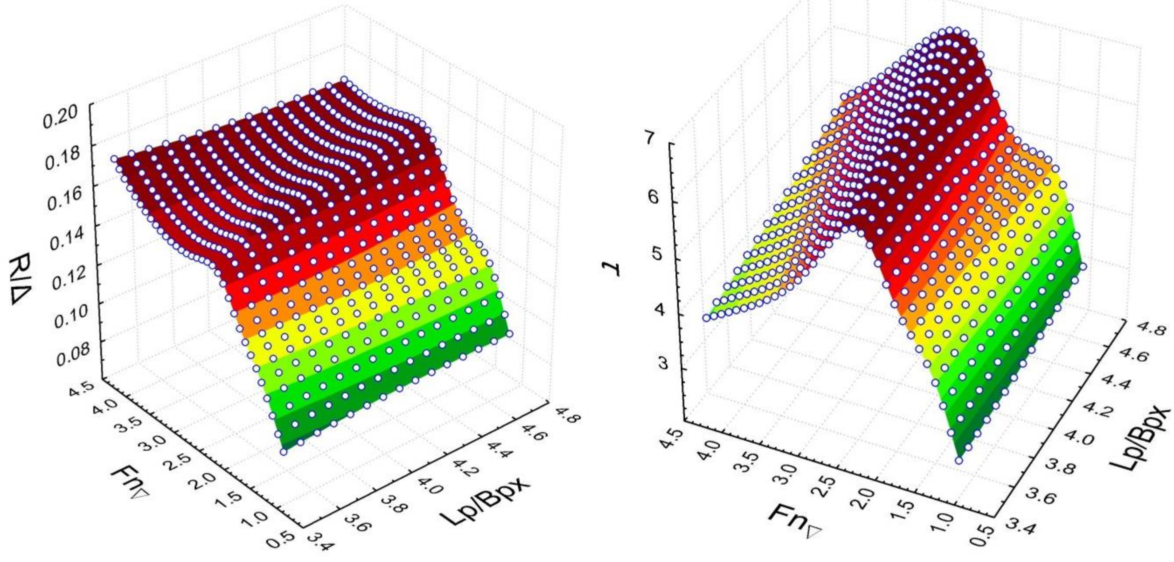

Figure 10: The influence of L_P/B_{PX} on R/Δ and τ ($L_P/\nabla^{1/3}$=5, LCG/L_P=0.37)

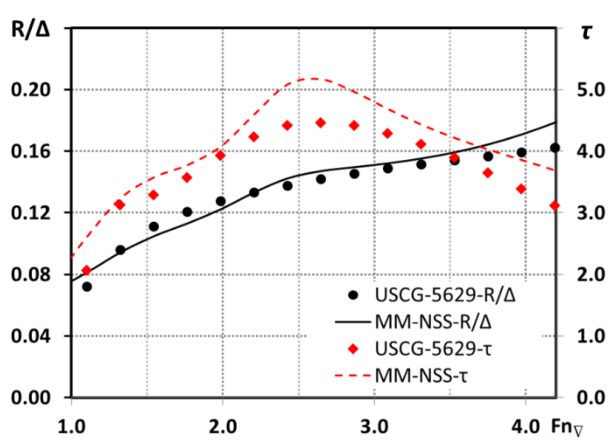

Figure 11: Comparison of MM predictions with the measurements of USCG Model No. 5629 ($\beta_M=23^o$, $L_P/B_{PX}=4.09$, $L_P/\nabla^{1/3}=5.6$, $LCG/L_P=0.37$)

The input parameters for all the derived mathematical models that define the hull form and loading, are L_P/B_{PX}, $L_P/\nabla^{1/3}$ and LCG/L_P. The secondary hull characteristics of the NSS (deadrise angle distribution, for instance) are an intrinsic part of the models, and hence the MMs are applicable for this and similar hull forms within the boundaries of applicability. Slight extrapolation, within the boundaries indicated in Figure 2, might be considered with caution.

Multiple-output models share the same ANN structure, with only slight differences in equations for R/Δ and τ. Namely, equations with 122 terms define each R/Δ and τ, but 113 terms are common to both, clearly demonstrating the relationship between dynamic trim and resistance on planing craft. As the multiple-output ANN structure is identical for R/Δ & τ, and L_{WL}/L_P & $S/\nabla^{2/3}$, the abovementioned discussion stands for both datasets.

MMs developed here are valid for the NSS without interceptors and for conditions as per De Luca and Pensa (2017). MMs were developed immediately following the publication of the experimental results, and hence this work may be considered as an extension of that paper. Once the influence of the interceptors is revealed, new MMs can be developed to demonstrate the interceptor effect (the depth of interceptor, for instance, may be the fifth independent variable).

6. ACKNOWLEDGMENTS

The paper is part of the project “Development of the Next Generation of Safe, Efficient, Ecological (SE-ECO) Ships” executed by the Department of Naval Architecture, Faculty of Mechanical Engineering, University of Belgrade. The project is partly financed by the Serbian Ministry of Education, Science and Technology Development, Contract No. TR35009.

7. REFERENCES

1. BERTRAM, V. and MESBAHI, E. (2004) *Estimating Resistance and Power of Fast Monohulls Employing Artificial Neural Nets.* Int. Conf. High Performance Marine Vehicles (HIPER), Rome.
2. BLOUNT, D. L. (2014) *Performance by Design.* ISBN 0-978-9890837-1-3
3. DE LUCA, F. and PENSA, C. (2017) *The Naples warped hard chine hulls systematic series.* Ocean Engineering, 139.
4. KEUNING, J. A., GERRITSMA, J. and TERWISGA, P. F. (1993) *Resistance Tests of a Series Planing Hull Forma With 30^o Deadrise Angle, and a Calculation Model Based on This and Similar Systematic Series.* International Shipbuilding Progress, Vol. 40, No. 424.
5. KOWALYSHYN, D. H. and METCALF, B. (2006) *A USCG Systematic Series of High Speed Planing Hulls.* Trans. SNAME, Vol. 114.
6. LAHTIHARJU, E., KARPPINEN, T., HELLAVAARA, M. and AITTA, T. (1991) *Resistance and Seakeeping Characteristics of Fast Transom Stern Hulls with Systematically Varied Form.* Trans. SNAME, Vol. 99.
7. MASON A., COUSER, P., MASON, G., SMITH, C. R. and KONSKY, B. R. von (2005) *Optimisation of Vessel Resistance using Genetic Algorithms and Artificial Neural Networks.* 4th Int. Conf. on Computer and IT Applications in the Maritime Industries, Hamburg.
8. RADOJČIĆ, D. (1985) *An Approximate Method for Calculation of Resistance and Trim of the Planing Hulls.* SNAME Symp. on Powerboats, Sept. 1985; also University of Southampton, Ship Science Report No. 23.
9. RADOJČIĆ, D., ZGRADIĆ, A., KALADŽIĆ, M. and SIMIĆ, A. (2014a) *Resistance Prediction for Hard Chine Hulls in the Pre-Planing Regime.* Polish Maritime Research, Vol. 21, No. 2(82), Gdansk.
10. RADOJČIĆ, D., MORABITO, M., SIMIĆ, A. and ZGRADIĆ, A. (2014b) *Modeling With Regression Analysis and Artificial Neural Networks the Resistance and Trim of Series 50 Experiments with V-Bottom Motor Boats.* Journal of Ship Production and Design, Vol.30, No.4.
11. RADOJČIĆ, D. V., KALAJDŽIĆ, M. D., ZGRADIĆ, A. B. and SIMIĆ, A. P. (2017) *Resistance and Trim Modeling of Systematic Planing Hull Series 62 (With 12.5, 25 and 30 Degrees Deadrise Angles) using Artificial Neural Networks, Part 2: Mathematical Models.* Journal of Ship Production and Design, Vol.33, No.4.
12. SAVITSKY, D. (1964) *Hydrodynamic Design of Planing Hulls.* Marine Technology, Vol. 1, No. 1.

13. ZUREK, S. (2007) *LabVIEW as a tool for measurements, batch data manipulations and artificial neural network predictions.* National Instruments, Curriculum Paper Contest, Przeglad Elektrotechniczny, Nr 4/2007.

APPENDIX 1 – MULTIPLE OUTPUT – R/Δ AND τ

ANN coefficients L_w, G_w, R_k, P_k, A_{kj}, B_{ji}, C_{iw}, a_j, b_i and c_w for resistance (R/Δ) and dynamic trim – **τ**

$$Y_w = \frac{sig\left(c_w + \sum_{i=1}^{6}\left(C_{iw} \times sig\left(b_i + \sum_{j=1}^{9}\left(B_{ji} \times sig\left(a_j + \sum_{k=1}^{4}\left(A_{kj} \times \left(P_k X_k + R_k\right)\right)\right)\right)\right)\right)\right) - G_w}{L_w}$$

Where $w = \{1,2\}$, $Y_1 = R/\Delta$, $Y_2 = \tau$, $X_k = \{L_P/\nabla^{1/3}, L_P/B_{PX}, LCG/L_P, F_{n\nabla}\}$, $sig(x) = \frac{1}{1+e^{-x}}$

j	A_{1j}	A_{2j}	A_{3j}	A_{4j}	a_j
1	1.6841110	3.0981180	1.5282840	-16.4245400	3.1890700
2	2.4092060	0.3142931	0.3908146	0.2556609	-1.8597140
3	-1.9152880	-7.1345370	-3.6484370	-0.6078711	1.1340150
4	-1.4699330	-10.6498300	-0.0225162	-0.5634111	10.0365500
5	4.1680880	-4.5602380	0.6937186	2.7010170	-2.0246550
6	1.3626750	0.1168425	0.7784404	-10.0020100	-0.6886486
7	0.5479282	2.5084270	-1.1066880	-3.2642590	-0.3612035
8	-0.9420888	-0.2510580	0.0049670	-7.9977910	2.1865540
9	-3.1893870	1.2750320	-0.5223626	-3.9322540	4.7179180

	$L_P/\nabla^{1/3}$	L_P/B_{PX}	LCG/L	Fn_∇
P_k	0.3214286	0.3215434	16.6666698	0.2893891
R_k	-1.5571429	-1.0596463	-5.4166677	-0.2770096

	R/Δ	τ
L_w	6.4766839	0.1573427
G_w	-0.2948834	-0.1309441

i	B_{1i}	B_{2i}	B_{3i}	B_{4i}	B_{5i}	B_{6i}	B_{7i}	B_{8i}	B_{9i}	b_i
1	-0.4082681	0.0891881	1.4520660	0.0838715	1.1443510	-4.0656230	1.7600280	3.3407880	2.1149690	-2.0033580
2	0.6056641	1.8613140	0.3999820	0.1692302	0.0305501	2.5074690	-0.4054057	-0.8660036	1.2468480	-3.5325410
3	-0.1796350	-2.7916050	-2.9371210	0.3929720	-1.9068460	-6.4689190	-0.7239615	-2.9223100	-2.3012630	3.3583560
4	-5.3774030	-4.4911580	-2.2997850	-1.4914010	-3.7586970	-7.1752740	0.5064505	8.1555560	5.5388670	-4.1627820
5	-0.2961807	-4.7618480	-2.7215400	-0.5896583	2.0540800	0.1658212	-1.8644930	-1.6496020	-8.5582700	2.9999680
6	-6.2256920	2.9541990	-2.5990310	0.7695088	-3.3201360	-4.2225760	-1.7524090	7.9941520	-3.7219060	-0.1329643

w	C_{1w}	C_{2w}	C_{3w}	C_{4w}	C_{5w}	C_{6w}	c_w	
1	-2.2633980	-7.7446910	0.2705126	4.3702590	7.6477400	0.0098969	3.2038660	← for R/Δ
2	7.3747910	-1.3781800	4.4610630	8.6496370	-1.1401120	6.7151070	-6.6791630	← for **τ**

APPENDIX 2 – MULTIPLE OUTPUT – L_{WL}/L_P AND $S/\nabla^{2/3}$

ANN coefficients L_w, G_w, R_k, P_k, A_{kj}, B_{ji}, C_{iw}, a_j, b_i and c_w for length of wetted area (L_{WL}/L_P) and wetted area ($S/\nabla^{2/3}$)

$$Y_w = \frac{sig\left(c_w + \sum_{i=1}^{6}\left(C_{iw} \times sig\left(b_i + \sum_{j=1}^{9}\left(B_{ji} \times sig\left(a_j + \sum_{k=1}^{4}\left(A_{kj} \times \left(P_k X_k + R_k\right)\right)\right)\right)\right)\right)\right) - G_w}{L_w}$$

Where $w = \{1,2\}$, $Y_1 = L_{WL}/L_P$, $Y_2 = S/\nabla^{2/3}$, $X_k = \{L_P/\nabla^{1/3}, L_P/B_{PX}, LCG/L_P, F_{n\nabla}\}$, $sig(x) = \frac{1}{1+e^{-x}}$

j	A_{1j}	A_{2j}	A_{3j}	A_{4j}	a_j
1	-1.0290940	-8.3437940	-0.7758193	0.3231824	1.9491680
2	4.2965780	-6.9091490	-1.0277140	8.8388290	-1.9010410
3	5.1826030	-1.5968630	5.0166010	1.0523230	-6.5190030
4	-15.3890100	9.5143390	0.6286043	4.9452410	-2.6309080
5	10.4899200	-4.8726330	-1.6352600	-0.1959135	-4.5200380
6	-0.9499520	-2.1286730	-0.9494023	8.1789890	-0.9933102
7	-26.5298400	0.8592815	-1.6622860	0.6121404	9.7718200
8	1.6415560	-8.1853450	-0.8103762	1.7085260	0.0527342
9	-12.0271000	-2.0909870	-0.9701849	0.9512810	1.7652420

	$L_P/\nabla^{1/3}$	L_P/B_{PX}	LCG/L	Fn_∇
P_k	0.3214286	0.3215434	16.6666698	0.2893891
R_k	-1.5571429	-1.0596463	-5.4166677	-0.2770096

	L_{WL}/L_P	$S/\nabla^{2/3}$
L_w	2.0529197	0.1524332
G_w	-1.0735219	-0.3873496

i	B_{1i}	B_{2i}	B_{3i}	B_{4i}	B_{5i}	B_{6i}	B_{7i}	B_{8i}	B_{9i}	b_i
1	4.1591200	-0.9906697	13.9657000	-2.6740540	6.1056830	-4.2079160	-2.5134440	2.3902560	2.6879430	7.9379350
2	1.0908680	-1.9158720	0.3214091	2.3244010	-3.6995700	-1.0235730	-4.3936600	1.6758450	-6.1349780	4.2691960
3	5.9825890	-1.3113770	0.1117310	-0.0907498	-2.4306030	0.6541541	1.3742260	-3.7154990	-2.3982970	-0.7658195
4	-12.5662400	1.0044840	10.1118400	0.2574254	14.9457800	-0.5477254	7.7494610	-9.2629270	12.7814500	3.2341290
5	2.4613880	1.2783540	0.3146927	-3.3574090	1.8264710	-1.5419090	-10.0103900	-1.0326580	0.1740037	-2.0128590
6	-3.9455390	0.4092577	0.7670850	0.1192115	-0.9617954	-2.9109090	-0.9420338	4.2584630	0.7633737	2.8597680

w	C_{1w}	C_{2w}	C_{3w}	C_{4w}	C_{5w}	C_{6w}	c_w
1	5.2640740	-1.3256100	1.4416850	6.9203660	0.8226122	5.7311380	-15.1649800
2	3.5917060	2.1159010	4.8052780	-0.4571030	12.4226700	1.2936160	-8.0888610

← for L_{WL}/L_P

← for $S/\nabla^{2/3}$

LCG EFFECTS ON RESISTANCE, LIFT AND TRIM CHARACTERISTICS OF R/V ATHENA HULL

(DOI No: 10.3940/rina.ijsct.2018.b1.212)

S Duman, **B Sener**, Yildiz Technical University, Turkey and **S Bal**, Istanbul Technical University, Turkey

SUMMARY

The proper prediction of resistance and lift values of high-speed planning crafts is of importance in hydrodynamic design. Modelling of free water surface has also a great importance on the simulation of flow around a planing hull running at high speeds. Another issue that must be taken into account is the vertical plane motions, i.e., trim and sinkage values. Dynamic trim and hence the planing performance of the hull are directly related to LCG (Longitudinal Center of Gravity). In this study, hydrodynamic analyses (including LCG effects) of R/V Athena hull which has a round-bilge and transom stern planing craft have been performed with overset and rigid grid techniques and the numerical results have been compared with the available experimental data. It has been found that the overset grid technique is more stable than the rigid grid technique in the transition region to the planing regime in terms of dynamic trim and sinkage. The hydrodynamic computations of R/V Athena hull are then repeated for different LCG values using only overset grid technique in a wide range of Froude numbers. For CFD (Computational Fluid Dynamics) analyses, a commercial unsteady RANS (Reynolds-averaged Navier Stokes) solver based on finite volume method (FVM) has been used. The free surface effects have been included in the computations by volume of fluid (VOF) method. The effects of LCG on resistance coefficients, dynamic trim and sinkage values, hydrodynamic lifting forces and wetted surface areas are discussed.

NOMENCLATURE

B	Beam (m)
C_T	Total resistance coefficient
C_R	Residual resistance coefficient
C_F	Frictional resistance coefficient
C_P	Dynamic pressure coefficient
C_L	Dynamic lifting force coefficient
DOF	Degree-of-freedom
DTMB	David Taylor Model Basin
E	Difference between two solutions
Fn	Froude number
FS	Factors of safety
g	Gravitational acceleration (m s^{-2})
GCI	Grid Convergence Index
L	Length between perpendiculars (m)
LCG	Longitudinal center of gravity (m)
ITTC	International Towing Tank Conference
N	Total cell numbers
ONR	Office of Naval Research
P_A	Actual pressure (N m^{-2})
P_∞	Reference pressure (N m^{-2})
RANS	Reynolds-averaged Navier-Stokes
r	Refinement factor
R	Convergence ratio
R_T	Total resistance (N)
$\mathrm{RT}_{\mathrm{EXT}}$	Extrapolated total resistance (N)
S	Wetted surface area (m^2)
SF	Safety factor
T	Draught (m)
U	Uncertainty; total resistance (N)
V	Ship advance speed (m s^{-1})
$y+$	Dimensionless wall distance
δ	Error estimator
λ	Model scale ratio
υ	Kinematic viscosity (N s m^{-2})
ρ	Density of water (kg m^{-3})
Δt	Time step
ε	Relative error
$\overline{u}_i$	Average velocity components (m s-^{1})
$\overline{\tau}_{ij}$	Viscous stress tensor

1. INTRODUCTION

There is a wide application area for high-speed marine vehicles ranging from small pleasure boats to large military vessel. Prediction of the hydrodynamic performance of these crafts is one of the most challenging problems in naval architecture due to its complex nature. At high speeds, the hydrodynamic lifting forces acting on the hull become dominant and part of the total displacement is lifted by these forces. When the hull enters the planing regime it raises above the free water surface and the wetted surface area decreases. At that moment it is crucial to determine the dynamic behaviour of the vessel in terms of lifting forces, dynamic trim and sinkage values, wetted surface areas etc. Numerous studies have been done by the researchers for the assessment of hydrodynamic characteristics of high-speed marine vehicles, e.g., empirical, experimental and/or computational.

(Savitsky, 1964) was one of the most famous researchers who succeeded to formulate and generalize the trim and the total resistance of the planing hull. After the systematic model experiments carried out by (Fridsma, 1969), experimental studies on planing hulls behaviour have begun. His first report included the results of a series of constant-deadrise models with different lengths, tested both in calm water and regular waves. He provided a mathematical approach on the effects of some design parameters, such as deadrise, trim, length-beam ratio, load etc. on the resistance performance, heave and pitch motions and impact accelerations, and indicated trends between seakeeping and systematically varied geometric and operational parameters.

In the first phase of the Fridsma's work (1971), the results were applicable only at low speeds and small wave heights. Therefore, he continued his studies in more realistic environmental conditions by performing the tests of same models in irregular waves (Fridsma, 1971). As a result of the work, a design procedure was developed that predicts the performance of any given hull. This work is the milestone for seakeeping considerations of planing hulls in terms of both experimental and empirical formulae developed by (Fridsma, 1971), reworked into equations by (Savitsky and Brown, 1976).

Another experimental study was carried out on a 1/8.25-scale model of the high-speed transom stern ship, R/V Athena, in order to provide data for comparison and evaluation of various analytical predictions (Jenkins, 1984). Tests were realized both under fixed, and free trim and sinkage conditions. The experimental results were compared with Dawson's analytical method applied on a 1/14.67-scale model in terms of total resistance, dynamic sinkage and trim values and wave heights along and behind the hull.

Main dimensions of the model play an important role in resistance tests of planing hulls. (Katayama et al., 2002) realized an experimental study on the scale effects on wetted surface area, frictional resistance and hydrodynamic forces acting on a very small prismatic model at high Froude numbers. The longitudinal center of gravity (LCG) is another important parameter on the running attitude of a planing vessel. (Kim et al., 2009) performed model tests in calm water for various test conditions in order to find out the effects of weight and center of gravity on the planing craft behaviour. (Danisman and Bastug, 2015) carried out several model tests of a small planing hull in order to observe the effects of LCG on resistance, dynamic trim, and sinkage.

Besides experimental works, nowadays, computational methods have become a very popular approach in the assessment of marine vehicle's hydrodynamic performance in early design stages. Although experimental approach is still very useful, it has limitations, such as scale effects and model tests need long time to get the results and are expensive. With the advancement of technology in computer hardware and software, the use of CFD has become widespread. CFD technique has a wide area of applications in ship hydrodynamics including viscous and inviscid methods. Inviscid methods are often used in the solution of the wave resistance problems while the viscous effects are included in the analyses by the viscous methods based on the solution of RANS equations. Today, it is possible to solve the complex flow around a planing hull with high accuracy by using commercially available software or other in-house codes that are capable of solving viscous flow equations.

In 2006, a report was published by the Naval Surface Warfare Center (Wilson et al., 2005) in order to compare the model test results of 1/8.25-scale model of R/V Athena (also known as NSWC Model 5365), reported in (Fu et al., 2005), with the predictions obtained by several CFD codes. The evaluation of the current capability of different CFD solvers was the main objective of this work. (Lee et al., 2016) also performed experiments both in calm water and in waves. The calm-water resistance, sinkage, and trim values over a wide range of speed were compared with those obtained by three different CFD codes. (Bhushan et al., 2007) developed a two-layer, two-point wall function model in a general purpose unsteady RANS solver to simulate model and full-scale ship flows for resistance, propulsion, seakeeping and maneuvering. Model and full-scale simulations were performed for R/V Athena both at fixed and free to sinkage and trim conditions. The results were compared with experimental data and full-scale in-situ measurements. In continuation of this work, a new study was realized (Wyatt et al., 2008) that includes the comparison of CFD simulations with high-resolution measurements of the breaking transom waves of a full-scale ship, again for R/V Athena.

Many other studies have recently been carried out on planing hulls to be able to simulate the planing phenomena more accurately. (Akkerman et al., 2012) employed a newly developed finite element based approach to compute Fridsma's hull in calm water. (Wang, 2016) used a commercial software to predict the resistance of planing vessel with using two phase flow theory. In simulations, he used dynamic grid to consider the effects of heave and pitch motion on the resistance of planing vessel. Grid structure plays an important role in planing hull simulation especially at high speeds where high amplitude vertical motions occur. To be able to handle the planing regime, the grid structure has to move freely with the moving object without any deformation. Although there are several grid techniques for the dynamic motion simulations, three of them are the most suitable methods for ship hydrodynamic simulations: the simple moving grid (or rigid grid), the diffusion-based smoothing method (or morphing grid), and the overset/Chimera grid. Assessment of the accuracy and effectiveness of different grid techniques on planing hulls can be found in (Casadei, 2010), (Stern et al., 2013) and (Mancini, 2015). The dynamic overset grid method, including a hierarchy of bodies that enable computation of ship motions with moving components, makes it possible to directly compute ship motions with large amplitudes. So far, overset grid method has been applied to the computations of ship hydrodynamics, especially for the simulation of planing hulls, self-propulsion and hull-propeller-rudder interaction problems. (Huang et al., 2012) presented a geometry-based level set method for curvilinear overset grids to overcome the limitations imposed by the small discontinuities caused by the overset interpolations. They applied their method to simulate the flow around the surface combatant model DTMB 5415 and ONR Tumblehome model DTMB 5613 with superstructure. (Araki et al., 2014) used overset grid method to analyse the bilge keel effects on roll damping. They performed roll decay and forced roll simulations of DTMB 5415 with/without bilge keels and compared their results with experiments. (Wang, 2016) applied an in-house CFD-based method to investigate the hydrodynamic performance of the fully appended ONR Tumblehome ship model for self-propulsion condition. During the simulation, the moving objects were handled by the dynamic overset grid method. (De Luca et al., 2016) presented a verification and validation study to evaluate the reliability of unsteady RANS (URANS) simulations applied to planing craft. They realized simulations for three different hull forms generated systematic variation of L/B ratio at four Froude numbers by using overset grid technique. They reported that greater simulation reliability was achieved by using the overset grid technique. (Sukas et al., 2017) also published a paper about hydrodynamic assessment of planing hulls by implementing overset grid and rigid body motion system. (Duman et al., 2017) carried out a study to compare the ability of overset and rigid grid techniques on the assessment of planing performance of a round-bilge high-speed vessel by performing several CFD analyses using both grid techniques.

The main objective of this study is to extend the previous work on the ability of different grid methods and investigate the effects of LCG on powering performance and planing characteristics of a round-bilge high-speed vessel. For this purpose, LCG is moved in forward and backward directions by 5% of L. First, the previous experiences and results where the validation of the method took place will be briefly given, then the new results will be presented.

2. COMPUTATIONAL METHOD

The multiphase flow field (air and water) has been modelled by the unsteady Reynolds-averaged Navier-Stokes (RANS) equations based on finite volume method (FVM). In order to obtain a well-posed algebraic equation system that can be solved on a computer, appropriate initial and boundary conditions and a number of discrete approximations are needed. First, the computational domain is subdivided into a finite number of control volumes (CVs). Fully hexahedral elements have been used to generate the grid system. The solution time is also subdivided into time steps according to ITTC (International Towing Tank Conference) recommendations for transient CFD (Computational Fluid Dynamics) solutions (ITTC, 2011).

The fluid flow is assumed as 3-D, incompressible, transient and fully turbulent. The flow field is governed by the RANS equations and Standard Realizable k-ε turbulence model which uses two-layer all y+ wall treatment. This approach attempts to calculate the velocity profiles near the no-slip wall according to the dimensionless wall y+ values. For coarse grids, it uses a logarithmic universal velocity profile to represent the flow in the boundary layer instead of solving the flow equations. This is achieved by setting the dimensionless wall y+ to be 30 or higher values. In the present study, y+ values are set to be in the range of 30-300 for all related Froude numbers.

During hydrodynamic analyses, the free surface effects have been included by using volume of fluid (VOF) method which is utilized by Eulerian fluid approach. The VOF method developed by (Hirt and Nichols, 1981) is a fixed grid technique designed for two or more fluids, where in each cell of a grid it is necessary to use only one value for each dependent variable defining the fluid state. The segregated flow solver is used to solve the RANS equations iteratively.

2.1 GOVERNING EQUATIONS

In the Cartesian coordinate system, the averaged continuity and momentum equations can be written in tensor notation as follows for an incompressible flow with constant viscosity and assuming there are no body forces acting on the hull (Ferziger and Perić, 2002):

$$\frac{\partial(\overline{u}_i)}{\partial x_j} = 0 \tag{1}$$

$$\frac{\partial(\overline{u}_i)}{\partial t} + \overline{u}_j \frac{\partial(\overline{u}_i)}{\partial x_j} + \frac{\partial(\overline{u'_i u'_j})}{\partial x_j} = -\frac{1}{\rho}\frac{\partial \overline{\mathrm{p}}}{\partial x_j} + \frac{\partial \overline{\tau}_{ij}}{\partial x_j} \tag{2}$$

in which $\overline{\tau}_{ij}$ are the mean viscous stress tensor components, as shown below:

$$\overline{\tau}_{ij} = \nu\left(\frac{\partial \overline{u}_i}{\partial x_j} + \frac{\partial \overline{u}_j}{\partial x_i}\right) \tag{3}$$

and p is the mean pressure, $\overline{u}_i$ is the average Cartesian components of the velocity vector, $\rho\overline{u'_i u'_j}$ is the Reynolds stress, ρ is the fluid density and ν is the kinematic viscosity coefficient.

2.2 CHOICE OF TIME STEP

The time step has been determined according to the ITTC CFD recommendations for transient solutions (ITTC, 2011). ITTC proposes the formula $\Delta t = 0.005 - 0.01L/V$, where L is the length between perpendiculars and V is the ship advance speed.

2.3 OVERSET GRID TECHNIQUE

Dynamic overset grid or grid-embedding technique where the grid system is able to move freely with the body, has been used for the transmission of flow properties between embedded boundaries and overlap region cells. The computational domain is divided into two main regions; background and overset. Unlike the common boundaries, embedded boundaries (or overset region boundaries) have the flexibility of arbitrary orientation without any deformation. According to this technique, the grid cells are classified into several types, such as fringe, hole, donor etc. The flow properties are transferred between overset region boundaries and background region cells (Benek et al., 1986).

3. COMPUTATIONAL RESULTS

In this work, Naval Surface Warfare Center Carderock Division (NSWCCD) Model 5365, a 1/8.25 scale model of R/V Athena hull, has been chosen to be used in hydrodynamic analyses which provides experimental data for validation of the CFD method.

Model 5365 is a round-bilge high-speed vessel with a transom stern. The model, built in 1979, was constructed out of wood and fiberglass. In 2002, it was measured using NSWCCD's laser tracker model measurement system. Since the 3-D geometry of the model cannot be obtained, it is remodelled in accordance with the lines plan (Jenkins, 1984). The 3-D view of the ship model is shown in Figure 1.

There are two design features for the increase in interest to the R/V Athena hull in its use for CFD validation: one is the large speed range of the model, corresponding to 11-41 knots full scale, representing a Froude number ranging from 0.28 to 1.00; the other one is the transom stern geometry of the hull form, which is a realistic form for a naval combatant.

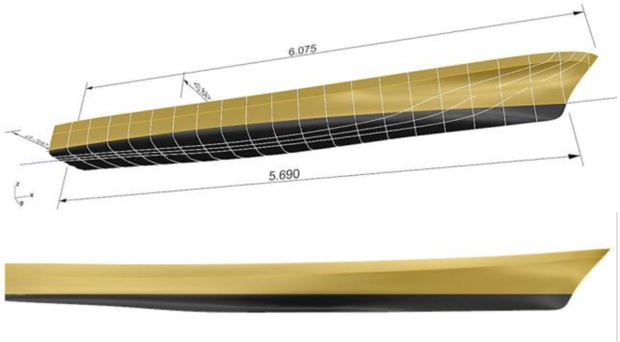

Figure 1. 3-D view of 5365.

In all simulations, the hull is free to heave and pitch motions. Hydrodynamic analyses have been carried out over a Froude number range of 0.28-1.00. The principal particulars of form 5365 are given in Table 1.

Table 1. Principal particulars of 5365.

	Full Scale	Model Scale
λ	1	8.25
L (m)	46.9	5.685
B (m)	6.9	0.836
T (m)	1.498	0.182
S (m^2)	287.36	4.222
Δ	229 tons	397 kg

3.1 GRID RESOLUTION AND BOUNDARY CONDITIONS

The sizes of domain have been chosen according to the previous experience on free surface flow hydrodynamic analyses (Duman, 2016) and related studies in literature to simulate the flow around the ship properly (Table 2). Since the problem has a symmetric behaviour, only half of the solution domain is used for the simulations in order to reduce the computational cost.

A xyz-Cartesian coordinate system where the origin is the intersection of forward perpendicular and base line, is adopted. The hull surfaces are identified as no-slip walls where the normal and tangential components of the velocity are to be zero. Front, top and bottom faces of the computational domain are defined as velocity inlets. Side faces are assigned as symmetry-planes and the back face is defined as pressure outlet (Figure 4).

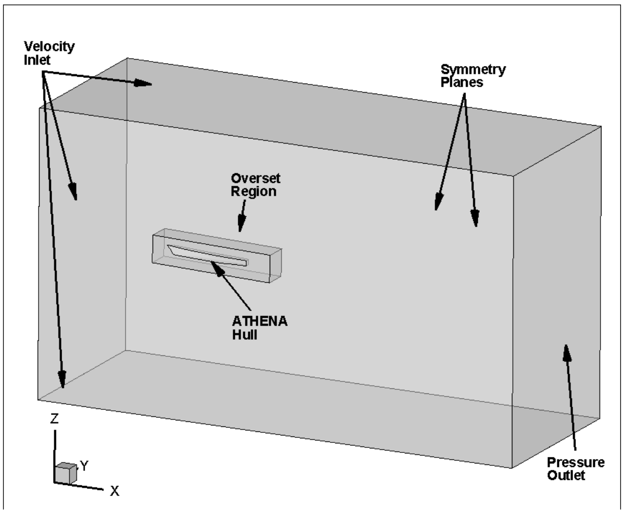

Figure 2. Boundary conditions.

The transmission of the flow properties between background and overset region is achieved via overset boundaries where the linear interpolation technique is applied. In order to calculate the free surface deformations at the interaction of two phases (air and water), the free surface is assigned as calm water initially.

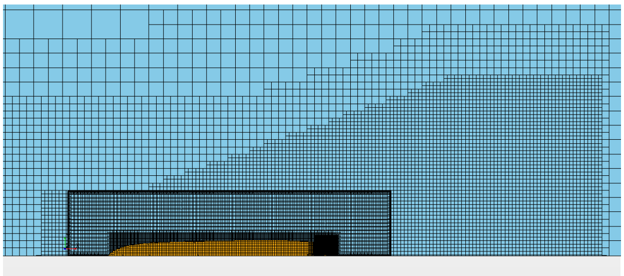

Figure 3. Kelvin wave adopted grid.

The Kelvin wave adopted grid (Duman, 2016) have been used to capture the free surface deformations accurately (Figure 3). The dimensions of the computational domain are shown in Table 2. Upstream is in the -ve x-direction and downstream is in the +ve x-direction. The top boundary distance is given between top of domain and the origin of xyz-Cartesian coordinate system.

Table 2. Computational domain dimensions.

Domain dimensions (m):			λ=8.25
Boundaries	Upstream	1.8L	10.233m
	Downstream	3.6L	20.465m
	Top	1.6L	9.096m
	Bottom	2.1L	11.938m
	Transverse	2.4L	13.644m

Finite volume method with fully hexahedral elements has been applied to discretize the computational domain. Local refinements have been used around the hull, bow and stern, free water surface and wake zone (Figure 4) to obtain a good resolution grid.

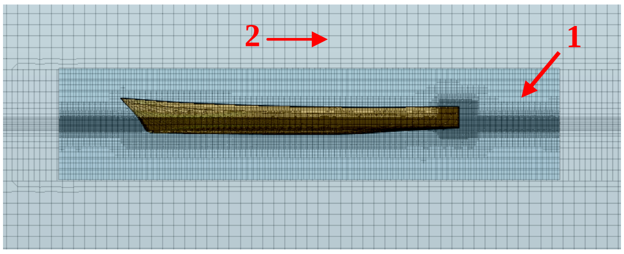

Figure 4. Grid structure around the hull.

In Figure 4, number “1” and “2” indicate the grid structure of overset region and background region, respectively. The total boundary layer thickness around the hull is determined by the dimensionless wall y+ values to be in the range of 30-300 for all related Froude numbers.

In the comparison of overset and rigid grid techniques, care has been taken to ensure the cell sizes on and near the hull and around the free surface to be similar. The sizes of domain, total boundary layer thickness, time step and other numerical parameters remain the same.

3.2 VERIFICATION AND VALIDATION

3.2 (a) Study on Grid Independence

In the present study, three different solution verification methods based on Richardson Extrapolation (RE) have been implemented to obtain uncertainties in the CFD simulations. These are Grid Convergence Index (GCI), which was developed by (Roache, 1994), Correction Factor (CF) (Stern et al., 2001) and Factors of Safety (FS) methods (Xing and Stern, 2010). The ITTC Guidelines (ITTC, 2008) recommend the refinement factor values to be between √2 and 2. Due to non-integer grid refinements have been used in the spatial discretization, the refinement factors were calculated by considering the total cell numbers (Eqn. 4).

$$r_{21} = \left(\frac{N_1}{N_2}\right)^{1/3} \qquad r_{32} = \left(\frac{N_2}{N_3}\right)^{1/3} \qquad (4)$$

where N_1, N_2 and N_3 are total cell numbers and $N_3<N_2<N_1$. The difference between any scalar results (total resistance in this case) of the simulations of two different grids can be calculated as follows:

$$E_{21} = X_2 - X_1 \qquad E_{32} = X_3 - X_2 \qquad (5)$$

It should be noted that the verification study has been done for Froude number 1 which can be regarded as the most challenging case in this study. Convergence ratio R is equal to the ratio of E values (Eqn. 5).

The group of uncertainty assessment was selected as a triplet of different grid sizes, i.e., fine, medium and coarse grids. The convergence ratio for overset grid uncertainty assessment was calculated as 0.65 which indicated that the monotonic convergence was achieved (Phillips and Roy, 2014).

Table 3. Overset grid results for different grid qualities.

Grid quality	Cell #	R_T-CFD
fine	1,685,535	458.409
medium	695,021	448.565
coarse	305,973	433.517

The uncertainties in the computations were calculated as 4.27%, 5.01% and 5.97% for fine overset grid at Froude number of 1.00 with GCI, CF and FS methods, respectively. Since the relative error between fine and medium grids is about 2.14% (see Table 3), medium grid has been used in the simulations in order to reduce the computational cost. Note that the second-order accuracy (P_{th}) was used in the estimations of uncertainties of spatial discretization. Detailed information about the uncertainty formulations can be found in (Celik et al., 2008), (Stern et al., 2001) and (Xing and Stern, 2010).

The uncertainties of CFD simulations according to three different methods are given in Table 4. Here, P represents the ratio of observed order of accuracy (P_{RE}) obtained by RE to the theoretical one (P_{th}). The results show that the FS method is more conservative than the others for the overset grid method.

Table 4. Uncertainty assessment for overset grid.

Uncertainty analyses	1-2-3 triplet-grid
r_{21}	1.34
r_{32}	1.31
P_{th}	2.00
P_{RE}	1.62
P	0.82
RT_{EXT} (N)	474.059
SF_{GCI}	1.25
δ_{GCI} %	4.27
U_{GCI} (N)	19.56
SF_{CF}	0.78
δ_{CF} %	5.01
U_{CF} (N)	22.49
SF_{FS}	1.74
δ_{FS} %	5.97
U_{FS} (N)	27.35

Table 5. Rigid grid results for different grid qualities.

Grid quality	Cell #	R_T-CFD
fine	1,166,272	450,643
medium	529,874	445,559
coarse	203,412	477,497

Table 6. Uncertainty assessment for rigid grid.

Uncertainty analyses	1-2-3 triplet-grid
r_{21}	1.30
r_{32}	1.37
P_{th}	2.00
P_{RE}	6.94
P	3.47
RT_{EXT} (N)	451.619
SF_{GCI}	1.25
δ_{GCI} %	0.27
U_{GCI} (N)	1.22
SF_{CF}	7.52
δ_{CF} %	2.87
U_{CF} (N)	13.71
SF_{FS}	42.13
δ_{FS} %	9.23
U_{FS} (N)	41.13

Unlike the overset grid, the convergence ratio R was calculated as -0.15 for rigid grid which indicated an oscillating convergence. The uncertainties for fine rigid grid were found as 0.27%, 2.87% and 9.23% at Froude number of 1.00 with GCI, CF and FS methods, respectively. The relative error between fine and medium rigid grids is about 1.13% (see Table 5). Therefore, medium grid has been chosen for CFD simulations to reduce computational cost. Detailed information about the convergence types of numerical simulations can be found in (Stern et al., 2006).

As it can be seen from Table 4 and Table 6, FS method is more conservative than GCI and CF methods for the both overset and rigid grid methods. The highest value of uncertainties for overset and rigid grids should be taken into consideration to be in safe side.

3.2 (b) Comparison of Resistance Coefficients

The results of computational analyses were compared with the available experimental data in terms of total and residual resistance coefficients, free surface deformations and dynamic trim and sinkage values. The experimental results for 2 degree-of-freedom (2-DOF) condition were taken from (Jenkins, 1984). The comparison of total resistance coefficients is shown in Figure 5. The total resistance and lift forces are nondimensionalized as follows:

$$C_T = \frac{R_T}{0.5\rho S V^2} \tag{6}$$

where R_T is total resistance, ρ is density, S is the wetted surface area and V is the ship advance speed. The wetted surface area has been assumed constant as 4.222 m^2 to compare the computational results with experiments, given in (Jenkins, 1984).

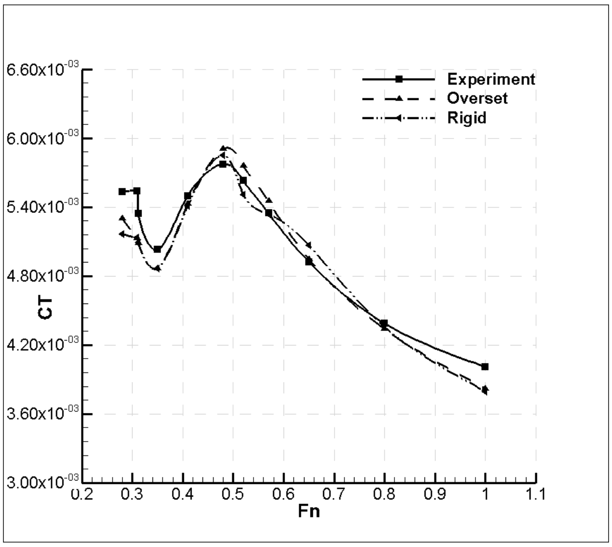

Figure 5. Total resistance coefficient comparison of different grid types.

The total and residual resistance coefficients and their comparison with the experimental data are given in Tables 7-10. The experimental results are not explicitly given, but one can reach these values by making calculations from the tabulated data or directly from the relevant references. The relative error in this study is calculated by using the following formula:

$$\varepsilon = \frac{C_{T,CFD} - C_{T,Exp}}{C_{T,Exp}} x100 \tag{7}$$

It is found that the numerical results of both grid techniques are compatible with the experiments in terms of total resistance coefficient (Figure 5 and Tables 7-8). It can be noticed that the hull enters the planing regime about the Froude number of 0.52 where the resistance coefficient starts to decrease. At higher Froude numbers after this point, the hydrodynamic lifting forces become effective.

The errors of overset grid are smaller than those of rigid grid for all Froude numbers except for (0.312, 0.48, 0.57 and 0.80). Moreover, the overset grid shows more stable characteristics than the rigid grid (rigid grid has oscillations around 0.48-0.8 Froude numbers) (see Figures 5-6). Although there is not a direct correlation in the relative errors, general characteristics of overset and rigid grid results are in good agreement with the experimental results. Further investigations on the effects of grid quality on numerical results are still needed.

The residual resistance coefficients are also estimated satisfactorily and very close to the experiments by both grid techniques in the range of 0.35-0.80 Froude numbers. However, the relative error increases above Fn=0.80 due to the fact that the URANS approach underestimates the pressure-based resistance components (see Figure 6 and Tables 9-10).

Table 7. CT values computed by overset and rigid grids.

Froude number	C_Tx10^{-3} (overset)	C_Tx10^{-3} (rigid)
0.28	5.193	5.070
0.31	5.005	5.033
0.312	4.963	4.991
0.35	4.745	4.714
0.41	5.256	5.234
0.48	5.710	5.667
0.52	5.564	5.304
0.57	5.234	5.129
0.65	4.704	4.814
0.80	4.031	4.049
1.00	3.372	3.357

Table 8. C_T relative errors of overset and rigid grids.

Froude number	$\varepsilon_{overset}$ %	ε_{rigid} %
0.28	4.13	6.54
0.31	7.40	7.27
0.312	4.83	4.75
0.35	3.21	3.24
0.41	1.25	1.55
0.48	2.27	1.36
0.52	2.30	2.14
0.57	1.97	0.19
0.65	0.49	2.92
0.80	1.15	0.66
1.00	4.68	5.31

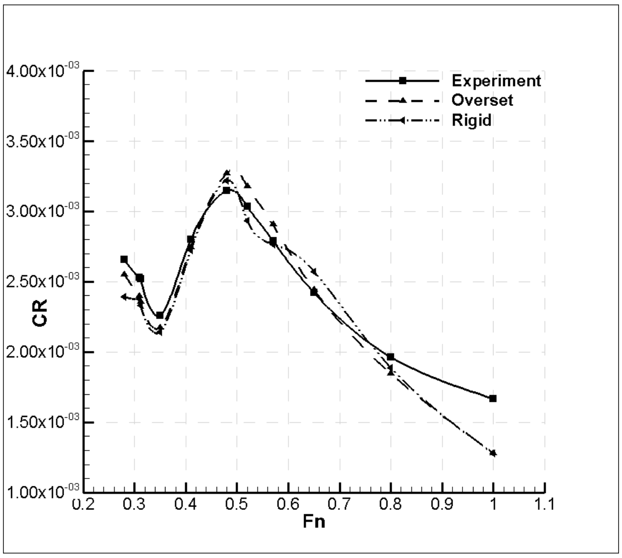

Figure 6. Residual resistance coefficient comparison of different grid types.

Table 9. C_R values computed by overset and rigid grids.

Froude number	C_Rx10^{-3} (overset)	C_Rx10^{-3} (rigid)
0.28	2.551	2.391
0.31	2.395	2.375
0.312	2.356	2.331
0.35	2.172	2.143
0.41	2.746	2.724
0.48	3.272	3.219
0.52	3.176	2.933
0.57	2.907	2.765
0.65	2.443	2.572
0.80	1.845	1.887
1.00	1.280	1.277

Table 10. C_R relative errors of overset and rigid grids.

Froude number	$\varepsilon_{overset}$ %	ε_{rigid} %
0.28	3.91	9.94
0.31	5.32	6.15
0.312	6.51	7.52
0.35	3.91	5.16
0.41	1.91	2.71
0.48	4.04	2.35
0.52	4.72	3.31
0.57	4.19	0.91
0.65	0.95	6.30
0.80	6.02	3.89
1.00	23.18	23.34

In addition to the CFD results, the ITTC-1957 frictional correlation line (ITTC, 2002) is added to compare the frictional resistance coefficients. The computational results for both grid techniques are totally agree with the experiments and the correlation line between 0.41-0.65 Froude numbers while there are some discrepancies at low speeds (Figure 7). Above the 0.65 Froude number, on the other hand, the CFD results are deviated from the experiment and the correlation line. The main reason to be considered here is that a logarithmic universal velocity profile is used to calculate the velocities around the no-slip boundaries instead of solving the flow equations in the boundary layer. This may cause the differences at high speeds.

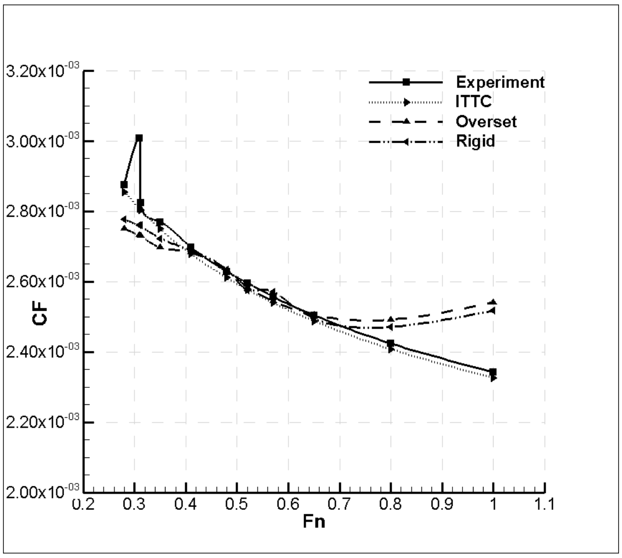

Figure 7. Frictional resistance comparison of different grid types.

3.2 (c) Free Surface Deformations

The non-dimensional wave profiles on the hull at 0.65 Froude number are shown in Figure 8 as compared with the experimental data where the x-axis is the non-dimensional longitudinal distance from FP (fore peak) to AP (aft peak) and the y-axis is non-dimensional wave height. The wave heights are non-dimensionalized by $V^2/2g$ as described in (Jenkins, 1984), and are referenced to the calm water free surface, where V is the advance speed of ship and g is the gravitational acceleration.

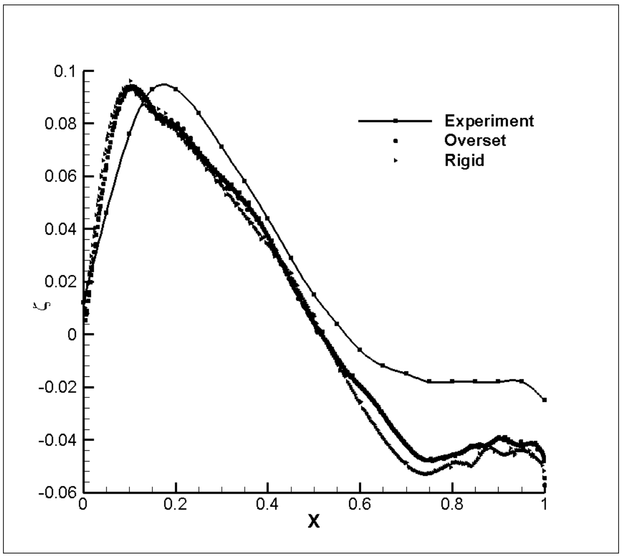

Figure 8. Comparison of wave profiles on the hull at 0.65 Froude number.

The height of bow waves in the fore region is in accordance with experiment. However, a small phase difference between computational and experimental results can be noticed. There is also a decrease and an oscillatory behaviour of wave deformations obtained by CFD method in the aft part of the hull when compared to the experimental results (Figure 8).

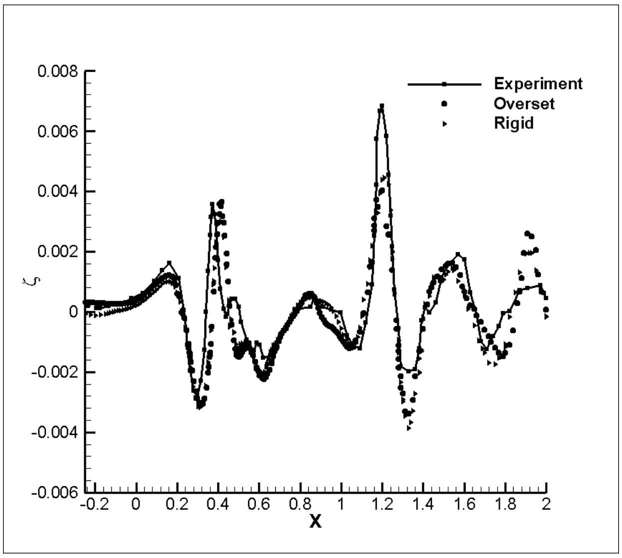

Figure 9. Comparison of wave profiles along the hull at 0.252 Froude number (y/B=0.86).

A wave profile from y/B=0.86 at 0.252 Froude number is also shown in Figure 9. The experimental wave profile data have been taken from (Wilson et al., 2005). The wave profiles by computational methods are generally in good agreement with the experimental result.

The Kelvin wave patterns in the dominant wave system were captured accurately with both techniques (Figure 10).

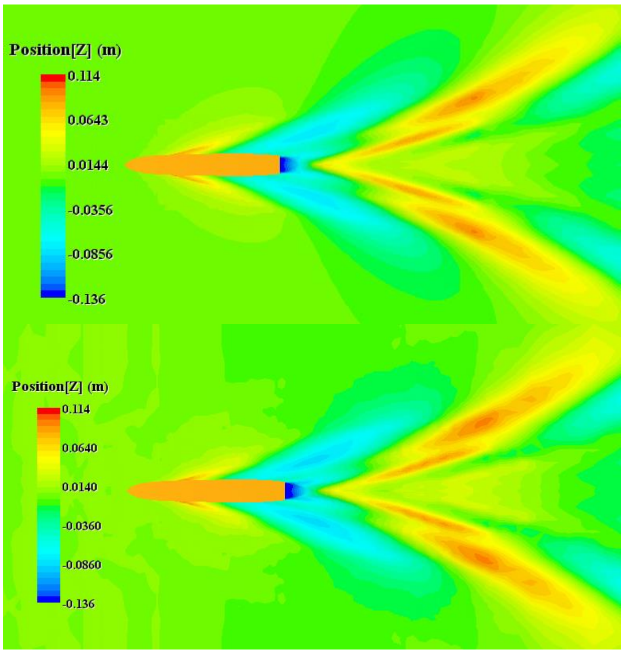

Figure 10. Comparison of Kelvin wave patterns at 0.65 Froude number; overset (top) and rigid grid (bottom).

3.2 (d) Pressure Distributions and Dynamic Behaviour of the Hull

The pressure distributions on the bottom of hull are shown in Figure 11 both for overset and rigid grids at 1.0 Froude number. The pressure centres for both grid techniques are located approximately at the same position as indicated with arrows (Figure 11). The dynamic pressures acting on the hull at a specific advance speed are non-dimensionalized using Eqn. 8.

$$C_P = \frac{P_A - P_\infty}{0.5\rho V^2} \tag{8}$$

where P_A is the actual pressure, P_∞ is the undisturbed free stream pressure, ρ is density, and V is the advance speed of ship.

The dynamic trim and sinkage values obtained by numerical simulations are also compared with the experimental data (Figure 12-13). The oscillatory behaviour of the rigid grid results can be noticed between 0.48-0.8 Froude numbers while the overset grid gives smoother values.

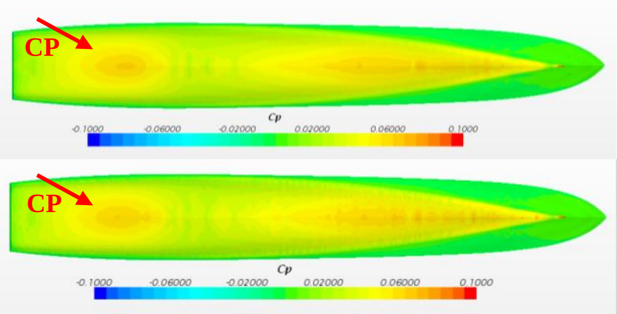

Figure 11. Comparison of Cp distributions on the hull bottom at 1.00 Froude number; overset (top) and rigid grid (bottom).

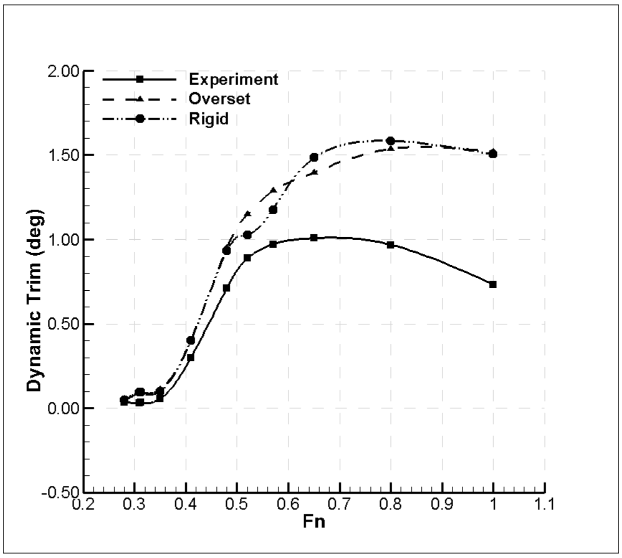

Figure 12. Comparison of dynamic trim values.

The fluctuations around the start of planing regime reduces the reliability of rigid grid technique for high speed planing vessel simulations when compared with the overset grid since general characteristics of the overset results are more stable considering the overall table.

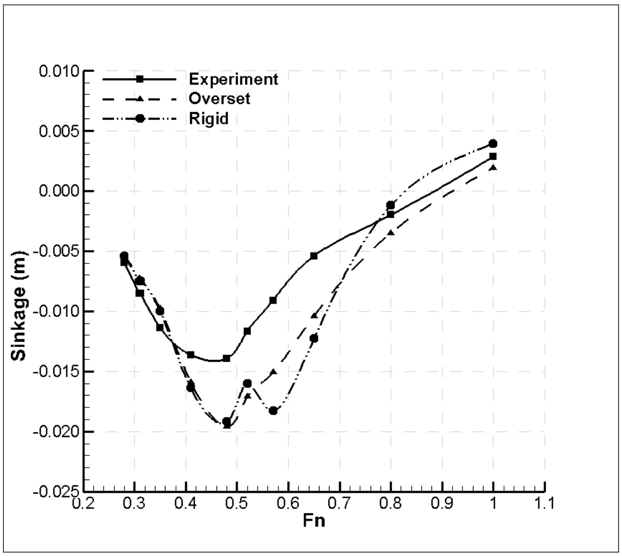

Figure 13. Comparison of sinkage values.

3.3 EFFECTS OF LCG CHANGE ON THE HYDRODYNAMIC PERFORMANCE

A study has been carried out to investigate the effects of LCG position on the powering and planing performance of R/V Athena hull. LCG is moved from its original position to forward (-ve direction) and backward (+ve direction) by 5% of L and the hydrodynamic analyses are redone. It should be noted that only overset grid technique is used here.

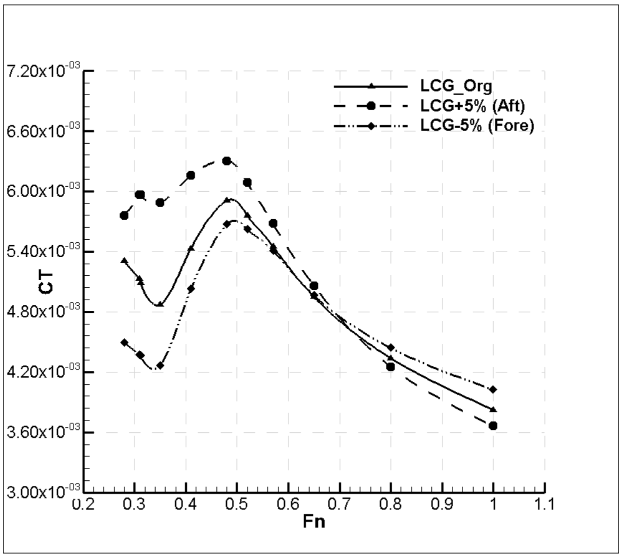

Figure 14. Total resistance coefficients for different LCG

Total, residual and frictional resistance coefficients are given in Figures 14-16. LCG_Org represents the original position of the gravity center. Note that forward movement of LCG causes a decrease in total and residual resistance coefficients below the 0.65 Froude number. However, an increase in frictional resistance coefficients has been observed for the given range of Froude numbers (Figure 16). In addition, an increase in total and residual resistance coefficients and a decrement in frictional resistance values have been obtained by the backward movement of LCG. When the planing regime is considered, moving the gravity center by the stern gives better results (total resistance values) (Figure 14) above the 0.65 Froude number than moving it by forebody.

Non-dimensional lift force coefficients have also been computed. The advance speed at Fn=0.28 has been chosen as the reference speed. Note that the hydrodynamic lifting force coefficients of backward movement of LCG are greater than those of forward movement (Figure 17). The main reason for this is that the ship moves with a higher angle of attack in the case of backward movement of LCG and this makes the hull easy to enter to the planing regime.

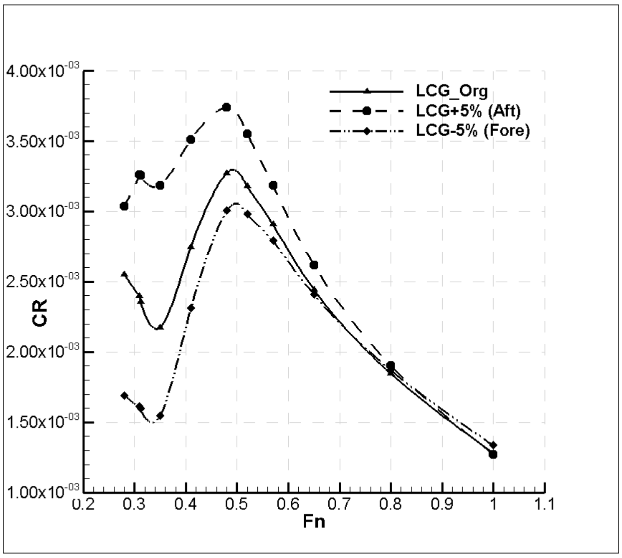

Figure 15. Residual resistance coefficients for different LCG

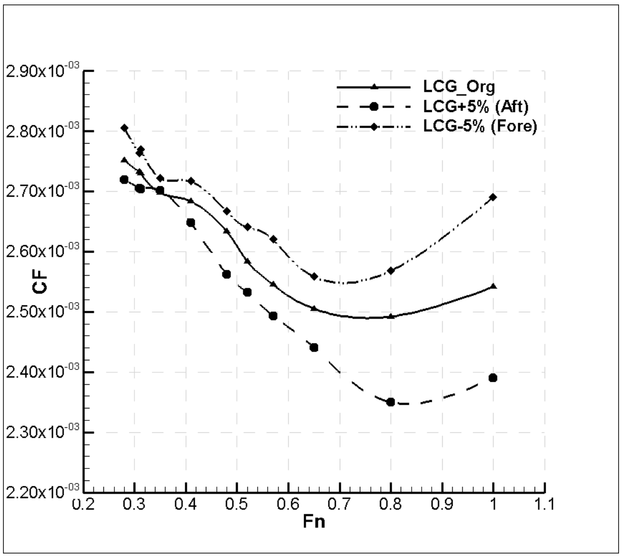

Figure 16. Frictional resistance coefficients for different LCG

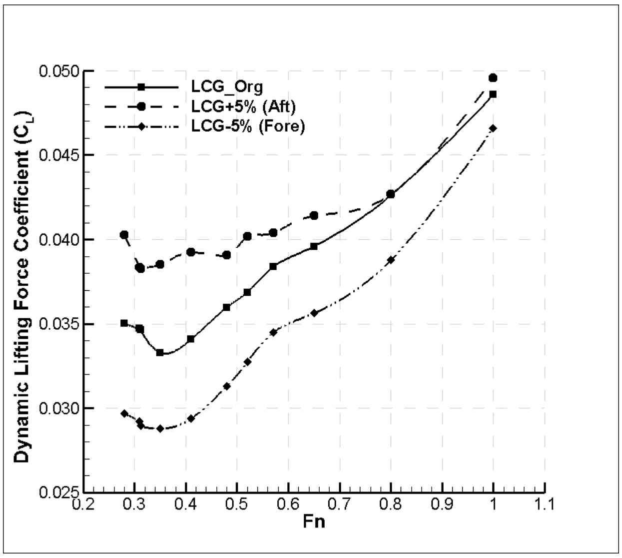

Figure 17. Comparison of dynamic lifting force coefficients

Dynamic trim and sinkage values have been computed and compared with those of original position of LCG (Figures 18-19). Here, the zero value of sinkage means that the gravity center of the ship hull is at its original position, -ve sinkage values mean that the gravity center of the ship hull is in the negative z-direction and +ve sinkage values indicates that the ship hull is lifted up.

There are significant differences between forward and backward movement of LCG. For the range of Froude numbers given here, forward movement of LCG generates lower angles of dynamic trim but causes higher sinkage values which is resulted in larger wetted surface areas (Figure 20). On the other hand, backward movement of LCG gives opposite results except for low speeds where the sinkage values are almost the same with the original position of LCG.

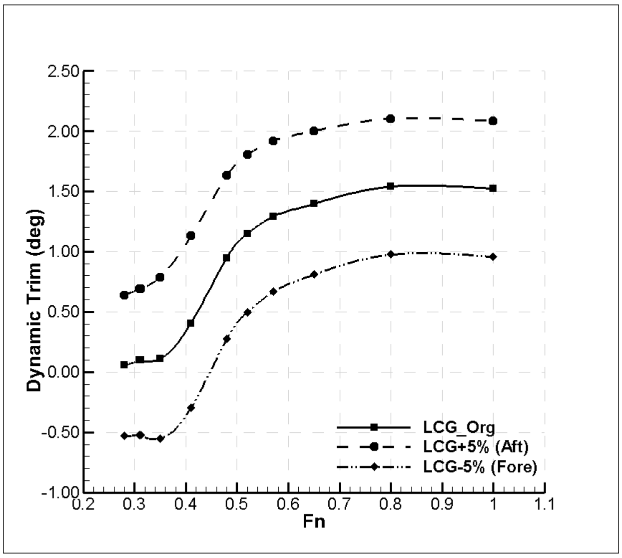

Figure 18. Dynamic trim values for different LCG

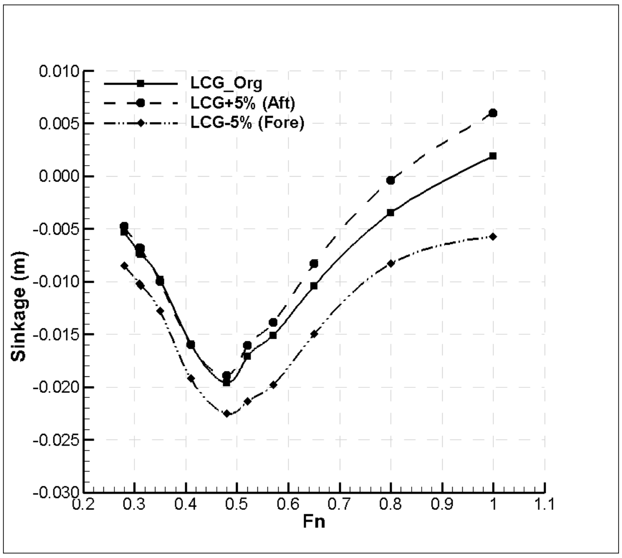

Figure 19. Dynamic sinkage values for different LCG

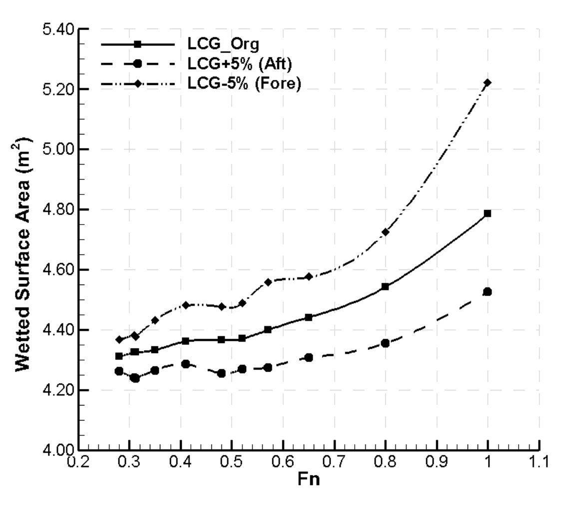

Figure 20. Wetted surface area for different LCG

4. CONCLUSIONS

The hydrodynamic analyses of R/V Athena in 1/8.25 model scale have been carried out over a wide range of Froude numbers (0.28-1.00) by using unsteady RANS approach. CFD analyses have been carried out under free to sinkage and trim conditions. Two different grid techniques have been implemented to discretize the computational domain. The verification study has been conducted at Froude number 1.00 using three different methods based on Richardson Extrapolation: GCI, CF and FS. A study has been carried out to investigate the effects of changes in LCG on powering and planing performance of the hull.

It is found that reasonably accurate results can be provided by the unsteady RANS computations for 2-DOF flow simulations of high-speed round-bilge planing vessels with overset and rigid grid techniques. The Kelvin wave patterns, wave elevations on and along the hull are captured accurately with both grid techniques.

In the range of Froude numbers (0.35-0.80), both grid techniques estimate the resistance values satisfactorily, while the errors are high at Fn=1.00. Two main reasons of this can be given as follows:

i. URANS approach underestimates the pressure-based resistance components.
ii. A logarithmic universal velocity profile is used in order to calculate the velocities in boundary layer instead of solving the flow equations.

On the other hand, overset technique is more successful at low speeds and gives much satisfactorily results when compared with rigid grid results especially between 0.48-0.80 Froude numbers which corresponds to the transition zone to the planing regime. The fluctuations around the start of planing regime reduce the reliability of rigid grid technique for high speed planing vessel simulations.

It is also found that the movement of LCG in backward or forward directions has significant effects on powering and planing performance of the high-speed vessel. Firstly, an increase in hydrodynamic lifting force coefficients (C_L) is found by the backward movement of LCG. Although the total and residual resistance values are lower at forward movement of LCG at low speeds, moving LCG to the stern provides a better planing performance. Note that the movement of LCG to the stern can cause a decrease in wetted surface area and also in frictional resistance. The other effects of change in LCG are listed below:

i. For the selected range of Froude numbers, the forward movement of LCG causes lower dynamic trim angles but higher sinkage values. This (forward movement of LCG) means larger wetted surface areas.
ii. Backward movement of LCG gives almost the same sinkage values with those of original LCG for Froude numbers below 0.48.

In future work, turning and zig-zag maneuvers of R/V Athena will be carried out using overset grid technique and manoeuvring parameters will be predicted. Heeling effects on turning performance will be investigated. The effects of design parameters such as LCB (longitudinal center of buoyancy), main dimensions, frontal areas, form coefficients etc. on hydrodynamic performance of high-speed vessels will also be investigated.

5. ACKNOWLEDGEMENT

The authors wish to thank Dr. Thomas Fu from NSWCCD for sharing the geometrical and experimental data of R/V Athena hull.

6. REFERENCES

1. AKKERMAN, I., DUNAWAY, J., KVANDAL, J., SPINKS, J., BAZILEVS, Y. (2012) *Toward free-surface modeling of planing vessels: simulation of the Fridsma hull using ALE-VMS*. Comput. Mech. 50, 719–727. https://doi.org/10.1007/s00466-012-0770-2.
2. ARAKI, M., OHASHI, K., HIRATA, N. (2014) *An Analysis of Bilge Keel Effects using RANS with Overset Grids Method*. Presented at the The 14th International Ship Stability Workshop (ISSW), Kuala Lumpur, Malaysia.
3. BENEK, J.A., STEGER, J.L., DOUGHERTY, F.C., BUNING, P.G. (1986) *Chimera: A Grid-Embedding Technique (No. AEDC-TR-85-64).* Arnold Engineering Development Center, Arnold Air Force Station, Tennessee.
4. BHUSHAN, S., XING, T., CARRICA, P., STERN, F. (2007) *Model- and Full-Scale URANS/DES Simulations for Athena R/V Resistance, Powering, and Motions.* Presented at the 9th International Conference on Numerical Ship Hydrodynamics, Ann Arbor, Michigan, pp. 122–142.
5. CASADEI, G.M. (2010) *Dynamic-Mesh Techniques for Unsteady Multiphase Surface-Ship Hydrodynamics (Master's Thesis).* The Pennsylvania State University.
6. CELIK, I., GHIA, U., ROACHE, P.J., CHRISTOPHER, J.F. (2008) *Procedure for Estimation and Reporting of Uncertainty Due to Discretization in CFD Applications.* J. Fluids Eng. 130, 078001. https://doi.org/10.1115/1.2960953.
7. DANISMAN, D.B., BASTUG, T.B. (2015) *An Experimental Study of the Effect of Change in LCG on Resistance and Planing Capability of a Fast Vessel.* The 4th International Conference on Advanced Model Measurement Technology for the Maritime Industry (AMT'15). September 28-30, Istanbul Turkey.
8. DE LUCA, F., MANCINI, S., MIRANDA, S., PENSA, C. (2016) *An Extended Verification and Validation Study of CFD Simulations for Planing Hulls.* J. Ship Res. 60, 101–118. https://doi.org/10.5957/JOSR.60.2.160010.
9. DUMAN, S. (2016) *Investigation of the Turning Performance of a Surface Combatant with URANS (Master's Thesis).* Istanbul Technical University.
10. DUMAN, S., SENER, B., BAL, S. (2017) *Performance Prediction of a Planing Vessel Using Dynamic Overset Grid Method.* 11th Symposium on High Speed Marine Vehicles, October 25-26, Napoli, Italy.
11. FERZIGER, J.H., PERIĆ, M. (2002) *Computational methods for fluid dynamics,* 3., ed. ed. Springer, Berlin.
12. FRIDSMA, G. (1969) *A Systematic Study of the Rough-Water Performance of Planing Boats (Part I) (Technical Report).* Davidson Laboratory, Stevens Institute of Technology, Castle Point Station, Hoboken, NJ.
13. FRIDSMA, G., (1971). *A Systematic Study of the Rough-Water Performance of Planing Boats (Part II) (Technical Report).* Davidson Laboratory, Stevens Institute of Technology, Castle Point Station, Hoboken, NJ.
14. FU, T., KARION, A., PENCE, A., RICE, J., WALKER, D., RATCHLIFFE, T. (2005) *Characterization of the Steady Wave Field of the High Speed Transom Stern Ship – Model 5365 Hull F*orm (Technical Report No. NSWCCD-50-TR-2005/046). Carderock Division Naval Surface Warfare Center, West Bethesda, Maryland.
15. HIRT, C., NICHOLS, B. (1981) *Volume of fluid (VOF) method for the dynamics of free boundaries*. J. Comput. Phys. 39, 201–225. https://doi.org/10.1016/0021-9991(81)90145-5.

16. HUANG, J., CARRICA, P.M., STERN, F. (2012) *A geometry-based level set method for curvilinear overset grids with application to ship hydrodynamics.* Int. J. Numer. Methods Fluids 68, 494–521. https://doi.org/10.1002/fld.2517.
17. ITTC (2002) *Resistance, Uncertainty Analysis, Example for Resistance Test (Recommended Procedures No. 7.5-02-02-02).* International Towing Tank Conference.
18. ITTC (2008) *Uncertainty Analysis in CFD Verification and Validation Methodology and Procedures (Recommended Procedures and Guidelines No. 7.5-03-01-01).* International Towing Tank Conference.
19. ITTC (2011) *Practical Guidelines for Ship CFD Applications.* Presented at the Proceedings of 26th ITTC, Rio de Janerio, Brazil.
20. Jenkins, D.S. (1984) *Resistance Characteristics of the High Speed Transom Stern R/V Athena in the Bare Hull Condition, Represented by DTNSRDC Model 5365 (Technical Report No. DTNSRDC-84/024).* David W. Taylor Nval Ship Research and Development Center, Bethesda, Maryland.
21. KATAYAMA, T., HAYASHITA, S., SUZUKI, K., IKEDA, Y. (2002) *Development of Resistance Test for High-Speed Planing Craft Using very Small Model -Scale Effects on Drag Force-.* Presented at the Proceedings of Asia Pacific Workshop on Marine Hydrodynamics (APHydro), Kobe, Japan.
22. KIM, D.-J., RHEE, K.-P., PARK, H.-S. (2009) *A Study on the Effects of Weight and Center of Gravity of a Planing Craft on Running Attitude.* J. Soc. Nav. Archit. Korea 46, 335–342. https://doi.org/10.3744/SNAK.2009.46.3.335.
23. LEE, E., FULLERTON, A., GEISER, J., SCHLEICHER, C., MERRILL, C., WEIL, C., JIANG, M., LIEN, V., MORIN, J. (2016) *Experimental and Computational Comparisons of the R/V Athena in Calm Water.* Presented at the 31st Symposium on Naval Hydrodynamics, Monterey, CA, USA.
24. MANCINI, S. (2015) *The Problem of the Verification and Validation Processes of CFD Simulations of Planing Hulls (PhD Thesis).* Universita Degli Studi Di Napoli Federico II.
25. PHILLIPS, T. S., and ROY, C. J. (2014) *Richardson Extrapolation Based-Discretization Uncertainty Estimation for Computational Fluid Dynamics.* J. Fluids Eng. 136, 121401, 1-10. https://doi.org/10.1115/1.4027353.
26. ROACHE, P.J. (1994) *Perspective: A Method for Uniform Reporting of Grid Refinement Studies.* J. Fluids Eng. 116, 405. https://doi.org/10.1115/1.2910291.
27. SAVITSKY, D. (1964) *Hydrodynamic Design of Planing Hull.* Mar. Technol. 1, 1–25.
28. SAVITSKY, D., BROWN, P.W. (1976) *Procedures for Hydrodynamic Evaluation of Planing Hulls in Smooth and Rough Water.* Mar. Technol. 13, 381–400.
29. STERN, F., WILSON, R., COLEMAN, H. W., and PATERSON, E. G. (2001) *Comprehensive Approach to Verification and Validation of CFD Simulations-Part 1: Methodology and Procedures.* Journal of Fluids Engineering 123, 793-802. https://doi.org/10.1115/1.1412235.
30. STERN, F., WILSON, R., SHAO, J. (2006) *Quantitative V&V of CFD simulations and certification of CFD codes.* Int. J. Numer. Methods Fluids 50, 1335–1355. https://doi.org/10.1002/fld.1090.
31. STERN, F., YANG, J., WANG, Z., SADAT-HOSSEINI, H., MOUSAVIRAAD, M., BHUSHAN, S., XING, T. (2013) *Computational ship hydrodynamics: Nowadays and way forward.* Int. Shipbuild. Prog. 3–105. https://doi.org/10.3233/ISP-130090.
32. SUKAS, O.F., KINACI, O.K., CAKICI, F., GOKCE, M.K. (2017) *Hydrodynamic assessment of planing hulls using overset grids.* Appl. Ocean Res. 65, 35–46. https://doi.org/10.1016/j.apor.2017.03.015.
33. WANG, Y. (2016) *Numerical Prediction of Resistance of Planning Vessel with RANS Method.* Atlantis Press. https://doi.org/10.2991/iccsae-15.2016.55.
34. WILSON, W., FU, T., PENCE, A. (2005) *Comparison of Predicted and Measured Wavefields for Model 5365 Hull Form (Technical Report No. NSWCCD-50-TR-2006/014).* Carderock Division Naval Surface Warfare Center, West Bethesda, Maryland.
35. WYATT, D.C., FU, T.C., TAYLOR, G.L., TERRILL, E.J., XING, T., BHUSHAN, S., O’SHEA, T.T., DOMMERMUTH, D.G. (2008) *A Comparison of Full-Scale Experimental Measurements and Computational Predictions of the Transom-Stern Wave of the R/V Athena I.* Presented at the 27th Symposium on Naval Hydrodynamics, Seoul, Korea.
36. XING, T., and STERN, F. (2010) *Factors of Safety for Richardson Extrapolation.* Journal of Fluids Engineering 132, 061403, 1-13. https://doi.org/10.1115/1.4001771.

DISCUSSION

DYNAMIC STABILITY OF FOILBORNE HYDROFOIL/SWATH WITH ANHEDRAL FOIL CONFIGURATION

S Williams, Massachusetts Institute of Technology, USA and **S Brizzolara**, Virginia Tech, USA

(Vol 159 Part B2, 2017)

COMMENT

Ray Vellinga, President, International Hydrofoil Society

The paper represents a promising hydrofoil design. However in my opinion there is one important flaw that needs to be addressed. Without some modification, the craft as designed will have problems with a destructive yaw / outside-roll couple.

It is my observation through model testing that when this craft yaws or turns to port it will roll to the outside, i.e., starboard. This is unlike most conventional stable designs where a yaw initiating a turn or side-slip to port will induce a rolling moment to the port resulting in a balanced turn. This is commonly called "rolling into the turn", and that is normal in boats, hydrofoils, and aircraft. Rolling to the outside is unstable.

To prove this assertion, a short series of mathematical calculations were performed to estimate and quantify the problem – see Table Ia and Ib.

It's a matter of coincidence that some years back I tested two models with similar anhedral front foils that were 45° off horizontal (the paper assumes 40°). Performed were simple drag-by-wire shallow water runs along the shore, at the San Diego Model Basin, where I observed the same instability that I believe will affect the anhedral model in question – see figures 1-4.

To make the calculations I first applied a simplified lift formula, $L = V^2 * S * C_{L,}$ The symbols are Lift, Velocity, Surface Area, and Coefficient of lift. The scale is roughly extrapolated from my personal prototype, Hyfibe, which has demonstrated good flying characteristics. Early tests can be observed here: https://www.youtube.com/watch?v=TViDOm9HQsw&t=15s. After assuming lift, velocity, and coefficient of lift, the formula was modified to solve for area. Then the formula was modified in 15 cases to reflect straight-and-level then yaw angles of 1° through 7° with both positive and negative signs. The yaw changes the angle of attack and that changes the coefficient of lift therefore requiring a change in wetted area to maintain the necessary lift. The chord stays constant so only the wetted horizontal span changes when the wetted-area requires changes.

Knowing the increased wetted span on the descending side and the decreased wetted span on the ascending side allows the angle of roll to be measured.

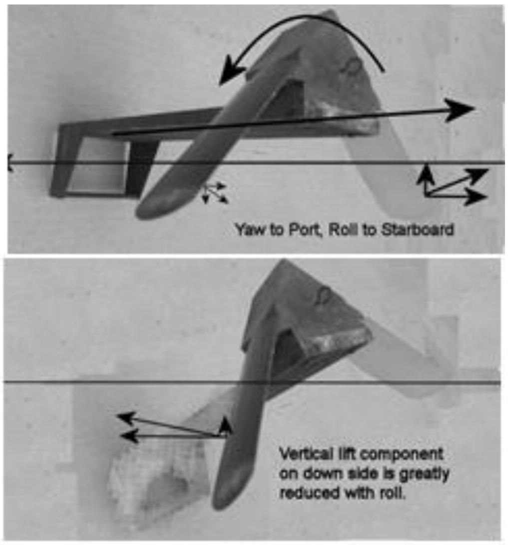

Figure 1: Vellinga model showing yaw vs roll couple.

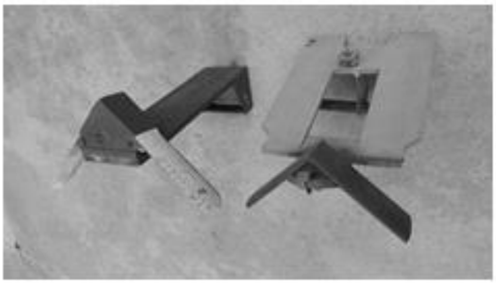

Figure 2: Two Vellinga models used to study yaw & roll characteristics.

To illustrate, here is an example (see Table Ia and Ib). The appropriate cell is indicated in parenthesis. Assume the subject craft is flying straight and level with the movable front foils deployed in the 40^{o} or 45^{o}degree anhedral position. The craft traverses an asymmetric wave or wake, and this disturbance causing an extreme 7^{o} yaw to port (Q27). The port angle of attack is therefore increased to 14^{o} (P27). This causes an increase in lift, and to compensate, and have the lift remain equal to load, the wetted area decreases from 1.388(G20) to .909 square feet (G27). The starboard area adjusts to 5.281 ft. (G13). The chord in this example is 1 ft, therefore the horizontal span is 1.388, .909 and 5.281 ft, respectively (F27,20,13). In step 2, this shift in area & horizontal span is accomplished by rolling to the Starboard, and the resulting angle off horizontal is determined by calculating the ratio of sides of a right triangle superimposed over the face-on view of the anhedral foils. This ratio equals the sine and the corresponding angle is 9.58^{o} (G49).

A corresponding but opposite change of wetted area occurs on the starboard side. The resultant angles off of horizontal, commencing at 45^{o}, are 35.4^{o} port and 54.6^{o} starboard (I49 & K49). Observe the graph in Step 2 showing that at 5^{o} or 6^{o} degrees of roll the rate increases dramatically with small additional increases of yaw.

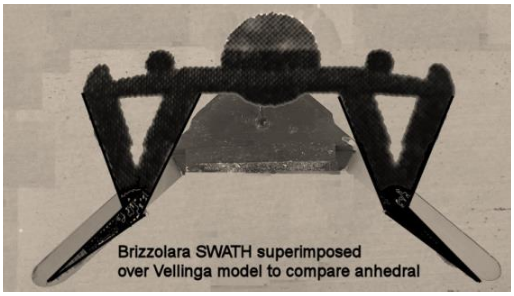

Figure 3: Vellinga model front view superimposed over Authors' drawing.

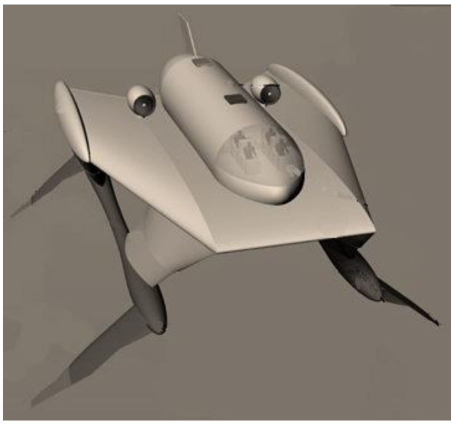

Figure 4: Authors'drawing alternate perspective.

Of course in this illustration I chose an extreme to create a dramatic example of the adverse effects of outside roll linked to any degree of yaw. The reader may wish to use the spreadsheet to observe more modest angles of yaw and the resulting roll. However, whatever the assumption, unlike with dihedral, the problem is -- there is no natural force to correct the adverse roll. A modest roll may progress into a catastrophic roll if left unchecked.

In these examples, we have been considering yaw without a turn, otherwise known as side-slip. However, if the yaw is the beginning of a turn, centrifugal force will exacerbate the outside roll.

This is not necessarily a fatal flaw in the design, if provisions are made to correct for the shortcomings. One obvious solution is to employ an active digital flight control system. There may be other solutions, but changes are definitely necessary.

AUTHORS' RESPONSE

The authors thank **Mr Vellinga** for his comments about his experiments with anhedral foils. The authors agree that an anhedral foil angle causes a coupling between the vehicle drift angle (referred to herein as sway velocity) and a change of foil angle of attack. The foils on the same side of the vehicle as the direction of sway experience a decrease in angle of attack and on the other side the foils experience an increase in angle of attack. This effect is magnified as the anhedral angle increases, and the effect reverses for a positive dihedral angle.

The authors also agree that a systematic approach to calculating the effects of sway, anhedral angle, and spanwise foil submergence is necessary to calculate forces and develop a model of vehicle dynamics. A comprehensive geometric approach to calculating the hydrofoil kinematics and forces has been presented in this paper as the core of a 6 DOF vehicle dynamics model. This model as well as a linearized analytical approach to vehicle dynamics has produced the results and conclusions about stability criteria for the family of foil configurations presented in the paper.

The authors believe that these results presented from the model are in agreement with the instability Mr. Vellinga has observed in his vehicle with 45° anhedral front foils and an aft foil with no anhedral. The conclusion to the paper clearly states that for this hybrid hydrofoil/SWATH with four anhedral foils to achieve directional stability, the aft foils must have at least 2° larger anhedral than the forward foils. A forward foil with 45° anhedral and aft foil with a 0° anhedral does not meet this criterion and therefore can generally be expected to be an unstable foil configuration. Other features like vehicle length, foil spans, etc. must be accounted for, but in general there must be a stronger sway force developing towards the aft of the vehicle to maintain stability in sway perturbations. This effect is equivalent to using fins at the aft of a marine vehicle or airplane for stability.

The authors also state in the conclusion that roll coupling in horizontal plane motion has a substantial effect on directional stability and horizontal plane dynamics. This is characterized by the linear coefficients Y_{ϕ}, the sway force due to a roll angle, and N_{ϕ}, the yaw moment due to a roll angle. Figure 18 shows the sway, roll, and heading coupling for both a stable and unstable version of the anhedral foil configuration. The unstable version of the configuration does show a catastrophic roll to the “outside” as heading direction grows at an accelerating rate in way that resembles a turn initiating. This behaviour, which matches the behaviour described by Mr. Vellinga, is due to directional instability. In the stable configuration case, the same roll direction is coupled with sway, however, the two correct to a stable equilibrium without active control. This correction is due to a balancing of the fore sway force with a greater sway force in the aft. This is mostly characterized by the linear coefficient N_v, the yaw moment due to a sway velocity, which is a critical coefficient for directional stability. Larger dihedral angles in the aft foils relative to the front foils increase this coefficient.

The precise anhedral angle differentials necessary for directional stability must be validated with experiments. The general trends, however, are fundamental to a well-established framework that is used for analyzing directional stability. The authors’ novel contribution has been the application of this framework to a vehicle with four anhedral foils. For a quick validation of these general trends, Mr. Vellinga may try to reverse the foil configuration on his “Hyfibe” hydrofoil so it has a fixed horizontal foil in the front and an anhedral foil in the aft. He may be able to steer with a rudder in the aft or aileron flaps on the front horizontal foil. This configuration would be closer to the suggested configuration in this paper’s conclusion that has larger dihedrals in the aft for directional stability.

Table Ia Supporting calculations (Part I)

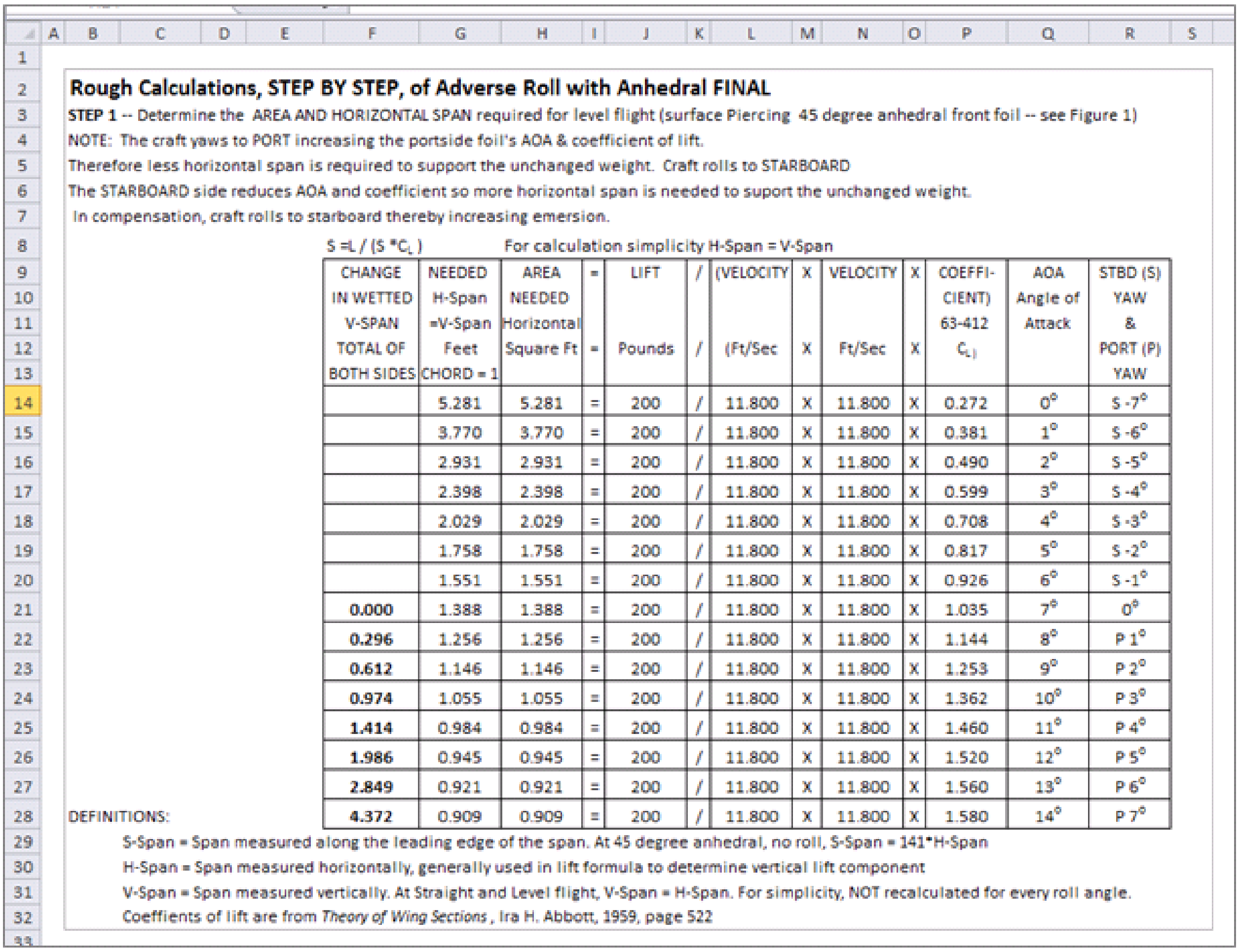

Rough Calculations, STEP BY STEP, of Adverse Roll with Anhedral FINAL

STEP 1 -- Determine the AREA AND HORIZONTAL SPAN required for level flight (surface Piercing 45 degree anhedral front foil -- see Figure 1)

NOTE: The craft yaws to PORT increasing the portside foil's AOA & coefficient of lift.

Therefore less horizontal span is required to support the unchanged weight. Craft rolls to STARBOARD

The STARBOARD side reduces AOA and coefficient so more horizontal span is needed to suport the unchanged weight.

In compensation, craft rolls to starboard thereby increasing emersion.

$S = L / (\$ * C_L)$ For calculation simplicity H-Span = V-Span

CHANGE IN WETTED V-SPAN TOTAL OF BOTH SIDES	NEEDED H-Span =V-Span Feet CHORD = 1	AREA NEEDED Horizontal Square Ft	=	LIFT Pounds	/	(VELOCITY (Ft/Sec	X	VELOCITY Ft/Sec	X	COEFFI-CIENT) 63-412 $C_{L)}$	AOA Angle of Attack	STBD (S) YAW & PORT (P) YAW
	5.281	5.281	=	200	/	11.800	X	11.800	X	0.272	0°	S -7°
	3.770	3.770	=	200	/	11.800	X	11.800	X	0.381	1°	S -6°
	2.931	2.931	=	200	/	11.800	X	11.800	X	0.490	2°	S -5°
	2.398	2.398	=	200	/	11.800	X	11.800	X	0.599	3°	S -4°
	2.029	2.029	=	200	/	11.800	X	11.800	X	0.708	4°	S -3°
	1.758	1.758	=	200	/	11.800	X	11.800	X	0.817	5°	S -2°
	1.551	1.551	=	200	/	11.800	X	11.800	X	0.926	6°	S -1°
0.000	1.388	1.388	=	200	/	11.800	X	11.800	X	1.035	7°	0°
0.296	1.256	1.256	=	200	/	11.800	X	11.800	X	1.144	8°	P 1°
0.612	1.146	1.146	=	200	/	11.800	X	11.800	X	1.253	9°	P 2°
0.974	1.055	1.055	=	200	/	11.800	X	11.800	X	1.362	10°	P 3°
1.414	0.984	0.984	=	200	/	11.800	X	11.800	X	1.460	11°	P 4°
1.986	0.945	0.945	=	200	/	11.800	X	11.800	X	1.520	12°	P 5°
2.849	0.921	0.921	=	200	/	11.800	X	11.800	X	1.560	13°	P 6°
4.372	0.909	0.909	=	200	/	11.800	X	11.800	X	1.580	14°	P 7°

DEFINITIONS:

S-Span = Span measured along the leading edge of the span. At 45 degree anhedral, no roll, S-Span = 141*H-Span

H-Span = Span measured horizontally, generally used in lift formula to determine vertical lift component

V-Span = Span measured vertically. At Straight and Level flight, V-Span = H-Span. For simplicity, NOT recalculated for every roll angle.

Coeffients of lift are from *Theory of Wing Sections* , Ira H. Abbott, 1959, page 522

Table Ib Supporting calculations (Part II)

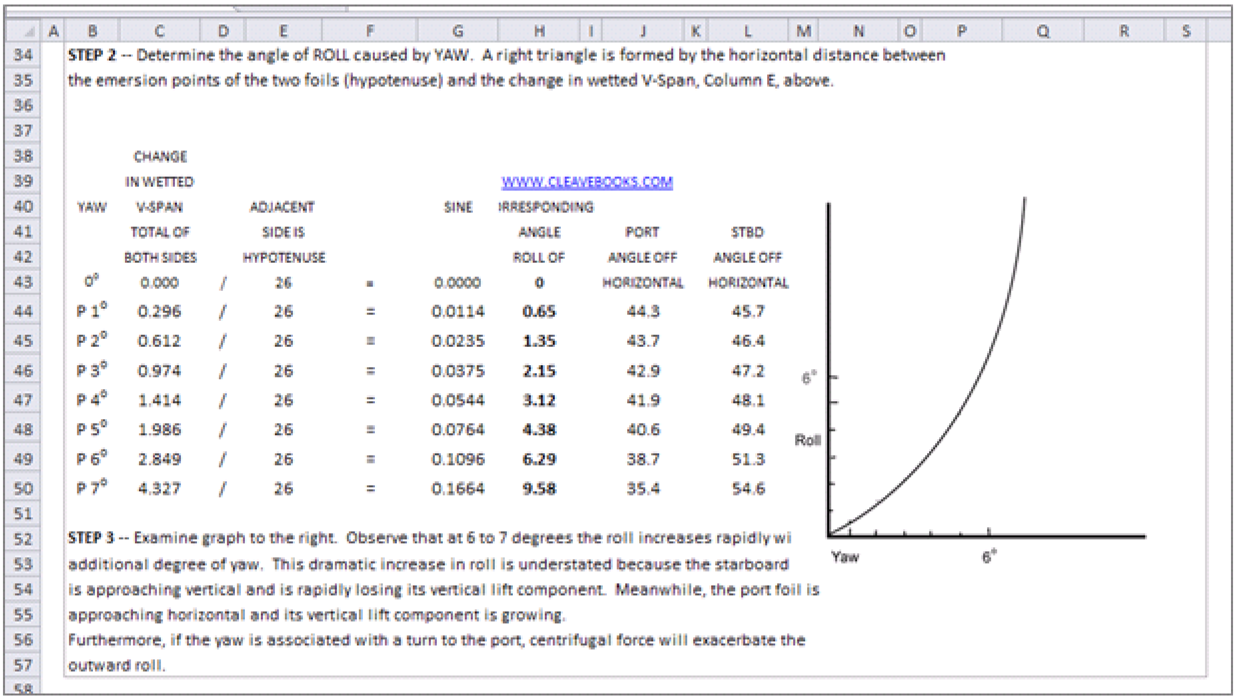

STEP 2 -- Determine the angle of ROLL caused by YAW. A right triangle is formed by the horizontal distance between the emersion points of the two foils (hypotenuse) and the change in wetted V-Span, Column E, above.

WWW.CLEAVEBOOKS.COM

YAW	CHANGE IN WETTED V-SPAN TOTAL OF BOTH SIDES		ADJACENT SIDE IS HYPOTENUSE		SINE	IRRESPONDING ANGLE ROLL OF	PORT ANGLE OFF HORIZONTAL	STBD ANGLE OFF HORIZONTAL
0°	0.000	/	26	=	0.0000	**0**		
P 1°	0.296	/	26	=	0.0114	**0.65**	44.3	45.7
P 2°	0.612	/	26	=	0.0235	**1.35**	43.7	46.4
P 3°	0.974	/	26	=	0.0375	**2.15**	42.9	47.2
P 4°	1.414	/	26	=	0.0544	**3.12**	41.9	48.1
P 5°	1.986	/	26	=	0.0764	**4.38**	40.6	49.4
P 6°	2.849	/	26	=	0.1096	**6.29**	38.7	51.3
P 7°	4.327	/	26	=	0.1664	**9.58**	35.4	54.6

STEP 3 -- Examine graph to the right. Observe that at 6 to 7 degrees the roll increases rapidly wi additional degree of yaw. This dramatic increase in roll is understated because the starboard is approaching vertical and is rapidly losing its vertical lift component. Meanwhile, the port foil is approaching horizontal and its vertical lift component is growing.
Furthermore, if the yaw is associated with a turn to the port, centrifugal force will exacerbate the outward roll.

DISCUSSION

COMPARISON OF MODERN YACHT KEEL TYPES FOR SAILING YACHTS

K Ljungqvist, SSPA Sweden AB, Sweden, **M Orych**, FLOWTECH International AB, Sweden, **L Larsson** Chalmers University of Technology, Sweden and **C Finnsgård**, SSPA Sweden AB, Sweden

(Vol 159 Part B2, 2017)

COMMENT

Kim Klaka, MRINA

This paper reports a valuable and much-needed piece of research. I have one question and one comment, both of which emanate from a short technical note I wrote for the RINA 'Australian Naval Architect' Journal (vol 19 no.1, Feb 2015), copy attached. That note was an attempt to compare the performance gains of a T-bulb keel with the racing time lost due to the likelihood of entanglement of such a keel shape with lobster pot lines (seaweed creates a similar problem).

My one question: When estimating the hydrodynamic effects of different fin-bulb configurations, I applied some of the work by Axfors and Tunander (also referenced in this paper). However, a naval architect friend alerted me to another performance factor – the fore and aft position of the bulb, and its associated shift in LCG from the neutral axis of the fin, usually creates twist in the fin. This twist then causes the angle of attack to change along the span of the fin, with resulting changes in lift and induced drag distribution. It is perhaps worth noting that the fin twist can also change the balance of the yacht adversely. Could the authors estimate the twist for the different keel configurations they tested, then recalculate the performance based on these changes in lift and drag? If they provided the CG positions for the bulbs and the fins, we readers could perhaps attempt this recalculation ourselves, though for comparison purposes we ought to use the same VPP.

And my one comment: The very approximate calculations I presented in the ANA journal note suggested that, if you race in waters where lobster pots (or weed) are often encountered, the performance gains resulting from a T-bulb configuration might well be outweighed by the time taken to disentangle from a pot line caught on the front of the bulb. The fastest boat in the computer is not always the fastest boat around the race course.

AUTHORS' RESPONSE

Thank you very much for your comments, interest in our research and for sending your article "Why do yacht designers fit T-bulbs to the keels of modern racer-cruisers?"

Our answer to the question: The twist induced by the longitudinal centre of the bulb could well be significant for a model yacht with a keel with high aspect ratio and flexible material. However, the deflection on the keel of a large cruiser or a performance cruiser with cast iron or lead keel will be negligible. For example the maximum stress on the YD-41's (the example boat used in the newest edition of Principles of Yacht Design, Larsson *et al.* (2014)), keel blade at 90 degrees of heel is about 40MPa. The deflection is less than 10mm with a cast iron keel.

Our answer to the comment: It is true that the fastest boat in the computer may not be the fastest in reality. Our study has shown the hydrodynamic comparison of the keels, the designer has to take other aspect into consideration as well, in order to get the whole picture.

APPENDIX

The Australian Naval Architect journal Vol 19 No. 1, Feb 2015.
Publisher: Royal Institution of Naval Architects

By: Kim Klaka PhD, MAppSc, BSc(Hons), Cert Ed, MRINA

Why do yacht designers fit T-bulbs to the keels of modern racer-cruisers?

Perhaps some of your readers can enlighten me. The answer to the title question that might reasonably be expected is: "because T-bulbs are faster", but that is perhaps too simplistic….

The question arose when I started investigating entanglement of yachts with craypots. This has become a serious problem on the west coast (and elsewhere), so we are exploring different strategies to manage the risk. I have been keeping a log of entanglement incidents, with over 30 recorded to date. Whilst most of those incidents are snags of pot lines on the rudder or prop, about a third seem to be snagged on the keel bulb when yachts are under sail. There is a performance trade off between any hydrodynamic or stability advantage of the T- bulb, and the time lost disentangling. In order to find out where that trade-off lies, we need to know three things:

1. The likelihood/frequency of entanglement.

2. The time taken to disentangle.

3. The performance advantage of the T-bulb compared with a less "catchy" L-bulb.

Likelihood of entanglement

This is clearly highly variable, but for many races it is close to one entanglement every 24 hours. Here are some informative extracts from reports of yachts entangled whilst racing

Race 1
"On the <overnight> feeder race. Calm weather, 10 knots, night (of course) we caught 4 pots and one cray pot line with 3 floats that was just floating around. The 4 pots stopped us and we lost around 1.5 hrs clearing all of them thru the night we reckon. The loose line dropped our speed and then we had to physically pull the line in to free us. We reckon caught on keel (T keel!!). Action to remove- manoeuvre until free, sail backwards etc. no cutting of anything. No damage sustained.

Race 2
Same on recent <overnight> race, same conditions early am, dark etc but only caught one. There was a line of pots set for some miles in a north south line off the coast which we caught one on the way up. On the way down we were in day light so could avoid them"

Race 3
"<overnight> Race. Most yachts also reported becoming entangled in craypot lines during the race, the long floating lines creating a constant hazard at night."

So it would appear that the likelihood of entanglement on an overnight race is nearly 100%! Let's say that only a third of them are around the keel, then we could estimate there is a 30% likelihood of entanglement around the keel on an overnight race. It could be 10%, it could be 50%, but it's somewhere in that ballpark.

Time taken to disentangle

Estimating the time taken to disentangle has an even wider range of uncertainty than estimating the likelihood of entanglement. The first of the above reports quote 1.5 hours which is a severe case but the minimum time lost in stopping the boat, backing it up and (hopefully) freeing the pot must be at least a couple of minutes, probably a lot more. So let's say the average time lost is 5 minutes per entanglement. It is somewhere between 2 minute and 90 minutes.

Performance gain of a T-bulb

This is where the naval architects start to get excited! My first thought was to go to the regular fall-backs of Hoerner (1965) and Hoerner (1975), expecting to find something useful about aircraft wing tip tanks or similar. Nothing! That's the first time they have failed me. An initial cursory internet search didn't reveal anything useful either. The next step was obvious

– phone a friend. Whenever there is an intriguing design problem I turn to model yachts to see what they do. They use T-bulbs and have problems catching weed in some ponds. Luckily a friend of mine is a professional model yacht designer who has been looking into fins and bulbs, but with a very different approach to what I expected.

Fin twist

His research revealed that the flexure of the fin affected performance – especially twist induced by the longitudinal position of the bulb. An L-bulb has its centre of gravity well behind the twist axis of the fin, so will induce twist. A T-bulb on the other hand has its centre of gravity close to the twist axis of the fin, so the amount of twist, if any, will be small.

The twist changes the angle of attack of the fin along the span, which in turn alters the lift distribution and vertical centre of pressure. The optimum spanwise lift distribution is usually (but not always) elliptical, but the notion that this is generated by an elliptical profile (Spitfire wing), has long ago been proven incorrect when the waves on the free surface are taken into account. Also, a bulb will increase the lift at the fin tip, which can move the distribution away from optimum, but it also has a pseudo-endplate effect, which alters the optimum distribution from elliptical towards uniform. Hmmm…

Twist (positive) will produce more lift near the tip which will create a higher heeling moment. It will reduce the leeway angle of the hull, and here is the design dilemma – most hulls are very inefficient sideforce generators, so reducing hull leeway angle should increase overall lift-drag ratio. However, whilst that might be true for a fat or deep hull, it is rather less so for a slender hull. So the benefit or drawback of twist depends on the hull slenderness.

Let us assume though, that twist is detrimental to performance. Given the difficulties in quantifying its effect, I have taken a different approach. Let us suppose we wish to reduce the twist angle on a keel by, say, half. What is the increase in fin thickness required to achieve this, and what is the resulting drag increase and speed loss? To halve the twist we must double the polar inertia, which varies roughly as the cube of section thickness. So a 26% increase in section thickness will halve the twist. From Marchaj (1979), achieving this by increasing the section thickness from a NACA 0012 to NACA 0015 will increase the section drag coefficient by 11% at Reynolds numbers typical for yacht keels. What contribution does this make to total drag? Using convenient published data for the YD-40 in Larsson and Eliasson (1994) the section drag contributes about 11% of total drag at 6kn boat speed and 6% at 8kn. Let's call that an average of 8% around the course. So the increase in drag due to increase in keel thickness is 11% of 8%, which is a 0.9% increase in total drag. Next, let us make a wildly hand-waving approximation that drag varies with the cube of speed, then we have a 0.3% drop in speed due to the increase in keel thickness required to halve the twist angle. For a 24 hour race this corresponds to a time loss of just over 4 minutes.

Fluid flow

Now let's get back to bulb longitudinal placement itself. A nicely packaged piece of research from Chalmers University (Axfors and Tunander, 2011) examined the hydrodynamic differences of several keels, all with the same draft and righting moment. The results were then put into a VPP and they got some interesting answers. A well-designed T-bulb (a craypot catcher) is faster than a well-designed L- bulb (a craypot dodger), but not by much. (Interestingly, the study found a conventional non-bulb fin was even faster that the T-bulb, though they qualify that statement with reasoning that is not very convincing in my view.) Taking the average of the VPP results for true wind speeds of 8, 12, 16 and 20 knots, over a range of wind angles representative of an Olympic style race course, the T-bulb averages 2 and a half minutes faster than the L-bulb over 24 hours of racing (it's nearly 6 minutes faster in 8kn of wind and just 30 seconds faster in 20kn).

Overall speed effect.

Taken over a 24 hour race, if we add the 2.5 minute speed loss due to L-bulb position and the 4 minute speed loss due to increased keel thickness, we have a total speed loss of about 6.5 minutes for the L-bulb compared with the T-bulb. Our earlier estimate of likely time lost due to a keel entanglement in an overnight race was around 5 minutes, with a 30% chance of it occurring. In other words, the T-bulb is only faster if you are sailing somewhere where the likelihood of entanglement is low (and the typical wind speeds are low).

So there we have it – the benefit of the T-bulb on a race course along a lobster-friendly coastline is marginal at best, and they are a big nuisance when cruising; designers please take note!

My next task is to investigate ways to reduce the likelihood of craypot entanglement with the prop and rudder. Some cruisers fit a wire from the keel trailing edge to the bottom of the rudder(or skeg if they have one). It is easy to calculate the drag increase (from data on towed umbilical cables e.g. Erdsal, 2004), but do those wires actually reduced the likelihood of entanglement? Any feedback?

References

AXFORS B. & TUNANDER H (2011) *Investigation of keel bulbs for sailing yachts*. MSc Thesis report no X-11/263, Department of Shipping and Marine Technology, Chalmers University, Sweden

ERSDAL, S. (2004). *An experimental study of hydrodynamic forces on cylinders and cables in near axial flow*. Department of Marine Technology, NTNU, Trondheim, Norway.

HOERNER, S. F. (1965). *Fluid dynamic drag.* Hoerner Fluid Dynamics, Bricktown USA.

HOERNER, S. F. and H. V. BORST (1975). *Fluid dynamic lift*. Hoerner Fluid Dynamics, Bricktown USA.

LARSSON L. & ELIASSON R.E. (1994) *Principles of yacht design*. International Marine, Camden, Maine USA.

MARCHAJ C.A. (1079) *Aero-hydrodynamics of sailing*. Granada, St. Albans UK.

DISCUSSION

THERMAL LOAD EFFECTS ON ALUMINUM LIGHT ALLOY PLATES WITH EPOXY COATINGS

D Boote, T Pais, G M Vergassola, University of Genova, Italy and **D Giannarelli,** Naval Architect, Italy

(Vol 159 Part B2, 2017)

COMMENT

John Kecsmar, Ad Hoc Marine Designs Ltd

Thank you for a very interesting paper. I have a few questions which would aid my understanding of your research and the results that you present.

In section 2 you refer to distortion from fabrication, yet make no reference to any known standards, such as IACS No.47 Shipbuilding and Repair Quality Standard or LR SSC rules, Pt.3. Ch.1 Sec.8, thus where did the values you quote come from as a measure of acceptance or commonly found?

Later you state: "*White paints are cheaper, better to hiding imperfections*…"etc., yet no references or examples or given to substantiate this. Since it seems at variance with the "luxury" aspect that you allude too; as why would a luxury yacht owner select a cheaper paint? Surely it is not just the colour, but also how 'shiny' the finished paint is - as shiny colours, even dark, can reflect just as much heat as white colours?

In section 5, you state the FEM is based upon a stiffener spacing of 300mm and frame spacing of 1.07m, yet in section 4, you have used a test panel not representative of the actual vessel's panel size, given in section 5? Thus it is confusing why a test panel of 580 x 380mm is used for verification of a hull panel that is 1070 x 300mm; it is not consistent representation and is thus prone to errors in extrapolation. What is the rationale behind this?

Figure.6 shows a varied weld sequence inside the panel…it does not appear to be consistent with common fabrication of aluminium vessels; especially the short "blob" above the number 1 written on the panel. Welding sequence and weld lengths play a significant role in panel distortion. What controls and methods were used as none are given or presented for reference?

In 4.2, I find it hard to believe that the structural model boundary condition is assumed to be a simple support. It must surely be a partial fixity owing to the welded restraint, and is compounded by the restraint in the opposite axis (support/weld) preventing rotation near these right angled intersections which would suggest full fixity. Can the authors explain the rationale behind the simple support assumption?

In Section 5, how is the difference in structural loading between the QUAD-4 elements, which generally allow 6 degrees of freedom per node, and the SOLID which allows 3 degree of freedom per node accounted for in the results?

In Figure.17 there appears to be no temperature rise on the main deck. Why is this? Was the application of the heat only on the exterior surface? If so, can the authors explain why the heat does not transfer in-plane as would be expected?

Alan Dowd, Premier Composite Technologies

I thank the authors for an interesting investigation of what is a time consuming and expensive aspect of yacht building.

In the analysis of the results and displacement curves presented, the total deflection between bulkheads is 4-5 times larger than the waviness between the frames.

Is this an aspect of the method of analysis? Wouldn't this imperfection to the fairness be of as great a concern as the frame waviness?

The options offered by the authors for reducing the displacements between frames seem to be increased plate thickness and or reduced frame spacing.

These solutions add weight and cost to the build process. As all builders want the most cost effective manner to achieve the specific standards of an owner, I hope the research continues and provides a method for weight and cost comparisons of the different structural arrangements as compared to reduced use of epoxy fillers for a specific fairing standard.

AUTHORS' RESPONSE

First of all we wish to thank **Mr Kecsmar** for his interest in our work and his comments, which gave us interesting warnings and hints for future developments. In the following we will try to answer to his observations.

The values of distortion from fabrication we have reported in Section 2 have been measured in superyacht shipyards and come from the experience of shipyards themselves. A common rule on this aspect is the maximum filler thickness which can be accepted, in general not more than 10 mm over flat surfaces and 15 - 20 mm on high curvature zones and corners for light alloy vessels. Lower values are admissible for steel hulls (6 - 8 mm). In some measurements carried out on two L.A. and steel vessels after the publication of this paper, the plate distortions resulted to be of the order on 7 - 8 mm and 10 – 15 mm for side bending in case of light alloy vessels. For steel yachts average values of plates distortions are around 5 – 6 mm, with 10 mm as a maximum in one point (before plate straightening). The maximum value recommended by IACS Rules n.47 (Table 6.10 and 6.11) corresponds to 8 mm for plate distortions between frames. It should be noted that this standard is valid for steel ships and not specifically for yachts. LR SSC rules (Pt.3. Ch.1 Sec.8) give lower limits for plate deformations (between 3 and 6 mm) depending on plate thickness and hull zone, strangely the same for steel and L.A. vessels.

About white paints, even if the yacht colour mainly depends on owner's aesthetic preferences, an evaluation of the cost/quality ratio is always a good practice in any design procedure. From this point of view white paints are always the best solution. The absence of reference regarding the lower cost with respect to dark paint is due to commercial agreements among owner, shipyard and the supplier.

The size of experimental specimens is the largest one we can handle with our laboratory facilities. The laboratory tests have been carried out in order to validate the simulation and to calibrate the filler parameters needed for the numerical analysis. In any case the calibration of a FEM model by experimental measurements, within certain small scale factors (like in this case), should not depend on specimen dimensions.

Regarding the comments on the welding pattern used for specimens, we asked a superyacht shipyard to realise them with the same technique used for the side of L.A. superyacht. The short blob is what we call "spot-welding" used to adjust and fix the parts before the final welding. The figure does not show the complete specimen but, there is a blob on each side of the panel at its middle length.

In the FE analysis we have used brick solid elements, in which the rotational DOF are constrained by the shape of the element. So no other external constrains are needed to prevent rigid body motions.

In Figure 17, the zero temperature rise on the main deck is due to the fact that attention has been focused only on what happened on the side hull plates and so we have not applied any heat load on the main deck; for this reason its temperature distribution is close to the initial one. If we had applied the heat load also to the main deck, also the superstructure modelling would have been necessary.

We also thank **Mr Dowd**; our research is currently ongoing in the direction of an optimized structural layout in order to reduce weight and cost of L.A. vessels. The solution we presented in this paper, i.e. the use of small vertical reinforcements, was the one selected by the shipyard in order to solve the problem of high thermal deflection with the lowest cost and weight increase. From results got after the yacht delivery, it was demonstrated to be acceptable. Obviously the best solution would have been to recalculate the structure layout. But shipyards often build several units on the same hull project and a change in the hull colour (from white to dark blue as an example) does not allow/justify a new scantling of the hull structures.

We fully agree that the deflection between bulkheads is larger than the waviness, but human eyes are more sensible to wave deformation and they see them as a more relevant defect with respect to a global deformation. In this article, we were more interested in the aesthetic concerns caused by thermal loads and so our focus was in the direction of local waviness.

The Transactions of The Royal Institution of Naval Architects – Part B

International Journal of Small Craft Technology

GUIDANCE NOTES FOR AUTHORS

All papers, technical notes and discussions should be submitted in electronic form, normally in MSWord format. Authors wishing to submit in other formats should first contact RINA Headquarters. Submissions should be forwarded on PC compatible disks or CD-ROM, containing the full text, including inserted figures. Submissions less than 5Mb may be forwarded by email or online.

Authors are responsible for obtaining security clearance as required. If they so wish, authors may add a disclaimer stating that the opinions expressed are solely those of the author.

In submitting papers or technical notes for publication, authors implicitly assign copyright to the Royal Institution of Naval Architects if the paper or technical note is published. Where copyright is held elsewhere, authors must present evidence of approval to re-publish.

When submitting contributions for publication, authors must state if the paper or technical note has been published before and where, or whether it is being considered for publication by some other publisher

Papers: Papers should not normally exceed 6000 words (with up to 10 illustrations). Longer papers where the content justifies the extra length may be published at the Editor's discretion. The required format of papers submitted for publication may be obtained from the RINA website or from RINA Headquarters

Technical Notes: Technical notes should not normally exceed 1500 words (and up to 5 illustrations). The required format of technical notes submitted for publication may be obtained from the RINA website or from RINA Headquarters

Discussion: Discussion of published papers, or comment on published discussion, should not normally exceed 500 words (with up to 2 illustrations).

All submissions for publication should be forwarded to:

The Editor (IJSCT)
The Royal Institution of Naval Architects
8-9 Northumberland Street
London WC2N 5DA, UK
Tel: +44 (0)20 7235 4622   Fax: +44 (0)20 7259 5912
Email: ijsct@rina.org.uk   Online: www.rina.org.uk

THE ROYAL INSTITUTION OF NAVAL ARCHITECTS

The Royal Institution of Naval Architects is an internationally renowned professional institution and learned society, whose members are involved at all levels in the design, construction and repair of ships, boats and maritime structures, in over 80 countries. RINA is widely represented in the marine industry, universities and colleges, and maritime organisations worldwide.

Membership is open to those who are professionally qualified in naval architecture or a related subject, or who are involved or interested in the maritime industry. RINA members enjoy a wide range of benefits and services, including advice on education, training and professional development. The RINA also publishes a range of technical journals, books and papers, and organises an extensive programme of international conferences and training courses covering all aspects of naval architecture and maritime technology, available to members free or at reduced rates

The Transactions of The Royal Institution of Naval Architects

Vol 160 Part B1 2018 ISSN 1740-0694

International Journal of Small Craft Technology

CONTENTS

PAPERS

TECHNICAL NOTES

There are no Technical Notes published in this issue of the IJSCT

DISCUSSION